Systems approach to the multi-timescale dynamics of photosynthesis

Matsuoka, Takeshi

(Degree)
博士（工学）

(Date of Degree)
2015-03-25

(Date of Publication)
2017-03-25

(Resource Type)
doctoral thesis

(Report Number)
甲第6453号

(URL)
https://hdl.handle.net/20.500.14094/D1006453

PhD thesis

Systems approach to the multi-timescale dynamics of photosynthesis

光合成のマルチスケールダイナミクスに対するシステム解析

Graduate School of System Informatics,
Department of Computational Science, Kobe University
Takeshi Matsuoka

January 2015

Contents

Chapter 1

General Introduction

In living organisms, temporally and spatially multi-scale chemical reactions occur in a systematic way. Photosynthesis, the system of which has been constructed via plenty of evolution processes over a long time, provides a typical example of such a multi-scale reaction system. To adapt to changeable environmental conditions such as light, temperature and humidity, photosynthetic reaction systems have a variety of mechanisms for progressing reactions stably at each scale of protein, organelle, cell, tissue and whole body [1]. For example, chlorophyll *a* fluorescence induction, which exhibits responses to environmental changes of light, is well known as a phenomenon that represents a multi-time-scale property of photosynthetic reactions [2]. This phenomenon is observed when a photosynthetic organism that has been acclimated to the dark beforehand is continuously illuminated with a constant light intensity; it then shows a transient process of progressing reactions stably under the given light condition [3]. The notable properties of this phenomenon reflect multi-time-scale characteristics and different time-course patterns of fluorescence intensity with respect to different light conditions [2]. Experimentally observed time-course patterns are classified into fast change patterns (microsecond - second) and slow change patterns (second - hour). Besides, very fast processes are also involved concerning excitation-energy and electron transfer processes ($\sim$ picosecond) [4–7], though they are not apparent in the characteristic time scale of the induction phenomenon. This induction phenomenon has been theoretically studied on the basis of several mathematical models of photosynthetic reaction systems at various time scales [8–19]. Although many studies have been performed to elucidate this issue, a full understanding and consensus about the meaning of these time-course patterns and the detailed mechanisms have not yet been achieved [3, 20].

In Chapter 2, I shortly review previous studies about fluorescence induction phenomena and some theoretical studies concerning this topic. There remain some problems for constructing a better mathematical model of photosynthetic reaction systems. Several detailed studies about the components of photosynthetic reaction processes have been already conducted [21–25]. Thus, the construction of a mathematical model based on microscopic structural information, which is obtained, for example, by X-ray crystal structural analysis, can be achieved. However, a more detailed model description makes it more difficult to understand the dynamic behavior of the whole system intuitively because it makes the objects too complex [10]. Furthermore, such a precise description would lead to an intractably higher calculation cost, because the fast-time-scale processes have to be analyzed for the calculation of a multi-time-scale mathematical model even if one is concerned with slower-time-scale dynamics [26].

To overcome these problems, I propose a hierarchical reduction scheme to cope with coupled rate equations that describe the dynamics of multi-time-scale photosynthetic reactions in Chapter 3. To numerically solve nonlinear dynamical equations containing a wide temporal range of rate constants, I first study a prototypical three-variable model. Using a separation of the time scale of rate constants combined with identified slow variables as (quasi-)conserved quantities in the fast process, I achieve a coarse-graining of the dynamical equations reduced to those at a slower time scale. By iteratively employing this reduction method, the coarse-graining of broadly multi-scale dynamical equations can be performed in a hierarchical manner. I then apply this scheme to the reaction dynamics analysis of a simplified model for an illuminated photosystem II, which involves many processes of electron and excitation-energy transfers with a wide range of rate constants. I thus confirm a good agreement between the coarse-grained and fully (finely) integrated results for the population dynamics.

In Chapter 4, an extensive kinetic model of photosystem II (PS II) combined with oxygen-evolving complex (OEC) and light-harvesting chlorophyll-protein complex II (LHC II) is analyzed through the use of the hierarchical coarse-graining method proposed in Chapter 3. PS II is a protein complex which evolves oxygen and drives charge separation for photosynthesis employing electron and excitation-energy transfer processes over a wide time scale range from picoseconds to milliseconds. While the fluorescence emitted by the antenna pigments of this complex is known as an important indicator of the activity of photosynthesis, its interpretation was difficult because of the complexity of PS II. In this coarse-grained analysis, the reaction center (RC) is described by two states, open and closed RCs, both of which consist of oxidized and

neutral special pairs being in quasi-equilibrium states. Besides, the PS II model at millisecond scale with three-state RC, which was studied previously, could be derived by suitably adjusting the kinetic parameters of electron transfer between tyrosine and RC. Our novel coarse-grained model of PS II can appropriately explain the light-intensity dependent change of the characteristic patterns of fluorescence induction kinetics from O-J-I-P to O-J-D-I-P.

In Chapter 5, the coarse-graining method is applied to the model of PS I under continuous light. The coarse-grained model describes the RC by seven variable states, though the original model describes the RC by 2^8 states. Based on the derived model, I_{820} curve, which reflects the accumulations of P_{700}^+ and Pc^+, is simulated and analyzed. With respect to this signal curve, it is revealed that the increase up to the inflection point at 10^{-3} s, the increase from that point to the peak at 2 $\times 10^{-2}$ s, and the decay after that peak reflect the accumulations of P_{700}, Pc^+ and $P_{700}F_A^-F_B^-$, respectively. Besides, the important role of the charge recombination processes from $P_{700}^+A_{1A}^-$ and $P_{700}^+A_{1A}^-$ states for the dissipation of the extra absorbed energy in photosynthetic induction time is confirmed.

In Chapter 6, I summarize the present works and discuss the remaining problems and the future perspective.

Chapter 2

Background

2.1 Processes of photosynthesis

Photosynthesis is one of the most important reaction on the Earth. Almost all working of the living things consumes the energy of the sun light caught by this reaction. Over a long period of time, the mechanism of this reaction has been studied. In the early 19th century, chloroplast, that is the organelle in which all reaction of photosynthesis occur, was discovered. In the early 20th century, it were revealed that photosynthesis reaction is composed of light-dependent reactions and temperature-dependent reactions, later called as "light reaction" and "dark reaction", respectively. With respect to "dark reaction", Calvin determined the reductive pentose phosphate cycle (Calvin-Benson cycle) in 1956. For "light reaction", Emerson revealed that two photosystems work in tandem in 1957. Light reaction occurs at thylakoid membrane (Fig. 2.1). In this membrane, there is cytochrome b6/f protein complex in addition to photosystem I and photosystem II. Electron transfers linearly over the pigments located in series on these membrane binding complexes. In the late 20th, technological development made it possible to determine the structure of components of this reaction at atomic level. In 2001, The structure of Photosystem II and Photosystem I were revealed by x-ray crystal structural analysis. Although the static structure of photosynthesis has thus been revealed, the dynamic property of this phenomena has hardly been elucidated. To understand such a property, systems approach provides one of the useful tools.

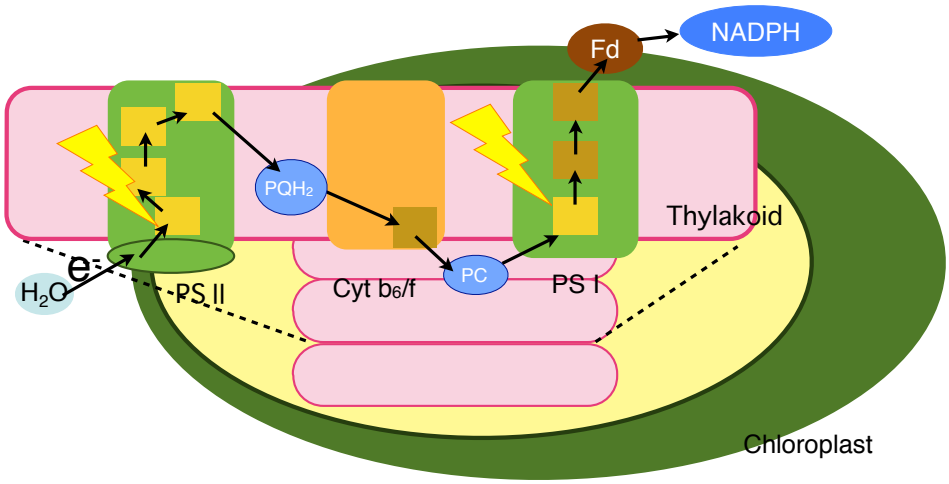

Figure 2.1 Electron transfer reaction processes on thylakoid membrane in chloroplast.

2.2 Fluorescence induction

Understanding the dynamic property is important to understand the mechanism of regulation of photosynthesis such as environmental response [27]. With respect to the light environment response of photosynthesis, chlorophyll *a* fluorescence induction phenomena (FI) is well known [28]. This phenomenon was first observed by Kautsky in 1931. In early days, the intensity of fluorescence emitted by chlorophyll was regarded as reflecting the amount of excitons which are not used by photochemical reaction. This phenomenon is observed when the photosynthetic organisms adapted to dark beforehand are illuminated with continuous light. On the one hand, fluorescence intensity rapidly increases after the illumination and then decreases to the lower steady intensity; on the other hand, the rate of CO_2 assimilation gradually increases to the steady rate. These behaviors show the inverse correlation. With the experimental improvement of resolution in time, it has been revealed that FI shows various time-

course patterns depending on the light intensity. The patterns are often separated into fast-change pattern and slow-change pattern based on the timescale of each pattern [23]. The former and latter indicate the patterns over millisecond to second range and over second to minute range, respectively. To explain the complex behavior of FI, various quenchers of fluorescence (i.e., the components which reduce the intensity of fluorescence) have been detected and proposed.

2.2.1 Quantum efficiency

The fluorescence intensity is widely observed as the indicator of photosynthesis activity in terms of fluorometry. The intensity of fluorescence is interpreted by use of the formula as follows [29]:

$$F_{\mathrm{t}} = V_{\mathrm{in}} \cdot \Phi_{\mathrm{F}}(t),$$
$$\Phi_{\mathrm{F}}(t) = \frac{k_{\mathrm{F}}}{k_{\mathrm{F}} + k_{\mathrm{P}}(t) + k_{\mathrm{H}}(t)},$$

where F_{t}, V_{in}, and $\Phi_{\mathrm{F}}(t)$ are photon flux density of fluorescence, photon flux density of incident light and quantum efficiency of fluorescence, respectively. Quantum efficiency of fluorescence indicates the probability that the exciton created by illumination is emitted as fluorescence. k_{F}, $k_{\mathrm{P}}(t)$ and $k_{\mathrm{H}}(t)$ are the rate constants of fluorescence emission, photochemical reaction and heat dissipation of excited energy in antenna chlorophyll, respectively. The rates of photochemistry and heat dissipation change with time following the proceeding of reaction. Photochemical and heat dissipation rates are determined by the states of electron transfer chain and those of quenchers, respectively.

The losses of energy via heat dissipation are caused by the light-induced path and the non-light-induced path [30]. The former of these paths is particularly called as non-photochemical quenching (NPQ). NPQ is regarded as the key factor that governs the slow-change patterns of FI, and the non-light-induced heat dissipation paths are considered to determine the fast-change patterns of FI [31].

2.2.2 Quenchers of Chl *a* fluorescence

A variety of factors have been proposed as the quencher of Chl *a* fluorescence. Among these quenchers, the typical ones that are not induced by light are as follows:

- P^{+}_{680} quenching shows similar efficiency to photochemical quenching [32].
- P_{680} triplet which survives as long as some hundred micro seconds is regarded as a quencher [33].
- Carotene triplet plays a role of quencher under very high intensity light [34].
- The oxidized state of plastoquinone-pool (PQ-pool) plays a role of quencher. This effect is observed by comparing between the samples whose electron transfer to PQ-pool is restricted by inhibitor, e.g. 3-(3,4-dichlorophenyl)-,1-dimethylurea (DCMU), and those whose electron transfer is not restricted [35].

The light-induced quencher, NPQ, is classified into three categories: q_E, q_I and q_T [36]. q_E is the NPQ that depends on the processes for energy accumulation. This q_E is considered to be regulated by the pH of the lumen, which is the inside space of the thylakoid membrane vesicle. The protonation of PsbS protein and the binding of zeaxanthin that is generated by the de-epoxidation of violaxanthin induce the conformational changes of the antennae that account for the increases of thermal dissipation of excited-energy [37]. q_I is the NPQ that depends on the photo-inhibition. This factor is considered to be related to processes such as repairing cycle of damaged PS II [37]. q_T is the NPQ that depends on the state transition which is the process of LHA traveling for the purpose of regulating energy allocation between two photosystems, PS II and PS I [38]. The classification above is based on the difference of relaxation time scales of fluorescence in dark. That is, the amount of absorbed light for driving photosynthesis is regulated in various timescales.

These different NPQs have been analyzed based on the simulation of the dynamics of the fluorescence transient at each different timescale [31]. However, the consistent understanding of this phenomenon has not been achieved because of the complexity and the hierarchical spatiotemporal property of the whole picture.

2.2.3 Characteristics of the patterns of FI

The patterns of FI are known to be different depending on the species and the environmental condition [2]. The three parameters, oxygen evolving rate, CO_2 uptake rate and the difference of pH across the thylakoid membrane, i.e. the difference between stroma and lumen, are correlated with the FI [3]. The characteristics of these parameters in regard to the O-P-S-M-T pattern, which are observed in higher plants, is as follows:

- Oxygen evolving rate:
  Oxygen evolving rate increases during O-I phase, then decreases until peak P. After that, it increases again and reaches a plateau during MT phase.
- CO_2 uptake rate:
  The value of CO_2 uptake rate remains zero during O-P-S pattern of FI. This rate starts to increase in S-M phase and reaches a steady state at the end of M-T phase.
- pH difference across the thylakoid membrane:
  pH difference between stroma and lumen is considered to be in proportion to the rate of electron transfer. This value has a negative correlation with FI, i.e., it decreases on P-S phase, increases in S-M phase, and decreases again in M-T phase.

With respect to higher plants, the several-times repetition of S-M-T wave cycle is observed under abnormal circumstance. Such cycle is regarded to come from the transient restriction on the receiver of electron flux behind PS I. This sort of limit is caused by the deficiency of supply of $NADP^+$, phosphorus or oxygen, or excessive supply of CO_2.

parameter	OI	IP	PS	SM	MT
O_2 evolving rate	↗	↘	↗	↗	becomes steady after transient plateau
CO_2 uptake rate	0	0	0	↗	↗ and then becomes steady at the T point
Δ pH across thylakoid			↗	↘	↗

In general, the slow-change pattern of FI is more difficult to understand than the fast-change pattern because more factors are involved .

2.3 Kinetic models of excitation-energy and electron transfer processes

2.3.1 Principle

Electron and excited-energy transfer processes can be described by means of reaction kinetics. In this treatment, the variables of the ordinary differential equations are set as the states of electron of each pigment which construct the electron transfer

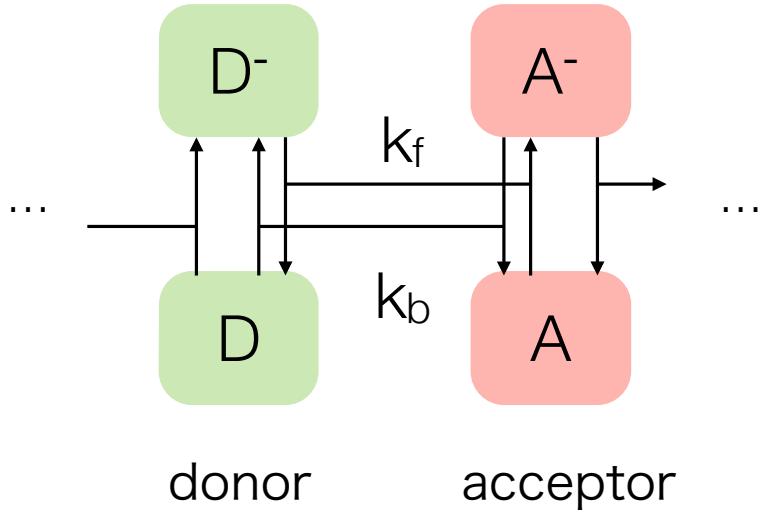

Figure 2.2 Diagram of electron transfer processes between donor and acceptor.

chain on thylakoid membrane. Change of each state is described to occur when electron or excited-energy transfer happens. For example, a charged electron acceptor is created when an electron transfers from a charged electron donor to a neutral electron acceptor occurs (Fig. 2.2). The rate of this transfer is described by the product of the concentration of the charged donor and that of the neutral acceptor. The dynamics of the change of the states of electron carriers evoked by electron transfer processes are thus described as

$$\begin{cases} \dfrac{d[D^-]}{dt} = -k_f[D^-][A] + k_b[D][A^-] + \cdots, \\ \dfrac{d[A^-]}{dt} = k_f[D^-][A] - k_b[D][A^-] + \cdots, \end{cases} \tag{2.1}$$

where the conservation relation holds:

$$\begin{aligned} [D^-] + [D] &= const, \\ [A^-] + [A] &= const. \end{aligned} \tag{2.2}$$

Here, $[D^-]$ and $[D]$ represent the concentrations of charged donor and neutral donor,

respectively. $[A^-]$ and $[A]$ represent the concentration of charged acceptor and neutral acceptor, respectively. k_f and k_b are rate constants of forward and backward electron transfer processes, respectively. In principle, the model of photosynthetic electron transfer processes can be constructed by adding all the states of pigments on electron transfer chain to the differential equations and connecting them by the electron or excited-energy transfer processes.

2.3.2 Excited-energy transfer in lattice

Photoexcitation at antenna complex initiates photosynthesis. Once exciton that is generated by photon absorption reaches the reaction center (RC), then electron transfer is driven by charge separation. This excited-energy transport process at antenna system is simply expressed by the use of a homogeneous lattice model [39,40].

kinetic model of trapping by RC

The exciton transport process at light harvesting antenna (LHA) lattice is represented by the master equation:

$$\frac{\mathrm{d}p_i}{\mathrm{d}t} = -k_l p_i + \sum_j (p_i W_{ji} - p_i W_{ij}) - \delta_{i,\mathrm{RC}} \gamma p_{\mathrm{RC}}. \tag{2.3}$$

Here, k_l, W_{ij}, γ and p_i represent the rate of excited-energy loss at LHA, the hopping rate from site i to site j, the rate of quenching at RC, and the population of exciton at site i (the notation "RC" indicates reaction center site), respectively.

LHA-lattice is characterized by the space structure, site number N, dimension d and coordination number z. This process is regarded as a random walk on lattice. The characteristics of random walk on a variety of lattices are analyzed by Montroll [41,42]. With respect to the case that trap-site owing a quencher exists on lattice, Perlstein developed the generalized theory for the lifetime of a random walker [43].

Average life-time approach

In 1982, Perlstein analyzed the lifetime of the exciton on LHA based on a model of the lattice with trap site [43]. The lifetime is given by the zeroth moment M_0 of the total exciton population on lattice.

$$M_0 = \int_0^\infty \left(\sum_{n=0}^{N-1} \rho_n(t) \right) dt. \tag{2.4}$$

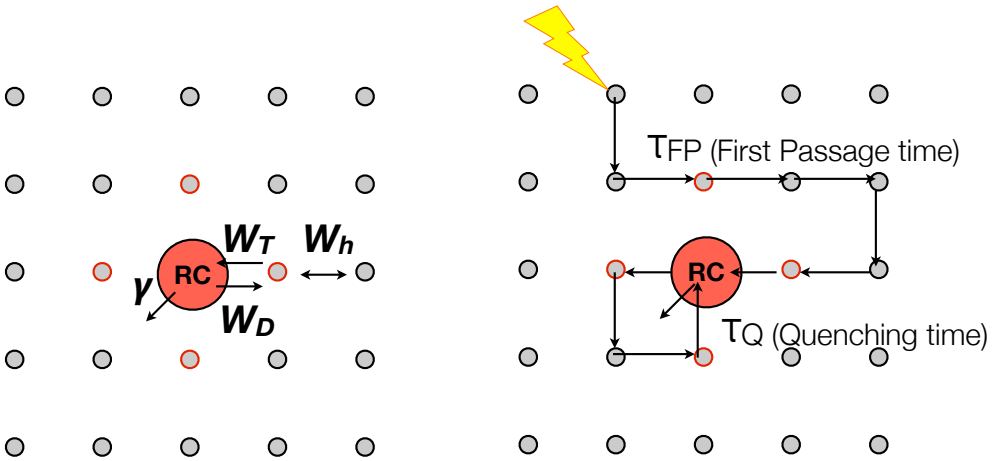

Figure 2.3 Excited-energy transfer processes in a lattice model.

This depends on the initial value of the population of the exciton on lattice. In the condition where the exciton transport is restricted to the nearest-neighbor and the initial values are set as $\rho_0 = \rho_{RC}$ and $\rho_{i\neq 0} = (1-\rho_{RC})/N$, M_0 is expressed as

$$\begin{aligned} M_0 &= \frac{W_T + W_D(N-1)}{W_T}\frac{1}{\gamma} + (1-\rho_{RC})\left(\frac{N-1}{z}\left(\frac{1}{W_T} - \frac{1}{W_h}\right) + \frac{N^2}{N-1}h_d(N)\frac{1}{W_h}\right) \\ &= \tau_Q + (1-\rho_{RC})(\tau_T + \tau_{mig}) = \tau_Q + (1-\rho_{RC})\tau_{FP}, \end{aligned} \tag{2.5}$$

where W_T, W_D and W_h represents the rate constant for trapping to RC from its neighbors, detrapping from RC, and hopping between others, respectively. Here, τ_{FP} is the "first passage time", i.e. the average time taken for an exciton generated at LHA to arrive at RC, and τ_Q is the "all revisiting time", i.e. the average time taken to be quenched after arriving RC. These ideas are described in Fig. 2.3. On the one hand, this process is "trap-limited" if multi-revisiting occurs, but on the other hand, it is "diffusion-limited" if revisiting hardly occurs.

τ_{FP} can be decomposed into the time taken to arrive at the site next to RC, τ_{mig}, and that taken from RC neighbor site to the RC, τ_T.

$$\begin{aligned} \tau_Q &= \frac{W_T + W_D(N-1)}{W_T}\frac{1}{\gamma}, \\ \tau_T &= \frac{N-1}{z}\left(\frac{1}{W_T} - \frac{1}{W_h}\right), \\ \tau_{mig} &= \frac{N^2}{N-1}h_d(N)\frac{1}{W_h}, \end{aligned} \tag{2.6}$$

where τ_{mig} depends on the function $h_d(N)$ of the geometrical structure of lattice. M_0 is linearly dependent on the initial value $(1 - \rho_{RC})$.

Perturbed two-level model

If the size of antenna system is small, the time taken for the exciton transfer inside of the LHA to reach the equilibrium is much shorter than that taken to be quenched at RC. In this case, the antenna system can be regarded as a super-molecular complex by the assumption that the time taken for the exciton migration inside the LHA is infinitesimally short: $W_h = 0$ as the first approximation. If the exciton transport inside of the LHA is restricted to nearest-neighbor, the rate between RC and LHA is represented as

$$\begin{aligned} \bar{W_T} = \frac{1}{N-1}\sum_{n=1}^{N-1} W_{0n} = \frac{zW_T}{N-1}, \\ \bar{W_D} = \sum_{n=1}^{N-1} = zW_D. \end{aligned} \tag{2.7}$$

Then the rate τ_+ for the equilibrium and τ_- for the decay of excited-energy are Expressed, respectively, as

$$\lambda_\pm = -\frac{\gamma + \bar{W_T} + \bar{W_D} \pm \sqrt{(\gamma + \bar{W_T} + \bar{W_D})^2 - 4\gamma\bar{W_T}}}{2}. \tag{2.8}$$

In the case that the time for the migration inside the LHA is finite, the effect of the migration time is evaluated by expanding the lifetime of the exciton by the hopping time W_h [44].

Chapter 3

Hierarchical Coarse-Graining Method for Photosystem II

3.1 Introduction

I here propose a method for reducing the ordinary differential equations (ODEs) of a reaction network including both fast and slow time-scale processes to those including only slow time-scale processes for the purpose of constructing the reliable phenomenological model of photosynthesis. This new method makes it possible to algebraically calculate the fast time-scale variables in a precise way, to evaluate the order of magnitude of the flux of each fast time-scale process, and to reduce a complex model including multi-time-scale processes to a simpler one only including slow time-scale processes. Consequently, an answer to the question of what processes govern the asymptotic behavior of an complex system at concerned time scale is given as a reduced model through application of time-coarse-graining scheme. If there exists a simple structure in a biological reaction network system including various intertwined multi-scale processes, the identification of the simple structure at each scale would imply the achievement of a deep understanding of the pertinent system. I would like to discuss a method of systematically reducing an complex model of a biological reaction system to such a simple one that emerges as a result of the interactions among the multi-scale layers, while finding such a phenomenological structure has often been attempted by intuition. The effect of this scheme for reducing the cost of understanding and computation will also be addressed.

In this chapter, I first present a reduction method for coarse-graining in time, which makes it possible to reduce a complex kinetic model to a simpler tractable

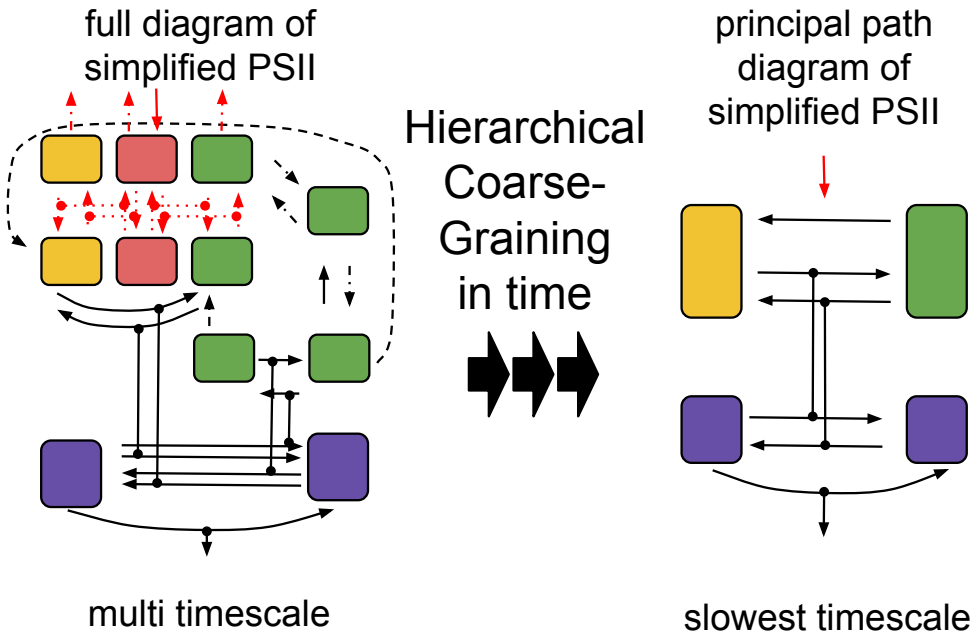

Figure 3.1 Graphical Abstract of Chapter 3

one on the basis of a prototypical three-variable reaction system. Then, I confirm the usefulness of this time-coarse-graining reduction method by applying it to a simplified photosystem II (PS II) model, which has multi-time-scale processes. The multi-time-scale coarse-graining reduction of the simplified PS II model can be achieved by applying the time-coarse-graining reduction method iteratively. Thus, I can extract the structure governed by dominant processes at each time-scale class from a model system with multi-scale property in time.

3.2 Theory

In this section, a prototypical three-variable reaction model that has a multi-time-scale property is discussed. This model is composed of reaction, inflow, and outflow processes. The characteristics of this model are having a nonlinear reaction process, fast reaction processes, and no fast inflow process (see Fig. 3.2). The characteristics listed above are common with a variety of biological reactions such as photosynthetic reactions. The effect of interactions between different time-scale reactions with each

other is an interesting problem about these reaction systems. A theoretical way to investigate such chain-like interactions is the analysis of ordinary differential equations (ODEs) of the full model, which simultaneously describe all multi-time-scale reaction processes in a system. However, there are some issues concerning this approach: (1) An intuitive understanding of the behavior of the system becomes more difficult as the number of components forming the system increases; (2) The computation cost increases as a wider variety of different time scales are considered. In order to overcome these difficulties, I study how to simplify and reduce such a complex multi-time-scale system to a combination of effective mono-time-scale systems. A full model for three time-dependent variables for the population, $x_i(t)$, which are analyzed in this section, is presented as

$$\begin{cases} \frac{dx_0}{dt} &= v_0 - k_0 x_0 + k_b x_2 - k_f x_1 x_0, \\ \frac{dx_1}{dt} &= v_1 - k_1 x_1 + k_b x_2 - k_f x_1 x_0, \\ \frac{dx_2}{dt} &= v_2 - k_2 x_2 - k_b x_2 + k_f x_1 x_0, \end{cases} \tag{3.1}$$

where v_0, v_1 and v_2 represent the slow inflows into the system. Reaction rates k_js are categorized into two groups according to their time scales. Two rate constants, k_b and k_0, which satisfy $1/k_b \ll 1/k_0$, are set as the characteristic rate constants for fast and slow groups, respectively: $A_{\mathrm{I}} = \{k_j \mid \mathcal{O}(k_j) \sim \mathcal{O}(k_b)\}$ and $A_{\mathrm{II}} = \{k_j \mid \mathcal{O}(k_j) \sim \mathcal{O}(k_0)\}$. k_f and k_b are fast rate constants of inner chemical reactions; k_0, k_1 and k_2 are the rate constants of outflows. The property of the system dynamics thus depends on the pattern of the time-scale-based classification of rate constants of outflows. I discuss three typical cases of the time-scale based classification of these outflow rate constants. The multi-time-scale property makes it possible to introduce dimensionless time parameters at each time scale. The dimensionless times are then expressed in terms of the characteristic rate constants at each time scale as $\tau_{\mathrm{I}} = k_b t$ and $\tau_{\mathrm{II}} = k_0 t$. $\varepsilon_{\mathrm{I,II}} = k_0/k_b$ represents the ratio of two time scales, which is assumed to be small. κ_j refers to dimensionless rate constants that are defined as each k_j normalized by the characteristic rate constants of time-scale groups to which each k_j belongs:

$$\kappa_j = \begin{cases} k_j/k_b & k_j \in A_{\mathrm{I}}, \\ k_j/k_0 & k_j \in A_{\mathrm{II}}, \end{cases} \tag{3.2}$$

where $\kappa_b = k_b/k_b = 1$, $\kappa_0 = k_0/k_0 = 1$ and all κ_js are of the order of unity. v_js are also normalized as $\nu_j = v_j/k_0$.

Here, I present a scheme that shows how to reduce the original ODE systems with

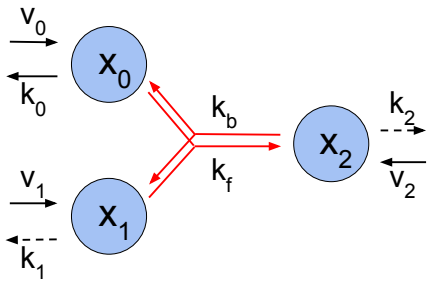

Figure 3.2 Three-variable reaction model. Blue circle: variable population, red arrow: fast reaction path, black solid arrow: slow reaction path. Black dashed arrow represents that the time scale of this path depends on the case.

time t, which have the characteristics addressed above, to the dimensionless ODE systems having small degrees of freedom with time τ_{II} characterized by a slower rate constant k_0, as the following steps.

0. To make the original ODEs with time t dimensionless, and to yield ODEs with $\tau_{\text{I}} \to \infty$: Dividing the original ODEs with t by the fast rate constant k_b yields the dimensionless ODEs for τ_{I}. Then, the dimensionless ODEs with $\tau_{\text{I}} \to \infty$ can be obtained.

1. Pseudo-steady-state approximation in the dimensionless ODEs with $\tau_{\text{I}} \to \infty$: Suppose a system which is formed by reaction paths having $\mathcal{O}(1)$ rate in the dimensionless ODEs with τ_{I}, and which is not affected by the reaction paths having $\mathcal{O}(\varepsilon_{\text{I,II}})$ rate. I then consider the following three cases.
   (a) If the system constructed above in the fast process has no outflow or inflow that allows interactions between the system and the environment, it is called a quasi-isolated system. In this case, there exist quasi-conserved quantities that change little with $\mathcal{O}(\varepsilon_{\text{I,II}})$ at the τ_{I} scale. Provided that the quasi-isolated system is in a quasi-equilibrium for $\tau_{\text{I}} \to \infty$, the system is in quasi-equilibrium pseudo-steady state that changes with $\mathcal{O}(\varepsilon_{\text{I,II}})$ rate. Then, the fast variables which change at the τ_{I} scale can be represented by a coarse-grained functions $\Gamma's$ of quasi-conserved quantities. These quasi-conserved quantities will be used as variables in the next step.

   (b) If the system constructed above is not quasi-isolated but has quasi-

conserved quantities, the quasi-equilibrium pseudo-steady-state approximation is not be applicable. In this case, fast variables that linearly decay with $\mathcal{O}(1)$ at $\tau_{\rm I}$ scale are assumed to be in nonequilibrium pseudo-steady state as $\tau_{\rm I} \to \infty$. Then, the fast variables which change at the $\tau_{\rm I}$ scale can be represented by a coarse-grained functions $\Gamma' s$ of quasi-conserved quantities. These quasi-conserved quantities will be used as variables in the next step.

(c) If the system constructed above is not a quasi-isolated system and does not have any quasi-conserved quantity, fast variables that vary with $\mathcal{O}(1)$ at the $\tau_{\rm I}$ scale are assumed to be in nonequilibrium quasi-steady state as $\tau_{\rm I} \to \infty$. Then, the fast variables which linearly decay at the $\tau_{\rm I}$ scale can be represented by a coarse-grained functions $\Gamma' s$ of slow variables. These slow variables will be used in the next step.

2. Transformation of the ODEs with $\tau_{\rm I} \to \infty$ to those with $\tau_{\rm II}$: Closed ODEs with $\tau_{\rm I} \to \infty$ that change by $\mathcal{O}(\varepsilon_{\rm I,II})$ at the $\tau_{\rm I}$ scale can be obtained by the application of step 1 to the ODEs with $\tau_{\rm I}$. Divided by $\varepsilon_{\rm I,II}$, the ODEs with $\tau_{\rm I} \to \infty$ can be translated into those with $\tau_{\rm II}$. Thus, we can obtain the ODEs with $\tau_{\rm II}$ that change by $\mathcal{O}(1)$ at the $\tau_{\rm II}$ scale. If one is interested only in the dynamics at the $\tau_{\rm II}$ scale, the $\mathcal{O}(\varepsilon_{\rm I,II})$ terms in the ODEs with $\tau_{\rm II}$ can be neglected.

I deal with three cases in which the classification of k_1 and k_2 according to time scales is different: (a) $k_0, k_1, k_2 \in A_{\rm II}$; (b) $k_0, k_2 \in A_{\rm II}, k_1 \in A_{\rm I}$; and (c) $k_0 \in A_{\rm II}, k_1, k_2 \in A_{\rm I}$. Each case corresponds to the case that should be approximated by (a), (b), and (c) in step 1, respectively, if the time-coarse-graining reduction method is applied to each case. This will be presented in more detail below.

a. Case of $k_0, k_1, k_2 \in A_{\rm II}$

To translate the ODEs with t to the dimensionless ODEs with $\tau_{\rm I}$, step 0 is applied. We thus find

$$\begin{cases} \frac{dx_0}{d\tau_{\rm I}} &= \varepsilon_{\rm I,II}\nu_0 - \varepsilon_{\rm I,II}\kappa_0 x_0 + \kappa_b x_2 - \kappa_f x_1 x_0, \\ \frac{dx_1}{d\tau_{\rm I}} &= \varepsilon_{\rm I,II}\nu_1 - \varepsilon_{\rm I,II}\kappa_1 x_1 + \kappa_b x_2 - \kappa_f x_1 x_0, \\ \frac{dx_2}{d\tau_{\rm I}} &= \varepsilon_{\rm I,II}\nu_2 - \varepsilon_{\rm I,II}\kappa_2 x_2 - \kappa_b x_2 + \kappa_f x_1 x_0. \end{cases} \tag{3.3}$$

Next, by applying step 1 (a) to the ODEs with $\tau_{\rm I}$, the quasi-equilibrium pseudo-

steady-state approximation is performed. The quasi-conserved quantities at the τ_{I} scale, $x_{02} = x_0(\tau_{\mathrm{I}}) + x_2(\tau_{\mathrm{I}})$ and $x_{12} = x_1(\tau_{\mathrm{I}}) + x_2(\tau_{\mathrm{I}})$, can be introduced. It is assumed that the reactions inside the quasi-isolated system, which proceed in the τ_{I} scale and consist of x_0, x_1 and x_2, are in quasi-equilibrium pseudo-steady states for $\tau_{\mathrm{I}} \to \infty$: $dx_0/d\tau_{\mathrm{I}} = 0, dx_1/d\tau_{\mathrm{I}} = 0$, and $dx_2/d\tau_{\mathrm{I}} = 0$. This approximation yields the following equation:

$$x_2 = \frac{\kappa_f}{\kappa_b} x_1 x_0. \tag{3.4}$$

Note that the processes of $\mathcal{O}(\varepsilon_{\mathrm{I,II}})$ at the τ_{I} scale are neglected in this treatment. By constructing a quadratic equation for x_0 by using Eq. (3.4) and the quasi-conserved quantities x_{02} and x_{12}, the solution to x_0 is obtained uniquely because of $x_0 > 0$. The forms of coarse-grained functions Γ, which hold at $\tau_{\mathrm{I}} \to \infty$ and represent x_0, x_1 and x_2 by the quasi-conserved quantities x_{02} and x_{12}, are thus derived as

$$\begin{aligned}
\lim_{\tau_{\mathrm{I}}\to\infty} x_0(\tau_{\mathrm{I}}) &= \Gamma_{x_0}(x_{02}, x_{12}) \\
&= \frac{\sqrt{(\kappa_b + \kappa_f x_{12} - \kappa_f x_{02})^2 + 4\kappa_f \kappa_b x_{02}} - (\kappa_b + \kappa_f x_{12} - \kappa_f x_{02})}{2\kappa_f}, \\
\lim_{\tau_{\mathrm{I}}\to\infty} x_1(\tau_{\mathrm{I}}) &= \Gamma_{x_1}(x_{02}, x_{12}) = \frac{x_{12}}{1 + \frac{\kappa_f}{\kappa_b}\Gamma_{x_0}(x_{02}, x_{12})}, \\
\lim_{\tau_{\mathrm{I}}\to\infty} x_2(\tau_{\mathrm{I}}) &= \Gamma_{x_2}(x_{02}, x_{12}) = x_{02} - \Gamma_{x_0}(x_{02}, x_{12}).
\end{aligned} \tag{3.5}$$

The ODEs with $\tau_{\mathrm{I}} \to \infty$ composed of the quasi-conserved quantities are derived by substituting these equations into Eq. (3.3). These ODEs change with the $\mathcal{O}(\varepsilon_{\mathrm{I,II}})$ rate for $\tau_{\mathrm{I}} \to \infty$.

Finally, step 2 is applied to the ODEs with $\tau_{\mathrm{I}} \to \infty$ for the coarse-graining transformation. That is, the ODEs are divided by $\varepsilon_{\mathrm{I,II}}$. Thus, the transformation from the ODEs with $\tau_{\mathrm{I}} \to \infty$ to those with τ_{II} is achieved as

$$\begin{cases} \frac{dx_{02}}{d\tau_{\mathrm{II}}} &= \nu_0 + \nu_2 - \kappa_0 \Gamma_{x_0}(x_{02}, x_{12}) - \kappa_2 \Gamma_{x_2}(x_{02}, x_{12}), \\ \frac{dx_{12}}{d\tau_{\mathrm{II}}} &= \nu_1 + \nu_2 - \kappa_1 \Gamma_{x_1}(x_{02}, x_{12}) - \kappa_2 \Gamma_{x_2}(x_{02}, x_{12}). \end{cases} \tag{3.6}$$

With respect to the ODEs composed of the terms that have $\mathcal{O}(1)$ rates at the τ_{I} scale, the relaxation time of the fast processes can be evaluated by the linear stability analysis [45]. In this analysis, the system is assumed to be in steady state. The solution $\bar{\boldsymbol{x}} = (\bar{x}_0, \bar{x}_1, \bar{x}_2)^{\mathrm{T}}$ of the ODEs that are in the steady state is called an equilibrium point. It is noted that $\bar{\boldsymbol{x}}$ is composed of non-negative values. The decay time

of the τ_{I}-scale reactions can be evaluated by the linear stability analysis of the point $\bar{\boldsymbol{x}} + \Delta\boldsymbol{x}$, which is displaced from the equilibrium point by $\Delta\boldsymbol{x} = (\Delta x_0, \Delta x_1, \Delta x_2)^{\mathrm{T}}$. The decay time can be analytically obtained by diagonalizing the Jacobian matrix for the ODEs of $\Delta\boldsymbol{x}$. The diagonalization can be carried out by transforming $\Delta\boldsymbol{x}$ to $\boldsymbol{y}$ via $\Delta\boldsymbol{x} = \mathbf{P}\boldsymbol{y}$, where $\mathbf{P} = (\mathbf{p_0}, \mathbf{p_1}, \mathbf{p_2})$; $\mathbf{p_0}, \mathbf{p_1}$ and $\mathbf{p_2}$ are eigenvectors of eigenvalues λ_1, λ_2 and λ_3 of the Jacobian matrix of ODEs of $\Delta\boldsymbol{x}$, respectively. As a result, the decay time of the perturbation $\Delta\boldsymbol{x}$ to the equilibrium point is evaluated as $\mathcal{O}(-1/\lambda_2)$, where λ_2 is the slowest decay component of the eigenvalues (see Appendix A.1).

b. Case of $k_0, k_2 \in A_{\mathrm{II}}, k_1 \in A_{\mathrm{I}}$

To translate the original ODEs with t to the dimensionless ODEs with τ_{I}, step 0 is applied, leading to

$$\begin{cases} \frac{dx_0}{d\tau_{\mathrm{I}}} &= \varepsilon_{\mathrm{I,II}}\nu_0 - \varepsilon_{\mathrm{I,II}}\kappa_0 x_0 + \kappa_b x_2 - \kappa_f x_1 x_0, \\ \frac{dx_1}{d\tau_{\mathrm{I}}} &= \varepsilon_{\mathrm{I,II}}\nu_1 - \kappa_1 x_1 + \kappa_b x_2 - \kappa_f x_1 x_0, \\ \frac{dx_2}{d\tau_{\mathrm{I}}} &= \varepsilon_{\mathrm{I,II}}\nu_2 - \varepsilon_{\mathrm{I,II}}\kappa_2 x_2 - \kappa_b x_2 + \kappa_f x_1 x_0. \end{cases} \tag{3.7}$$

With respect to the ODEs composed of the $\mathcal{O}(1)$ terms in Eq. (3.7), the relaxation time of the reactions at the τ_{I} scale can be evaluated by the linear stability analysis as well as through step 1 (a). The eigenvalues of Jacobian matrix of the ODEs for perturbation $\Delta\boldsymbol{x}$ around the equilibrium point can be obtained as

$$\lambda_0 = 0, \lambda_\pm = \frac{-[\kappa_1 + \kappa_b + \kappa_f(\bar{x}_0 + \bar{x}_1)] \pm \sqrt{[\kappa_1 + \kappa_b + \kappa_f(\bar{x}_0 + \bar{x}_1)]^2 - 4\kappa_1(\kappa_b + \kappa_f \bar{x}_1)}}{2}. \tag{3.8}$$

Thus, the slowest decay time of the ODEs with τ_{I} is evaluated as $\mathcal{O}(-1/\lambda_+)$ (see Appendix A.1).

Next, by applying step 1 (b) to the ODEs with τ_{I}, the nonequilibrium pseudo-steady-state approximation is performed. The quasi-conserved quantity at the τ_{I} scale, $x_{02} = x_0(\tau_{\mathrm{I}}) + x_2(\tau_{\mathrm{I}})$, can be introduced. It is then assumed that the reactions about the variables that linearly decay with the $\mathcal{O}(1)$ rate at the τ_{I} scale are in the nonequilibrium pseudo-steady states for $\tau_{\mathrm{I}} \to \infty$: $dx_1/d\tau_{\mathrm{I}} = 0$ and $dx_2/d\tau_{\mathrm{I}} = 0$ under the influence of the $\mathcal{O}(\varepsilon_{\mathrm{I,II}})$ terms. This approximation yields the following equations:

$$
\begin{aligned}
x_1 &= \frac{\kappa_b x_2 + \varepsilon_{\mathrm{I,II}}\nu_1}{\kappa_1 + \kappa_f x_0}, \\
x_2 &= \frac{\kappa_f x_1 x_0 + \varepsilon_{\mathrm{I,II}}\nu_2}{\kappa_b + \varepsilon_{\mathrm{I,II}}\kappa_2}.
\end{aligned}
\tag{3.9}
$$

Constructing the quadratic equation for x_2 by using Eq. (3.9) and the quasi-conserved quantity x_{02}, the solution to x_2 is obtained uniquely because of $x_2 > 0$. By expanding x_2 with $\varepsilon_{\mathrm{I,II}} \ll 1$ and considering up to the first order of $\varepsilon_{\mathrm{I,II}}$, the form of x_2 can be obtained as

$$
x_2 = \varepsilon_{\mathrm{I,II}} \frac{\kappa_f \nu_1 x_{02} + \nu_2(\kappa_1 + \kappa_f x_{02})}{\kappa_b \kappa_1} + \mathcal{O}(\varepsilon_{\mathrm{I,II}}^2). \tag{3.10}
$$

The forms of coarse-grained functions Γ that hold at $\tau_{\mathrm{I}} \to \infty$ and represent x_1 and x_2 by the quasi-conserved quantity x_{02} are thus derived from Eqs. (3.9) and (3.10) as

$$
\begin{aligned}
\lim_{\tau_{\mathrm{I}}\to\infty} x_1(\tau_{\mathrm{I}}) &= \varepsilon_{\mathrm{I,II}}\Gamma_{x_1}(x_{02}) + \mathcal{O}(\varepsilon_{\mathrm{I,II}}^2), \\
\lim_{\tau_{\mathrm{I}}\to\infty} x_2(\tau_{\mathrm{I}}) &= \varepsilon_{\mathrm{I,II}}\Gamma_{x_2}(x_{02}) + \mathcal{O}(\varepsilon_{\mathrm{I,II}}^2),
\end{aligned}
\tag{3.11}
$$

where

$$
\begin{aligned}
\Gamma_{x_1}(x_{02}) &= \frac{1}{\kappa_1 + \kappa_f x_{02}} \Big[\Gamma_{x_2}(x_{02}) + \nu_1 \Big], \\
\Gamma_{x_2}(x_{02}) &= \frac{\kappa_f \nu_1 x_{02} + \nu_2(\kappa_1 + \kappa_f x_{02})}{\kappa_b \kappa_1}.
\end{aligned}
\tag{3.12}
$$

The closed ODEs with $\tau_{\mathrm{I}} \to \infty$ composed of the quasi-conserved quantity are derived by substituting these equations into Eq. (3.7). These ODEs change with the $\mathcal{O}(\varepsilon_{\mathrm{I,II}})$ rate for $\tau_{\mathrm{I}} \to \infty$.

Finally, step 2 is applied to the ODEs with $\tau_{\mathrm{I}} \to \infty$ for the coarse-graining transformation. That is, the ODEs are divided by $\varepsilon_{\mathrm{I,II}}$. Thus, the transformation from the ODEs with $\tau_{\mathrm{I}} \to \infty$ to that with τ_{II} is achieved as

$$
\frac{dx_{02}}{d\tau_{\mathrm{II}}} = \nu_0 + \nu_2 - \kappa_0 \big[x_{02} - \varepsilon_{\mathrm{I,II}}\Gamma_{x_2}(x_{02}) \big] - \varepsilon_{\mathrm{I,II}}\kappa_2 \Gamma_{x_2}(x_{02}). \tag{3.13}
$$

c. Case of $k_0 \in A_{\mathrm{II}}, k_1, k_2 \in A_{\mathrm{I}}$

To translate the original ODEs with t to the dimensionless ODEs with τ_{I}, step 0 is applied. We thus find

$$\begin{cases} \frac{dx_0}{d\tau_{\mathrm{I}}} &= \varepsilon_{\mathrm{I,II}}\nu_0 - \varepsilon_{\mathrm{I,II}}\kappa_0 x_0 + \kappa_b x_2 - \kappa_f x_1 x_0, \\ \frac{dx_1}{d\tau_{\mathrm{I}}} &= \varepsilon_{\mathrm{I,II}}\nu_1 - \kappa_1 x_1 + \kappa_b x_2 - \kappa_f x_1 x_0, \\ \frac{dx_2}{d\tau_{\mathrm{I}}} &= \varepsilon_{\mathrm{I,II}}\nu_2 - \kappa_2 x_2 - \kappa_b x_2 + \kappa_f x_1 x_0. \end{cases} \tag{3.14}$$

Concerning the ODEs composed of the $\mathcal{O}(1)$ terms in Eq. (3.14), the relaxation time of the reactions at the τ_{I} scale can be evaluated by the linear stability analysis as well as through step 1 (a). The eigenvalues of the Jacobian matrix of the ODEs for the perturbation $\Delta\boldsymbol{x}$ around the equilibrium point can be obtained as

$$\begin{aligned} \lambda_0 &= \omega_1 \sqrt[3]{-q + \sqrt{q^2 + p^3}} + \omega_1 \sqrt[3]{-q - \sqrt{q^2 + p^3}} - \frac{1}{3}a, \\ \lambda_1 &= \omega_2 \sqrt[3]{-q + \sqrt{q^2 + p^3}} + \omega_3 \sqrt[3]{-q - \sqrt{q^2 + p^3}} - \frac{1}{3}a, \\ \lambda_2 &= \omega_3 \sqrt[3]{-q + \sqrt{q^2 + p^3}} + \omega_2 \sqrt[3]{-q - \sqrt{q^2 + p^3}} - \frac{1}{3}a, \end{aligned} \tag{3.15}$$

where $\omega_1 = 1, \omega_2 = \frac{-1+i\sqrt{3}}{2}, \omega_3 = \frac{-1-i\sqrt{3}}{2}, q = \frac{1}{2}c - \frac{1}{6}ab + \frac{1}{27}a^3$, and $p = \frac{1}{3}b - \frac{1}{9}a^2$. The details of a, b and c are described in Appendix A.1 Thus, the slowest decay time of the ODEs with τ_{I} is evaluated as $\mathcal{O}(-1/\lambda_0)$ (see Appendix A.1).

Next, by applying step 1 (c) to the ODEs with τ_{I}, the nonequilibrium pseudo-steady-state approximation is performed. In this case, there is no quasi-conserved quantity at the τ_{I} scale. It is assumed that the reactions of the variables that linearly decay with the $\mathcal{O}(1)$ rate at τ_{I} scale are in the nonequilibrium pseudo-steady states for $\tau_{\mathrm{I}} \to \infty$; $dx_1/d\tau_{\mathrm{I}} = 0$ and $dx_2/d\tau_{\mathrm{I}} = 0$ are considered under the influence of the $\mathcal{O}(\varepsilon_{\mathrm{I,II}})$ terms. This approximation yields the following equations:

$$\begin{aligned} x_1 &= \frac{\kappa_b x_2 + \varepsilon_{\mathrm{I,II}}\nu_1}{\kappa_1 + \kappa_f x_0}, \\ x_2 &= \frac{\kappa_f x_1 x_0 + \varepsilon_{\mathrm{I,II}}\nu_2}{\kappa_b + \kappa_2}. \end{aligned} \tag{3.16}$$

These equations can be arranged about x_1 and x_2 as

$$\begin{cases} \lim\limits_{\tau_{\mathrm{I}}\to\infty} x_1(\tau_{\mathrm{I}}) &= \varepsilon_{\mathrm{I,II}}\Gamma_{x_1}(x_0), \\ \lim\limits_{\tau_{\mathrm{I}}\to\infty} x_2(\tau_{\mathrm{I}}) &= \varepsilon_{\mathrm{I,II}}\Gamma_{x_2}(x_0), \\ \Gamma_{x_1}(x_0) &= \dfrac{\kappa_b\nu_2 + (\kappa_2 + \kappa_b)\nu_1}{(\kappa_2 + \kappa_b)(\kappa_1 + \kappa_f x_0) - \kappa_b\kappa_f x_0}, \\ \Gamma_{x_2}(x_0) &= \dfrac{\kappa_f}{\kappa_2 + \kappa_b}\big[\Gamma_{x_1}(x_0)x_0 + \dfrac{\nu_2}{\kappa_f}\big]. \end{cases} \tag{3.17}$$

The ODEs with $\tau_{\mathrm{I}} \to \infty$ constructed by the slow variable are derived by substituting these equations into Eq. (3.14). These ODEs change with the $\mathcal{O}(\varepsilon_{\mathrm{I,II}})$ rate for $\tau_{\mathrm{I}} \to \infty$.

Finally, step 2 is applied to the ODEs with $\tau_{\mathrm{I}} \to \infty$ for the coarse-graining transformation. That is, the ODEs are divided by $\varepsilon_{\mathrm{I,II}}$. Thus, the transformation from the ODEs with $\tau_{\mathrm{I}} \to \infty$ to that with τ_{II} is achieved as

$$\frac{dx_0}{d\tau_{\mathrm{II}}} = \nu_0 - \kappa_0 x_0 + \kappa_b \Gamma_{x_2}(x_0) - \kappa_f \Gamma_{x_1}(x_0) x_0. \tag{3.18}$$

Note that, in the three cases above, derived coarse-grained ODEs have different structures from each other depending on what processes are fast in the original model system. Figure 3.3 shows the results for the dynamics of x_0, which are computed on the basis of the original ODEs with time t, the ODEs composed only of $\mathcal{O}(1)$ terms at the τ_{I} scale, and the time-coarse-grained ODEs with τ_{II} in the case of (a), (b), and (c) above, respectively. The parameter values were set as $k_0 = 1, k_1 = 1$ or $1000, k_2 = 2$ or $2000, k_f = 3000, k_b = 1000, v_0 = 2, v_1 = 1$, and $v_2 = 3$. The results of both the ODEs composed only of $\mathcal{O}(1)$ terms at the τ_{I} scale and the time-coarse-grained ODEs with τ_{II} agree well with those of the original ODEs with time t at the fast and slow time scales, respectively. With respect to the original ODEs, the decay processes at the τ_{I} scale are represented by the former, and the slow processes at the τ_{II} scale are represented by the latter. These results show a clear separation of time scales τ_{I} and τ_{II}. The relaxation time to the pseudo-steady state at the τ_{I} scale can be evaluated through the linear stability analysis. The relaxation times in the (a), (b), and (c) cases are estimated as 1.9×10^{-4}, 7.9×10^{-3}, and 4.1×10^{-3}, respectively, by the linear stability analysis. The evaluated relaxation times are consistent with the calculated results of the ODEs composed only of $\mathcal{O}(1)$ terms at the τ_{I} scale. The relaxation times of the computed results do not depend on the initial values, where those of x_0, x_1, and x_2 are searched for the range between 0 and 2 under the constraint as $x_{02} = 2$ and $x_{12} = 1$ in the case (a) and $x_{02} = 2$ in the case (b).

3.3 Application to a simplified model for PS II

In this section, we investigate the usefulness of the time-coarse-graining scheme shown in the preceding section for the reduction of a system that has a multi-scale property in time. For such a system, I employ photosystem II (PS II) emitting Chlorophyll *a* fluorescence [29], which is often detected as an environmental response

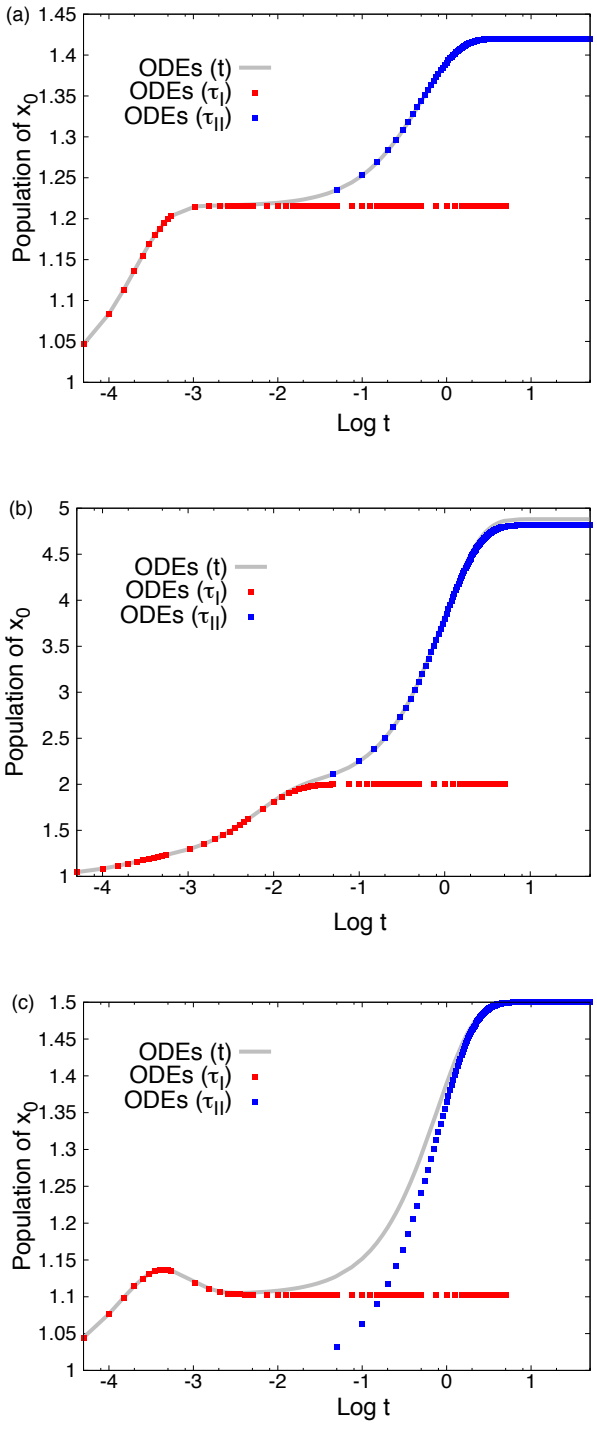

Figure 3.3 Calculated dynamics of x_0 in the cases of a, b and c. Grey line: the full ODE results with t (Eqs. (3.3), (3.7) and (3.14)), red squares: the ODE results with τ_{I} (Eqs. (A.1), (A.7) and (A.11)) and blue squares: the ODE results with τ_{II} (Eqs. (3.6), (3.13), and (3.18)). Initial values are set as $x_0 = 1$, $x_1 = 0$, and $x_2 = 1$. Parameters are set as $k_0 = 1, k_1 = 1$ or $1000, k_2 = 2$ or $2000, k_f = 3000, k_b = 1000, v_0 = 2, v_1 = 1$, and $v_2 = 3$.

of photosynthesis. Time-coarse-graining is applied to a simplified model of PS II, which simply describes the processes of excitation-energy and electron transfers in PS II, as illustrated in Fig. 3.4. Four different time scales coexist in the reactions of this model. The ODEs with time t are then given by

$$
\begin{cases}
\frac{dW_1(t)}{dt} &= \frac{W_0}{\mathrm{W_T}}\mathrm{v_I} - k_d W_1 - \frac{k_t}{\mathrm{R_T}}(X_0+Y_0)W_1 + \frac{k_{-t}}{\mathrm{W_T}}W_0(X_1+Y_1), \\
\frac{dX_0(t)}{dt} &= -\frac{k_t}{\mathrm{R_T}}X_0W_1 + \frac{k_{-t}}{\mathrm{W_T}}W_0X_1 + k_dX_1 + k_3X_4, \\
&\quad + \frac{k_4}{\mathrm{Z_T}}Z_0Y_0 - \frac{k_{-4}}{\mathrm{R_T}}X_0Z_1, \\
\frac{dX_1(t)}{dt} &= \frac{k_t}{\mathrm{R_T}}X_0W_1 - \frac{k_{-t}}{\mathrm{W_T}}W_0X_1 - k_1X_1 + k_{-1}X_2 - k_dX_1, \\
\frac{dX_2(t)}{dt} &= k_1X_1 - (k_2+k_{-1})X_2 + k_{-2}X_3, \\
\frac{dX_3(t)}{dt} &= k_2X_2 - (k_3 + \frac{k_4}{\mathrm{Z_T}}Z_0 + k_{-2})X_3 + \frac{k_{-4}}{\mathrm{R_T}}X_4Z_1, \\
\frac{dX_4(t)}{dt} &= -k_3X_4 - \frac{k_{-4}}{\mathrm{R_T}}X_4Z_1 + \frac{k_4}{\mathrm{Z_T}}Z_0X_3, \\
\frac{dY_0(t)}{dt} &= -\frac{k_t}{\mathrm{R_T}}Y_0W_1 + \frac{k_{-t}}{\mathrm{W_T}}W_0Y_1 + k_dY_1 + k_3X_3, \\
&\quad - \frac{k_4}{\mathrm{Z_T}}Z_0Y_0 + \frac{k_{-4}}{\mathrm{R_T}}X_0Z_1, \\
\frac{dY_1(t)}{dt} &= \frac{k_t}{\mathrm{R_T}}Y_0W_1 - \frac{k_{-t}}{\mathrm{W_T}}W_0Y_1 - k_dY_1, \\
\frac{dZ_1(t)}{dt} &= -k_5Z_1 + \frac{k_4}{\mathrm{Z_T}}Z_0(Y_0+X_3) - \frac{k_{-4}}{\mathrm{R_T}}(X_0+X_4)Z_1, \\
W_0(t) &= \mathrm{W_T} - W_1, \\
Z_0(t) &= \mathrm{Z_T} - Z_1,
\end{cases}
\tag{3.19}
$$

where W, X, Y and Z represent the concentrations of different states of the core antenna, the reaction center (the special pair, the first and second electron acceptor) and the final electron acceptor as follows. W_1: excited state of core antenna, W_0: ground state of core antenna, X_0: $[\mathrm{P_{680}PheQ}_A]$, X_1: $[\mathrm{P^*_{680}PheQ}_A]$, X_2: $[\mathrm{P^+_{680}Phe^-Q}_A]$, X_3: $[\mathrm{P^+_{680}PheQ}^-_A]$, Y_0: $[\mathrm{P_{680}PheQ}^-_A]$, Y_1: $[\mathrm{P^*_{680}PheQ}^-_A]$, Z_0: $[\mathrm{Q}_B]$, Z_1: $[\mathrm{Q}^-_B]$. The core antenna can take two possible states. The reaction center is characterized by the combination of the states of the special pair, the first and second electron acceptors. Each component of the reaction center takes two possible states; the special pair takes $\mathrm{P_{680}}$ or $\mathrm{P^+_{680}}$, the first electron acceptor takes Phe or $\mathrm{Phe^-}$, and the second electron acceptor takes Q_A or Q^-_A. However, the states $[\mathrm{P^+_{680}Phe^-Q}^-_A]$, $[\mathrm{P_{680}Phe^-Q}^-_A]$ and $[\mathrm{P_{680}PheQ}^-_A\ ]$, which are not easily realized kinetically, are neglected for simplicity. The special pair can transition to the excited state $\mathrm{P^*_{680}}$ only in the reaction center in

which both the special pair and the first electron acceptor are in the ground (neutral) states. The final electron acceptor takes two possible states Q_B and Q_B^-. The index 0 of each variable represents the ground (neutral) state.

The parameters of the simplified model of PS II are described in Table 1. The parameters that belong to significantly different time scales coexist in this model. To clearly represent the multi-time-scale property, time scales are characterized by the representative rate constants, k_t, k_2, k_3, k_{-2}, where these parameters satisfy the following relation: $1/k_t \ll 1/k_2 \ll 1/k_3 \ll 1/k_{-2}$. That is, the hierarchical structure in the time scale of this system is formed by four classes. The rate constants are classified on the basis of their time scales as follows: $A_{\mathrm{I}} = \{k_j \mid \mathcal{O}(k_j) \sim \mathcal{O}(k_t)\}$, $A_{\mathrm{II}} = \{k_j \mid \mathcal{O}(k_j) \sim \mathcal{O}(k_2)\}$, $A_{\mathrm{III}} = \{k_j \mid \mathcal{O}(k_j) \sim \mathcal{O}(k_3)\}$, and $A_{\mathrm{IV}} = \{k_j \mid \mathcal{O}(k_j) \sim \mathcal{O}(k_{-2})\}$.

The dimensionless times $\tau_{\mathrm{I}}, \tau_{\mathrm{II}}, \tau_{\mathrm{III}}$, and τ_{IV} normalized by the characteristic rate constants of each time scale are introduced as $\tau_{\mathrm{I}} = k_t t, \tau_{\mathrm{II}} = k_2 t, \tau_{\mathrm{III}} = k_3 t$ and $\tau_{\mathrm{IV}} = k_{-2} t$. The ratios of the time scales are introduced as

$$\begin{aligned} \varepsilon_{\mathrm{I,II}} &= k_2/k_t, \\ \varepsilon_{\mathrm{II,III}} &= k_3/k_2, \\ \varepsilon_{\mathrm{III,IV}} &= k_{-2}/k_3, \\ \varepsilon_{\mathrm{II,IV}} &= \varepsilon_{\mathrm{II,III}}\varepsilon_{\mathrm{III,IV}} = k_{-2}/k_2, \end{aligned} \tag{3.20}$$

which satisfy the following relations: $\varepsilon_{\mathrm{II,IV}} \ll \varepsilon_{\mathrm{I,II}} \sim \varepsilon_{\mathrm{II,III}} \sim \varepsilon_{\mathrm{III,IV}} \ll 1$.

The time-coarse-grained reduction of a reaction system that has a multi-time-scale property as described above is attempted in the following by applying repeatedly the time-coarse-graining scheme described in Sec. 3.2. It is shown that the reduction of the simplified PS II model from the τ_{I} scale to the τ_{IV} scale is realized by applying the time-coarse-graining scheme three times iteratively.

3.3.1 the ODEs (τ_{I}) $\rightarrow$ the ODEs (τ_{II})

To translate the original ODEs with t to the dimensionless ODEs with τ_{I}, step 0 is applied, i.e., Eq. (3.19) is divided by k_t. The ODEs having $\mathcal{O}(1)$ rates at the τ_{I} scale are given by

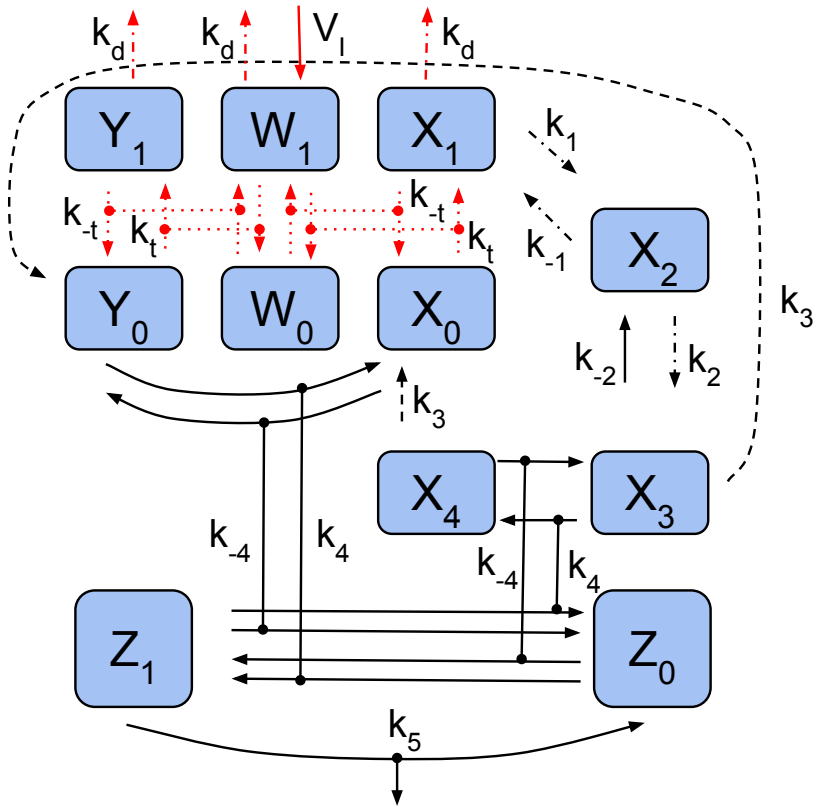

Figure 3.4 Diagram of the simplified model of PSII. Each box indicates each state variable. Dotted line: reactions at A_{I} scale, chain line: A_{II} scale, dashed line: A_{III} scale, solid line: A_{IV} scale. Black and red lines indicate electron transfer and excitation-energy transfer (or photon-flux), respectively.

$$
\begin{cases}
\dfrac{dW_1}{d\tau_{\mathrm{I}}} &= -\dfrac{\kappa_t}{\mathrm{R_T}}(X_0+Y_0)W_1 + \dfrac{\kappa_{-t}}{\mathrm{W_T}}W_0(X_1+Y_1), \\
\dfrac{dX_1}{d\tau_{\mathrm{I}}} &= \dfrac{\kappa_t}{\mathrm{R_T}}X_0W_1 - \dfrac{\kappa_{-t}}{\mathrm{W_T}}W_0X_1, \\
\dfrac{dX_0}{d\tau_{\mathrm{I}}} &= -\dfrac{\kappa_t}{\mathrm{R_T}}X_0W_1 + \dfrac{\kappa_{-t}}{\mathrm{W_T}}W_0X_1, \\
\dfrac{dY_1}{d\tau_{\mathrm{I}}} &= \dfrac{\kappa_t}{\mathrm{R_T}}Y_0W_1 - \dfrac{\kappa_{-t}}{\mathrm{W_T}}W_0Y_1, \\
\dfrac{dY_0}{d\tau_{\mathrm{I}}} &= -\dfrac{\kappa_t}{\mathrm{R_T}}Y_0W_1 + \dfrac{\kappa_{-t}}{\mathrm{W_T}}W_0Y_1.
\end{cases}
\tag{3.21}
$$

The reaction processes expressed by these ODEs constitute a quasi-isolated system at the τ_{I} scale. Then, step 1 (a) in Sec. 3.2 is applied to this system. The quasi-conserved quantities, U_1, X_{01} and Y_{01}, are introduced as $U_1 = W_1 + X_1 + Y_1$, $X_{01} =$

Table 3.1 Table 1: List of parameters of simplified PSII model.

description	notation	time scale class	value
rate constant of excitation transfer from core antenna to special pair	k_t	A_{I}	$2 \times 10^{13}\mathrm{s}^{-1}$
rate constant of excitation transfer from special pair to core antenna	k_{-t}	A_{I}	$\mathrm{k}_t \exp[\frac{hc(1/\lambda_{Chl}-1/\lambda_p)}{k_B T}]^* \mathrm{s}^{-1}$
rate constant of excitation dissipation from core antenna	k_d	A_{II}	$10^8\mathrm{s}^{-1}$
rate constant of charge separation in open (Q_A is neutral) reaction center	k_1	A_{II}	$2.5 \times 10^{10}\mathrm{s}^{-1}$
rate constant of charge recombination in open reaction center	k_{-1}	A_{II}	$3 \times 10^8\mathrm{s}^{-1}$
rate constant of electron transfer from Pheo^- to Q_A	k_2	A_{II}	$2 \times 10^9\mathrm{s}^{-1}$
rate constant of electron transfer from Q_A^- to Pheo^-	k_{-2}	A_{IV}	$2 \times 10^3\mathrm{s}^{-1}$
radiation flux density to core antenna	v_{I}	A_{IV}	$1,000\ \mu\mathrm{mol\ m}^{-2}\ \mathrm{s}^{-1}$
rate constant of electron transfer from OEC to P_{680}^+	k_3	A_{III}	$5 \times 10^6\mathrm{s}^{-1}$
rate constant of electron transfer from Q_A^- to Q_B	k_4	A_{IV}	$2,500\mathrm{s}^{-1}$
rate constant of electron transfer from Q_B^- to Q_A	k_{-4}	A_{IV}	$175\mathrm{s}^{-1}$
rate constant of electron transfer from Q_B^- to downstream (plastoquinone)	k_5	A_{IV}	$800\mathrm{s}^{-1}$
concentration of all reaction center's states (conserved quantity)	R_{T}	-	$1\ \mu\mathrm{mol\ m}^{-2}$
concentration of all Q_B's states (conserved quantity)	Z_{T}	-	$1\ \mu\mathrm{mol\ m}^{-2}$
concentration of all core antenna's states (conserved quantity)	W_{T}	-	$70\ \mu\mathrm{mol\ m}^{-2}$

* k_B: Boltzmann constant, h: Planck's constant, c: speed of light, T: temperature (298K), λ_{Chl}: wavelength of the maximum absorbance of antenna chlorophyll (678nm), λ_p: wavelength of the maximum absorbance of special pair (680nm).

$X_0 + X_1$ and $Y_{01} = Y_0 + Y_1$. It is assumed that the reactions inside the quasi-isolated system of Eq. (3.21), which proceed at the τ_{I} scale, are in the quasi-equilibrium pseudo-steady state for $\tau_{\mathrm{I}} \to \infty$: $dW_1/d\tau_{\mathrm{I}} = 0$, $dX_1/d\tau_{\mathrm{I}} = 0$ and $dY_1/d\tau_{\mathrm{I}} = 0$. Note that the processes of $\mathcal{O}(\varepsilon_{\mathrm{I,II}})$ at the τ_{I} scale are neglected in the above treatment. This approximation yields the following coarse-grained functions Γ, which hold for $\tau_{\mathrm{I}} \to \infty$, and represent W_1, X_1 and Y_1 by the quasi-conserved quantities, U_1, X_{01} and Y_{01}:

$$
\begin{aligned}
\lim_{\tau_{\mathrm{I}}\to\infty} W_1(\tau_{\mathrm{I}}) &= \frac{-[\frac{\kappa_t}{\mathrm{R_T}}(X_{01}+Y_{01}) + \kappa_{-t} - \alpha U_1] + \sqrt{[\frac{\kappa_t}{\mathrm{R_T}}(X_{01}+Y_{01}) + \kappa_{-t} - \alpha U_1]^2 + 4\alpha\kappa_{-t}U_1}}{2\alpha} \\
&\equiv \Gamma_{W_1}(U_1, X_{01}, Y_{01}), \\
\lim_{\tau_{\mathrm{I}}\to\infty} X_1(\tau_{\mathrm{I}}) &= \frac{\frac{\kappa_t}{\mathrm{R_T}} X_{01}}{\frac{\kappa_t}{\mathrm{R_T}}\Gamma_{W_1} + \frac{\kappa_{-t}}{\mathrm{W_T}}(\mathrm{W_T} - \Gamma_{W_1})} \equiv \Gamma_{X_1}(U_1, X_{01}, Y_{01}), \\
\lim_{\tau_{\mathrm{I}}\to\infty} Y_1(\tau_{\mathrm{I}}) &= \frac{\frac{\kappa_t}{\mathrm{R_T}} Y_{01}}{\frac{\kappa_t}{\mathrm{R_T}}\Gamma_{W_1} + \frac{\kappa_{-t}}{\mathrm{W_T}}(\mathrm{W_T} - \Gamma_{W_1})} \equiv \Gamma_{Y_1}(U_1, X_{01}, Y_{01}),
\end{aligned}
\tag{3.22}
$$

where $\alpha \equiv \kappa_t/\mathrm{R_T} - \kappa_{-t}/\mathrm{W_T}$. By substituting these equations into Eq. (3.19) and using the definitional equations for quasi-conserved quantities, the ODEs of quasi-conserved quantities that hold for $\tau_{\mathrm{I}} \to \infty$ are obtained. These ODEs change with $\mathcal{O}(\varepsilon_{\mathrm{I,II}})$ rates as $\tau_{\mathrm{I}} \to \infty$.

Then, step 2 is applied to the ODEs with $\tau_{\mathrm{I}} \to \infty$ for the coarse-graining transfor-

mation. That is, divided by $\varepsilon_{\mathrm{I,II}}$, the transformation from the ODEs with $\tau_{\mathrm{I}} \to \infty$ to those with τ_{II} can be achieved. The ODEs that change with $\mathcal{O}(1)$ rates at the τ_{II} scale are expressed as follows:

$$
\begin{cases}
\frac{dU_1}{d\tau_{\mathrm{II}}} & = -\kappa_d U_1 - \kappa_1 \Gamma_{X_1}(U_1, X_{01}, Y_{01}) + \kappa_{-1} X_2 + \varepsilon_{\mathrm{II,IV}} \nu_{\mathrm{I}}, \\
\frac{dX_{01}}{d\tau_{\mathrm{II}}} & = -\kappa_1 \Gamma_{X_1}(U_1, X_{01}, Y_{01}) + \kappa_{-1} X_2 + \varepsilon_{\mathrm{II,III}} \kappa_3 X_4 \\
& \quad + \varepsilon_{\mathrm{II,IV}} \frac{\kappa_4}{\mathrm{Z_T}} [Y_{01} - \Gamma_{Y_1}(U_1, X_{01}, Y_{01})] Z_0 \\
& \quad - \varepsilon_{\mathrm{II,IV}} \frac{\kappa_{-4}}{\mathrm{R_T}} [X_{01} - \Gamma_{X_1}(U_1, X_{01}, Y_{01})] Z_1, \\
\frac{dX_2}{d\tau_{\mathrm{II}}} & = \kappa_1 \Gamma_{X_1}(U_1, X_{01}, Y_{01}) - (\kappa_2 + \kappa_{-1}) X_2 + \varepsilon_{\mathrm{II,IV}} \kappa_{-2} X_3, \\
\frac{dX_3}{d\tau_{\mathrm{II}}} & = \kappa_2 X_2 - (\varepsilon_{\mathrm{II,III}} \kappa_3 + \varepsilon_{\mathrm{II,IV}} \frac{\kappa_4}{\mathrm{Z_T}} Z_0 + \varepsilon_{\mathrm{II,IV}} \kappa_{-2}) X_3 \\
& \quad + \varepsilon_{\mathrm{II,IV}} \frac{\kappa_{-4}}{\mathrm{R_T}} X_4 Z_1, \\
Y_{01} & = \mathrm{R_T} - (X_{01} + X_2 + X_3 + X_4).
\end{cases}
\tag{3.23}
$$

3.3.2 the ODEs (τ_{II}) $\to$ the ODEs (τ_{III})

The reaction processes at the τ_{II} scale presented in Eq. (3.23) do not form a quasi-isolated system. Then, step 1 (c) in Sec. 3.2 is applied to this system. In this system, the variables that linearly decay with $\mathcal{O}(1)$ rates at the τ_{II} scale are U_1 and X_2. The total inflow and outflow of the processes related to these variables are assumed to be balanced for $\tau_{\mathrm{II}} \to \infty$, that is, the nonequilibrium pseudo-steady-state approximation is applied: $dU_1/d\tau_{\mathrm{II}} = 0$ and $dX_2/d\tau_{\mathrm{II}} = 0$. As a result, the coarse-grained functions that hold for $\tau_{\mathrm{II}} \to \infty$ and represent U_1 and X_2 by the slower variables are obtained as

$$
\begin{aligned}
\lim_{\tau_{\mathrm{II}} \to \infty} U_1(\tau_{\mathrm{II}}) &= \varepsilon_{\mathrm{II,IV}} \frac{\nu_I + \kappa_{-2} \gamma^b_{X_2} X_3}{\kappa_d + \beta \kappa_1 \gamma^f_{X_2}}, \\
&\equiv \varepsilon_{\mathrm{II,IV}} \Gamma_{U_1}(X_{01}, Y_{01}, X_3), \\
\lim_{\tau_{\mathrm{II}} \to \infty} X_2(\tau_{\mathrm{II}}) &= \varepsilon_{\mathrm{II,IV}} \frac{\kappa_1 \beta \Gamma_{U_1} + \kappa_{-2} X_3}{\kappa_2 + \kappa_{-1}},
\end{aligned}
\tag{3.24}
$$

where $\Gamma_{X_1}(U_1, X_{01}, Y_{01})$ is expressed by βU_1 with $0 < \beta < 1$. Besides, $\gamma^f_{X_2} \equiv \kappa_2/(\kappa_2 + \kappa_{-1})$ and $\gamma^b_{X_2} \equiv \kappa_{-1}/(\kappa_2 + \kappa_{-1})$ are introduced, which indicate the ratios of forward and backward outflows to total outflow from X_2, respectively. Equation (3.24) suggests $U_1 \sim \mathcal{O}(\varepsilon_{\mathrm{II,IV}}) \ll 1$. Concerning Eq. (3.22), by expanding W_1 by U_1, and X_1 and Y_1 by $W_1 (< U_1)$, considering up to the first order of $\mathcal{O}(\varepsilon_{\mathrm{II,IV}})$, W_1, X_1 and Y_1 are represented as

$$
\begin{aligned}
\lim_{\tau_{\mathrm{II}}\to\infty} W_1(\tau_{\mathrm{II}}) &= \varepsilon_{\mathrm{II,IV}}\Gamma_{U_1}\big(1+\frac{\kappa_t}{\kappa_{-t}}\frac{X_{01}+Y_{01}}{\mathrm{R_T}}\big)^{-1},\\
\lim_{\tau_{\mathrm{II}}\to\infty} X_1(\tau_{\mathrm{II}}) &= \lim_{\tau_{\mathrm{II}}\to\infty} U_1\big(\frac{\kappa_{-t}}{\kappa_t}\frac{\mathrm{R_T}}{X_{01}+Y_{01}}+1\big)^{-1}\frac{X_{01}}{X_{01}+Y_{01}}\\
&= \varepsilon_{\mathrm{II,IV}}\Gamma_{U_1}p(X_1+Y_1\mid U_1)\frac{X_{01}}{X_{01}+Y_{01}}\\
&\equiv \varepsilon_{\mathrm{II,IV}}\Gamma_{X_1}(X_{01},Y_{01},X_3),\\
\lim_{\tau_{\mathrm{II}}\to\infty} Y_1(\tau_{\mathrm{II}}) &= \lim_{\tau_{\mathrm{II}}\to\infty} U_1\big(\frac{\kappa_{-t}}{\kappa_t}\frac{\mathrm{R_T}}{X_{01}+Y_{01}}+1\big)^{-1}\frac{Y_{01}}{X_{01}+Y_{01}}\\
&= \varepsilon_{\mathrm{II,IV}}\Gamma_{U_1}p(X_1+Y_1\mid U_1)\frac{Y_{01}}{X_{01}+Y_{01}}\\
&\equiv \varepsilon_{\mathrm{II,IV}}\Gamma_{Y_1}(X_{01},Y_{01},X_3),
\end{aligned}
\tag{3.25}
$$

where the partition ratio of U_1 (population of total exciton in PS II) at the reaction center (total concentration $\mathrm{R_T}$), $p(X_1+Y_1\mid U_1)\equiv[\kappa_{-t}/\kappa_t\cdot\mathrm{R_T}/(X_{01}+Y_{01})+1]^{-1}$, has been introduced. Equation (3.25) indicates $\beta=p(X_1+Y_1\mid U_1)X_{01}/(X_{01}+Y_{01})$. By substituting Eqs. (3.24) and (3.25) into Eq. (3.23), the ODEs with $\tau_{\mathrm{II}}\to\infty$ are obtained.

The transformation from the ODEs with $\tau_{\mathrm{II}}\to\infty$ to those with τ_{III} is achieved by applying step 2, i.e., by dividing the ODEs with $\tau_{\mathrm{II}}\to\infty$ by $\varepsilon_{\mathrm{II,III}}$. The ODEs that change with $\mathcal{O}(1)$ rates at the τ_{III} scale are thus given by

$$
\begin{cases}
\dfrac{dX_{01}}{d\tau_{\mathrm{III}}} &= -\varepsilon_{\mathrm{III,IV}}\kappa_1\gamma^f_{X_2}\Gamma_{X_1}(X_{01},Y_{01},X_3)+\kappa_3X_4+\varepsilon_{\mathrm{III,IV}}\kappa_{-2}\gamma^b_{X_2}X_3\\
&\quad+\varepsilon_{\mathrm{III,IV}}\dfrac{\kappa_4}{\mathrm{Z_T}}Y_{01}Z_0-\varepsilon_{\mathrm{III,IV}}\dfrac{\kappa_{-4}}{\mathrm{R_T}}X_{01}Z_1,\\
\dfrac{dX_3}{d\tau_{\mathrm{III}}} &= \varepsilon_{\mathrm{III,IV}}\kappa_1\gamma^f_{X_2}\Gamma_{X_1}(X_{01},Y_{01},X_3)\\
&\quad-(\kappa_3+\varepsilon_{\mathrm{III,IV}}\dfrac{\kappa_4}{\mathrm{Z_T}}Z_0+\varepsilon_{\mathrm{III,IV}}\kappa_{-2}\gamma^b_{X_2})X_3\\
&\quad+\varepsilon_{\mathrm{III,IV}}\dfrac{\kappa_{-4}}{\mathrm{R_T}}X_4Z_1,\\
\dfrac{dX_4}{d\tau_{\mathrm{III}}} &= -\kappa_3X_4-\varepsilon_{\mathrm{III,IV}}\dfrac{\kappa_{-4}}{\mathrm{R_T}}X_4Z_1+\varepsilon_{\mathrm{III,IV}}\dfrac{\kappa_4}{\mathrm{Z_T}}Z_0X_3,
\end{cases}
\tag{3.26}
$$

where the terms of $\mathcal{O}(\varepsilon_{\mathrm{III,IV}}\varepsilon_{\mathrm{II,IV}})$ at the τ_{III} scale are neglected.

3.3.3 the ODEs (τ_{III}) $\to$ the ODEs (τ_{IV})

The processes at the τ_{III} scale presented in Eq. (3.26) do not form a quasi-isolated system. Then, step 1 (c) in Sec. 3.2 is applied to this system. In this system, the

variables that linearly decay with $\mathcal{O}(1)$ rates at the τ_{III} scale are X_3 and X_4. The total inflow and outflow of the processes related to these variables are assumed to be balanced for $\tau_{\mathrm{III}} \to \infty$, that is, the nonequilibrium pseudo-steady-state approximation is applied: $dX_3/d\tau_{\mathrm{III}} = 0$ and $dX_4/d\tau_{\mathrm{III}} = 0$. As a result, the equations that hold for $\tau_{\mathrm{III}} \to \infty$ and represent X_3 and X_4 by the slower variables are obtained. The coarse-grained functions that are expanded by $\varepsilon_{\mathrm{III,IV}}$ are

$$\begin{aligned}
\lim_{\tau_{\mathrm{III}}\to\infty} X_3(\tau_{\mathrm{III}}) &= \varepsilon_{\mathrm{III,IV}}\gamma^f_{U_1}\nu_I[1+\varepsilon_{\mathrm{III,IV}}(\kappa_{-2}\gamma^b_{X_2}\gamma^f_{U_1} - \frac{\kappa_4}{\mathrm{Z_T}}Z_0 - \kappa_1\gamma^f_{X_2})] + \mathcal{O}(\varepsilon^3_{\mathrm{III,IV}}) \\
&\equiv \varepsilon_{\mathrm{III,IV}}\Gamma_{X_3}(X_{01}, Y_{01}, Z_0), \\
\lim_{\tau_{\mathrm{III}}\to\infty} X_4(\tau_{\mathrm{III}}) &= \varepsilon^2_{\mathrm{III,IV}}\gamma^f_{U_1}\nu_I\frac{\kappa_4}{\mathrm{Z_T}}Z_0 + \mathcal{O}(\varepsilon^3_{\mathrm{III,IV}}) \\
&\equiv \varepsilon^2_{\mathrm{III,IV}}\Gamma_{X_4}(X_{01}, Y_{01}, Z_0),
\end{aligned} \tag{3.27}$$

where the ratio of forward outflow via charge separation to total outflow from U_1:

$$\gamma^f_{U_1} \equiv \frac{\kappa_1\gamma^f_{X_2}p(X_1+Y_1 \mid U_1)\frac{X_{01}}{X_{01}+Y_{01}}}{\kappa_d + \kappa_1\gamma^f_{X_2}p(X_1+Y_1 \mid U_1)\frac{X_{01}}{X_{01}+Y_{01}}}, \tag{3.28}$$

is introduced. By substituting Eq. (3.27) into Eq. (3.26), the ODEs with $\tau_{\mathrm{III}} \to \infty$ are obtained.

The transformation from the ODEs with $\tau_{\mathrm{III}} \to \infty$ to those with τ_{IV} is achieved by applying step 2, i.e., by dividing the ODEs with $\tau_{\mathrm{III}} \to \infty$ by $\varepsilon_{\mathrm{III,IV}}$. The ODEs with τ_{IV} are thus given by

$$\begin{cases}
\dfrac{dX_{01}}{d\tau_{\mathrm{IV}}} &= -\kappa_1\gamma^f_{X_2}\Gamma_{X_1} + \varepsilon_{\mathrm{III,IV}}\kappa_3\Gamma_{X_4} + \varepsilon_{\mathrm{III,IV}}\kappa_{-2}\gamma^b_{X_2}\Gamma_{X_3} \\
&\quad + \dfrac{\kappa_4}{\mathrm{Z_T}}(\mathrm{Z_T}-Z_1)Y_{01} - \dfrac{\kappa_{-4}}{\mathrm{R_T}}X_{01}Z_1, \\
\dfrac{dY_{01}}{d\tau_{\mathrm{IV}}} &= \Gamma_{X_3} - \dfrac{\kappa_4}{\mathrm{Z_T}}(\mathrm{Z_T}-Z_1)Y_{01} + \dfrac{\kappa_{-4}}{\mathrm{R_T}}X_{01}Z_1, \\
\dfrac{dZ_1}{d\tau_{\mathrm{IV}}} &= -\kappa_5 Z_1 + \dfrac{\kappa_4}{\mathrm{Z_T}}(\mathrm{Z_T}-Z_1)(Y_{01}+\varepsilon_{\mathrm{III,IV}}\Gamma_{X_3}) - \dfrac{\kappa_{-4}}{\mathrm{R_T}}(X_{01}+\varepsilon^2_{\mathrm{III,IV}}\Gamma_{X_4})Z_1.
\end{cases} \tag{3.29}$$

In particular, by neglecting the terms of $\mathcal{O}(\varepsilon_{\mathrm{III,IV}})$, the ODEs with τ_{IV} are concisely represented as

$$\begin{cases}
\dfrac{dX_{01}}{d\tau_{\mathrm{IV}}} &= -\nu_I\gamma^f_{U_1} + \dfrac{\kappa_4}{\mathrm{Z_T}}(\mathrm{Z_T}-Z_1)(\mathrm{R_T}-X_{01}) - \dfrac{\kappa_{-4}}{\mathrm{R_T}}X_{01}Z_1, \\
\dfrac{dZ_1}{d\tau_{\mathrm{IV}}} &= \dfrac{\kappa_4}{\mathrm{Z_T}}(\mathrm{R_T}-X_{01})(\mathrm{Z_T}-Z_1) - \dfrac{\kappa_{-4}}{\mathrm{R_T}}X_{01}Z_1 - \kappa_5 Z_1,
\end{cases} \tag{3.30}$$

where the relation $\kappa_1 \gamma^f_{X_2} \Gamma_{X_1} = \nu_I \gamma^f_{U_1}$ is used, and the relations $X_{01} + Y_{01} = \mathrm{R_T}$ and $p(X_1 + Y_1 \mid U_1) = (\kappa_{-t}/\kappa_t + 1)^{-1}$ hold.

To represent these ODEs in a simpler way, each variable and parameter are normalized as follows: $X_{01}/\mathrm{R_T} = X$, $Z_1/\mathrm{Z_T} = Z$ and $\nu_I/\mathrm{R_T} = \nu$. They indicate the occupancy ratio of each state and the incidence rate of photo-excitation per PS II. Besides, by assuming $\mathrm{R_T} = \mathrm{Z_T}$, which is a natural assumption, Eq. (3.30) is represented as

$$\begin{cases} \dfrac{dX}{d\tau} &= -\nu \dfrac{\kappa_1' X}{\kappa_d + \kappa_1' X} + \kappa_4 (1 - X)(1 - Z) - \kappa_{-4} X Z, \\ \dfrac{dZ}{d\tau} &= \kappa_4 (1 - X)(1 - Z) - \kappa_{-4} X Z - \kappa_5 Z, \end{cases} \tag{3.31}$$

where τ_{IV} is replaced by τ, and $\kappa_1' \equiv \kappa_1 \gamma^f_{X_2} p(X_1 + Y_1 \mid U_1)$ is introduced.

3.3.4 Results and Discussion

The calculated results of four different time-scale variables of the full ODEs with t and the reduced ODEs obtained by the time-coarse-graining method are shown in Figs. 3.5 and 3.6. Each time step of integration of the full ODEs with t, ODEs with τ_{II}, ODEs with τ_{III}, and ODEs with τ_{IV} is set as 10^{-13}s, 10^{-11}s, 5×10^{-8}s, and 10^{-5}s, respectively. The integration of each reduced ODE is computed up to 0.1 s and that of the full ODEs is computed up to 0.01 s. Initial values of the variables are set as those for non-reduced states under the assumption that the system is dark adapted: $X_0 = 1$, $Z_0 = 1$, and otherwise 0. The values of the relevant variables and those of the fast variables at each time scale of the ODEs are calculated by integrating the ODEs and through the coarse-grained functions, respectively. All of the results of the reduced ODEs are in good agreement with those of the full ODEs at each time-scale range of each reduced ODE (see Fig. 3.5). This result indicates that the time-coarse-graining method adequately yields the effective reduced ODEs at each time scale. The calculated results for the variables of the reduced ODEs, which are not shown here, are also in good agreement with those of the full ODEs. The comparison between the results of the ODEs with τ_{IV} neglecting $\mathcal{O}(\varepsilon^2_{\mathrm{III,IV}})$ terms (see Appendix A.2) and those neglecting $\mathcal{O}(\varepsilon_{\mathrm{III,IV}})$ terms are shown in Fig. 3.6. This result suggests that Eq. (3.30) consisting of two variables appropriately describes the dynamics of the simplified PS II model consisting of nine variables at the τ_{IV} scale, because both the ODEs neglecting the $\mathcal{O}(\varepsilon^2_{\mathrm{III,IV}})$ terms and those neglecting $\mathcal{O}(\varepsilon_{\mathrm{III,IV}})$ terms represent the full ODEs fairly

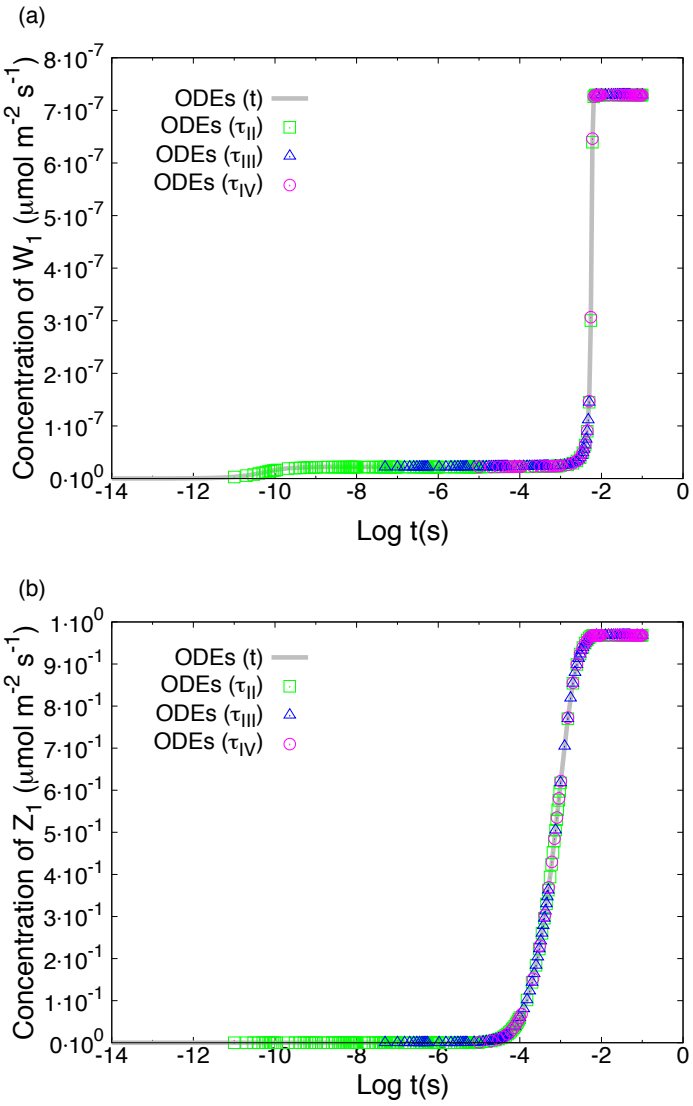

Figure 3.5 Computed dynamics of (a) W_1 and (b) Z_1 concentrations. Grey line: the results of full ODEs with t, open square (green): the ODE results with τ_{II}, open triangle (blue): the ODE results with τ_{III}, and open circle (magenta): the ODE results with τ_{IV}. The full ODEs are computed up to 0.01 s. Details of the computation are shown in Sec. 3.3.4.

well.

The diagram of coarse-grained model at the slowest time scale (Eq. (3.31)) is illustrated in Fig. 3.7. The initial values are $X = 1$ and $Z = 0$, corresponding to dark adapted samples. If the incident light flux ν is absorbed by PS II, then the ratio $\gamma^f_{U_1}$ to it is used for charge separation, which accompanies the decrease in the population of X state and the increase in the population of $1 - X$ state. As a result, the flux of

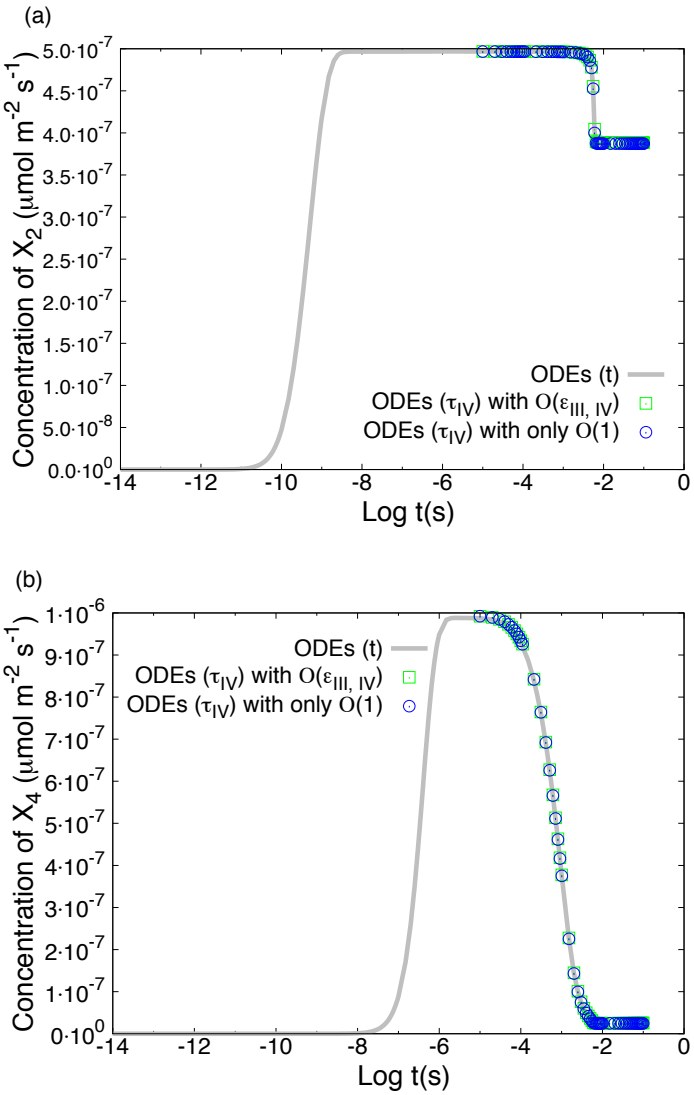

Figure 3.6 Computed dynamics of (a) X_2 and (b) X_4 concentrations. Grey line: the results of full ODEs with t, open square (green): the ODE results with τ_{IV} neglecting $\mathcal{O}(\varepsilon^2_{\mathrm{III,IV}})$ terms (Eq. (A.16)), and open circle (blue): the ODE results with τ_{IV} neglecting $\mathcal{O}(\varepsilon_{\mathrm{III,IV}})$ terms (Eq. (3.30)). The full ODEs are computed up to 0.01 s. Details of the computation are shown in Sec. 3.3.4.

downward outflow from reaction center, whose flux is in proportional to $(1-X)(1-Z)$, increases. On the one hand, $\gamma^f_{U_1} = \kappa'_1 X/(\kappa_d + \kappa'_1 X)$, which is a function of X, decreases along with the decrease in X state; on the other hand, the fraction of heat dissipation, $\gamma^d_{U_1} \equiv 1-\gamma^f_{U_1} = \kappa_d/(\kappa_d+\kappa'_1 X)$, which is also a function of X, increases simultaneously. As a sufficiently long time passes, the system becomes a steady state in which the net flux from reaction center to downward $(= \kappa_4(1-X)(1-Z) - \kappa_{-4}XZ)$

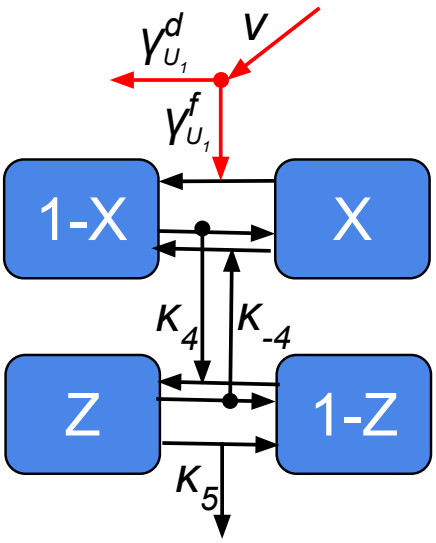

Figure 3.7 Diagram of the coarse-grained model at the τ_{IV} scale. Each box represents each state variable. X: open RC, $1-X$: closed RC, Z: reduced Q_B, and $1-Z$: oxidized Q_B. Black and red lines indicate electron transfer and excitation-energy transfer (or photon flux), respectively.

is equal to the flux of effective charge separation ($= \nu\gamma^f_{U_1}$) under the effect of the process occurring with the outflow from Z to downward.

Here, the effects of application of time-coarse-graining method is summarized as follows: (A) Fast processes are transformed to effectively slow processes. (B) The reaction network system is reduced to a simple one by neglecting reaction paths with evaluated small fluxes. The effect of (A) is reflected in the first term on the right-hand side of ODE for X in Eq. (3.31). This term contains the processes of excitation of PS II by light absorption, transfer of exciton to P_{680} of open RC (X_0 state), transition from X_1 state to X_2 state via charge separation, transition from X_2 state to X_3 state, and transition to closed RC (Y_{01} state). Concretely, ν represents the excitation rate of PS II, and the fractional factor represents the ratio of excited PS II which will transition from X_{01} state to Y_{01} state; κ_d and $\kappa'_1 X = \kappa_1\gamma^f_{X_2} p(X_1+Y_1 \mid U_1)X$, which are involved in the fractional factor, represent the dissipation rate and effective charge separation rate, respectively. Concerning the effective charge separation rate, $p(X_1+Y_1 \mid U_1)X$ and $\kappa_1\gamma^f_{X_2}$ reflect the result of quasi-equilibrium pseudo-steady state approximation at τ_{I} scale and that of nonequilibrium pseudo-steady state approximation at τ_{II} scale, respectively. The result of the approximation at τ_{III} scale is reflected as that almost all

of X_3 state transitioned from X_{01} state via charge separation becomes Y_{01} state. The effect of (B) is reflected on the description of electron transfer between the reaction center and Z_0 or Z_1 state. Eq. (3.31) suggests that one has only to consider X_{01} state and Y_{01} state as electron donor concerning this process. That is, the present time-coarse-graining method succeeds in the simultaneous extraction of the principal reaction paths at each layer of scale and consequently the accurate description of the system dynamics.

Finally, the present work is primarily focused on the novel development of mathematical modeling and methodology that can be applied to multi-scale photosynthetic systems. The applications of the present method to more realistic, full PS II models, which may involve macroscopic phenomena such as long-term state transitions [38], are currently under way, and their details will be reported elsewhere. Photosynthetic systems are complex and systematic combinations of a variety of quantum-mechanical and classical-mechanical devices with a wide range of characteristic times. These features underlie the coarse-graining manipulations developed in the present study, and their theoretical modeling and elucidation remain to be performed with respect to many issues.

3.4 Conclusions

In this chapter, I proposed a reduction method for temporal coarse-graining, and applied it to a simplified PS II model. This coarse-graining method is based on a prototypical three-variable reaction model that has two (fast and slow) time scales and a quadratic, nonlinear reaction process. Influxes into the system belong to the slower time-scale processes, and intra-system reaction processes belong to the faster time-scale ones, which is a typical setting for photosynthetic reaction systems. The extraction of the simple structure at slower time-scale and the reduction of computational cost about the three-variable model were systematically achieved for various cases by applying the temporal coarse-graining reduction method. The different structures of the coarse-grained models appear according to the cases of different time-scaled classification of reaction processes. I then applied the coarse-graining method to a simplified PS II model, which is more complex than the three-variable model and has a multi-time-scale character. The reduction of a model with a multi-time-scale property to that scaled to a certain time scale was performed by applying the coarse-graining method iteratively. It was possible to estimate the orders of magnitudes of

the fluxes of reaction paths reduced by the coarse-graining method. By neglecting the reaction paths whose fluxes are small enough at a given time scale, a reduction of the complex model to a model having a simple structure and small degrees of freedom was carried out. As a result, it has turned out that there exists a simple structure at slower time scale described by two variables and four paths in contrast to the original model composed of nine variables and eighteen paths. The simple structure contains the paths which include the information of fast processes in a renormalized way.

In this study, the proposed method successfully reduced the multi-time-scale dynamics of a photosynthetic reaction system composed of the reactions of the picosecond to millisecond time scale to a slower one. The temporal coarse-graining reduction method proposed in this work thus has the potential to be applied to any reaction model that shares the properties of the prototypical three-variable model for the extraction of the structure of each time-scale layer and the reduction of the computational cost. The reduction of more complex photosynthetic reaction systems with slower ($\gtrsim$ seconds or minutes) time scales using the present method is also possible. Thus, the reduced effective minimum model, which is consistent with the complex and detailed model of photosynthetic reaction systems, is expected to be obtained. Furthermore, the description of mathematical structure at each scale by this novel method will allow for the investigation of the effects of variations of reaction processes, which may be caused by the changes of environmental and genetic factors, on the coarse-grained structure and the asymptotic behavior of the whole system.

Chapter 4

PS II Complex Model Studies for Chl a Fluorescence Induction Kinetics

4.1 Introduction

Photosynthesis is a complex and multi-scale phenomenon in which a variety of chemical processes are involved and intertwined [46]. A variety of environmental responses of this phenomenon at a wide range of scales have been identified via experimental and theoretical studies on different spatiotemporal scales [27]. The measurement of chlorophyll a fluorescence [29, 47] is known in this context as a useful tool to probe the dynamics of photosynthesis. It has then been recognized [23, 28] that the major contribution to chlorophyll a fluorescence arises from photosystem II (PS II) that drives photosynthesis with the charge separation and the production of oxygen. As observed in experiments, the intensity of chlorophyll a fluorescence significantly varies according to environmental conditions. It is noticeable that plants show a variety of time-course patterns of fluorescence under various amplitudes of continuous illumination after the dark acclimation, which are known as fluorescence induction (FI) phenomena [2, 23, 28, 48]. The elucidation of the FI mechanism is, however, difficult generally due to the physicochemical complexities of pertinent systems [3, 15, 28].

Systems approach [49,50] provides an essential viewpoint for analyzing the dynamics of complex biological systems. Concerning the interpretation of FI, a simple kinetic model was first proposed by Duysens and Sweers [51]. They suggested that there was a fluorescence quencher "Q" , later identified as the PS II-bound plastoquinone Q_A in oxidized state. The main idea of Duysens and Sweers theory (DST) is that the fluorescence increases as the amount of quencher decreases, i.e, as the Q_A in

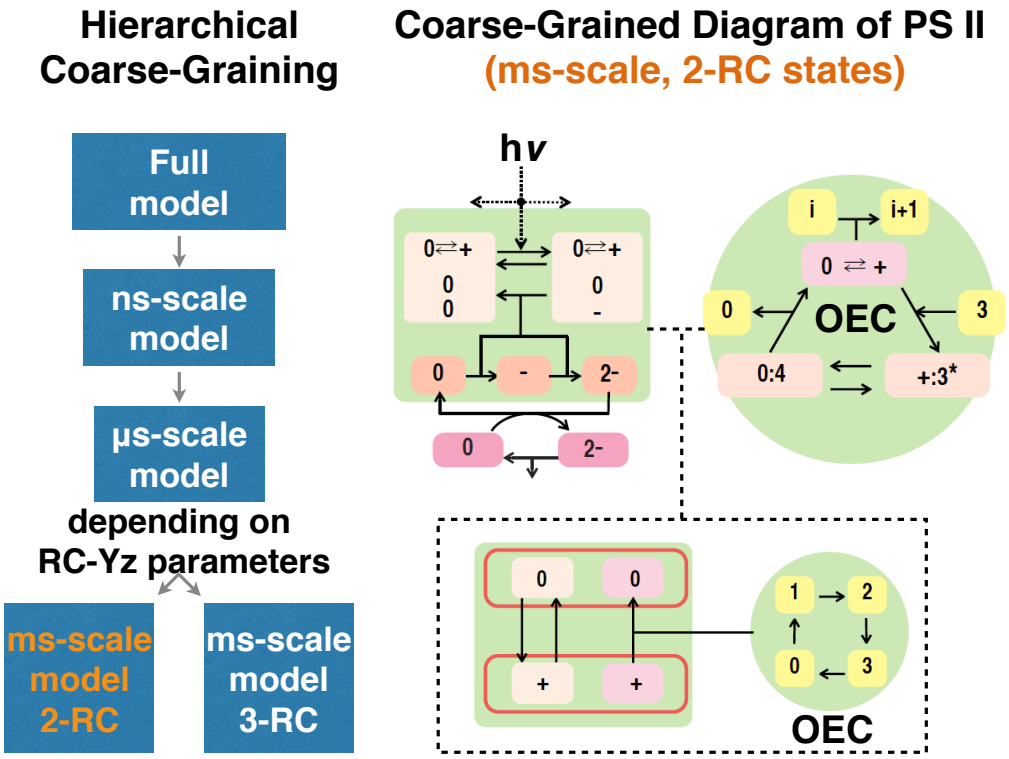

Figure 4.1 Graphical Abstract of Chapter 4

reduced state increases. Besides, they suggested the linear relationship between the fluorescence intensity and the amount of the quencher Q that was considered as the only factor influencing the fluorescence. Following their pioneering work, a number of extensions (extended Duysens-Sweers theories, EDSTs) have been introduced to quantitatively account for the FI kinetics, thus leading to more and more complicated models including many elementary processes associated with excitation-energy and electron transfer reactions [8, 9, 12, 13, 19, 20, 52–62]. EDSTs are formed on the basis of structural information of molecules and thus include the chemical processes such as S-state (Kok) cycle of the oxygen-evolving complex (OEC) [63], reversible radical pair model which describes the trapping and charge-stabilization processes in reaction center (RC) [11, 64, 65], two-electron gate model that describes the electron transfer processes between Q_A and Q_B [66], and so on. EDSTs also presume the quenchers of fluorescence in addition to the Q_A in oxidized state since various quenchers have been proposed. While the accuracy of the model calculations to reproduce the experimental results has thus been improved substantially [31], it has become fairly difficult to

intuitively and comprehensively understand the whole phenomena. On the other hand, a totally different, phenomenological model accounting for the FI behaviors has also been proposed by Vredenberg [67–69]. This theory is based on a three-state trapping model (TSTM) in which the reaction centers make transitions among three representative states with some associated assumptions. Although this model, called fluorescence induction algorithm (FIA), agrees well with experimental results, it is not straightforward to systematically compare it with the EDST, thus preventing us from assessing its relevance [15]. The differences in their degree of complexities also make the comparison more difficult.

In an earlier work [70], we have proposed a hierarchical coarse-graining (HCG) method to comprehensively analyze the dynamical behaviors of reaction networks with many dynamical variables such as those of PS II. In addition to its capability of hierarchically integrating the temporal evolutions of many dynamical variables with wide varieties of characteristic time scales, this HCG method can unambiguously provide us with rational coarse-grained pictures for the whole system dynamics at specified time scales on the basis of underlying mathematical structures. In the present study, we construct a complicated EDST-like model with 28 dynamical variables for PS II including oxygen-evolving complex (OEC) and light-harvesting complex (LHCII) components, and apply the HCG method to the full model for the reduction into a simplified one with good accuracy. We thus intend to understand the FI phenomena intuitively in terms of the correspondence between the original complicated model and the simplified coarse-grained model. Depending on the magnitudes of kinetic parameters in the original detailed models, the HCG method has an ability to give different coarse-grained model descriptions. With this perspective in mind, we simultaneously aim at showing how and under what conditions the phenomenological TSTM by Vredenberg can be derived from the original complex PS II model in this study. Theoretical accounts for the experimental results for the FI behaviors in PS II are thus given comprehensively.

In the following, the EDST-like model and two different coarse-grained models of PS II are described in Materials and Methods section. The HCG method is also introduced concisely in this section. The simulated FIs based on two different models are shown in Results section, where the light-intensity dependent changes of FI pattern from O-J-I-P, which shows two inflection points, J and I, between initial point O and peak point P, to O-J-D-I-P, which shows a dip D between J and I inflection points, observed by Schansker [71,72] are reproduced. The question of what the J-D-I pattern

reflects is answered based on the models, i.e., the transition on the donor side of PS II. In Discussion section, we compare the phases of the RC state over the wide range of light condition between the two different coarse-grained models of PS II and investigate the light-intensity dependent change of dominant transition path of the RC. Conclusion section provides a summary in the present work.

4.2 Materials and Methods

4.2.1 Kinetic model of PS II

To investigate the dynamic properties of the PS II, a variety of EDSTs have been proposed and improved. Though the increase in the complexity of the models makes the reproducibility for the experiments better, it also makes it difficult to interpret the phenomena on the basis of underlying models. While the phenomenological models of PS II which are simpler than EDSTs have been proposed, the comprehensive understanding has not been achieved because there are differences in the reaction processes considered among the models. For example, the quenchers taken into account in the models are different between the EDST by Zhu et al. [19] and the TSTM by Vredenberg [67–69]. Therefore, we here construct a model *à la* EDST which includes both processes described by Zhu et al. and Vredenberg with respect to electron and excitation-energy (exciton) transfers in PS II. The addition of the process for the redox reaction of tyrosine Yz in the model asks for the improvement of the model for the OEC reactions because the redox reaction of Yz facilitates the electron transfer between RC and OEC, and thus affects the reaction of OEC. For the purpose of constructing the comprehensive framework, the following physicochemical processes are also considered in our model:

- Effects of peripheral antenna and core antenna are taken into account.
- Rate constants of charge separation which drives the transition from P^*_{680}Phe to $P^+_{680}Phe^-$ are different between open RC, in which the primary quinone electron acceptor Q_A is neutral, and closed RC, in which Q_A is reduced [71,72].
- As the quenchers of excited chlorophyll, plastoquinone (PQ) [16, 73] and oxidized special-pair (P^+_{680}) [32,74] are taken into account. In some cases, oxidized tyrosine Z (Y^+_Z) [68] is also taken into account.
- As the energy dissipation pathways of excited chlorophyll, non-radiative recombination of $P^+_{680}Q^-_A$ to the ground state, non-radiative recombination of

$P^+_{680}Phe^-$ to the ground state, and intersystem crossing of $P^+_{680}Phe^-$ to the triplet state $^3P^+_{680}Phe^-$ are taken into account [75, 76].

- The states of tyrosine Y_Z which mediates the electron transfer between RC and oxygen-evolving complex (OEC) are explicitly treated in the model.

The kinetic model of PS II is described in terms of the concentrations on a green leaf (in the unit of $\mu\text{mol}\,\text{cm}^{-2}$) of various states of electron donors/acceptors and light-absorbing pigments that change via electron and exciton transfers. This model encompasses the processes from the transition of the states of OEC on the donor side of PS II to the oxidation of PQH_2 by cytochrome b_6f (Cyt b_6f) complex on the acceptor side of PS II. We note that the negative feedbacks by light-induced non-photochemical quenching processes, such as xanthophyll cycle and state transition [29], are assumed to have no effect on the reaction processes of PS II at the concerned timescale range (picoseconds - milliseconds) and therefore not included in the present model. It seems that these processes should be considered in the model to analyze the slow change pattern (seconds - minutes) of FI. The ordinary differential equations (ODEs) for the kinetic model of the reaction processes from RC to plastoquinone pool in thylakoid membrane are then given by

$$
\begin{cases}
\frac{dV_1(t)}{dt} & = \frac{V_0}{W_\mathrm{T}+V_\mathrm{T}+R_\mathrm{T}}V_\mathrm{in} + k_\mathrm{U}W_1\frac{V_0}{V_\mathrm{T}} - k_\mathrm{U}V_1\frac{W_0}{W_\mathrm{T}} \\
 & -(k_\mathrm{F}+k_\mathrm{d}+k_\mathrm{c}\frac{X_2+X_4+Y_2+Y_4}{R_\mathrm{T}}+k_\mathrm{q}\frac{Q_0}{Q_\mathrm{T}})V_1, \\
\frac{dW_1(t)}{dt} & = \frac{W_0}{W_\mathrm{T}+V_\mathrm{T}+R_\mathrm{T}}V_\mathrm{in} - k_\mathrm{U}W_1\frac{V_0}{V_\mathrm{T}} + k_\mathrm{U}V_1\frac{W_0}{W_\mathrm{T}} - \bar{k}_\mathrm{t}\frac{X_0+Y_0}{R_\mathrm{T}}W_1 + \bar{k}_{-\mathrm{t}}\frac{W_0}{W_\mathrm{T}}(X_1+Y_1) \\
 & -(k_\mathrm{F}+k_\mathrm{d}+k_\mathrm{c}\frac{X_2+X_4+Y_2+Y_4}{R_\mathrm{T}}+k_\mathrm{q}\frac{Q_0}{Q_\mathrm{T}})W_1, \\
\frac{dX_0(t)}{dt} & = -\frac{X_0}{W_\mathrm{T}+V_\mathrm{T}+R_\mathrm{T}}V_\mathrm{in} - \bar{k}_\mathrm{t}\frac{X_0}{R_\mathrm{T}}W_1 + \bar{k}_{-\mathrm{t}}\frac{W_0}{W_\mathrm{T}}X_1 \\
 & +(k_\mathrm{F}+k_\mathrm{d}+k_\mathrm{c}\frac{X_2+X_4+Y_2+Y_4}{R_\mathrm{T}}+k_\mathrm{q}\frac{Q_0}{Q_\mathrm{T}})X_1 + k_\mathrm{nr}^\mathrm{d}Y_4 + k_\mathrm{nr}^\mathrm{ind}X_2 + k_0^\mathrm{ntr}X_0^T \\
 & +k_3\frac{T_0}{T_\mathrm{T}}X_4 - k_{-3}\frac{T_1}{T_\mathrm{T}}X_0 + \frac{k_{41}Z_0+k_{42}Z_1}{Z_\mathrm{T}}Y_0 - (k_{-41}Z_1+k_{-42}Z_2)\frac{X_0}{R_\mathrm{T}}, \\
\frac{dX_1(t)}{dt} & = \frac{X_0}{W_\mathrm{T}+V_\mathrm{T}+R_\mathrm{T}}V_\mathrm{in} + \bar{k}_\mathrm{t}\frac{X_0}{R_\mathrm{T}}W_1 - \bar{k}_{-\mathrm{t}}\frac{W_0}{W_\mathrm{T}}X_1 \\
 & -(k_1^\mathrm{o}+k_\mathrm{F}+k_\mathrm{d}+k_\mathrm{c}\frac{X_2+X_4+Y_2+Y_4}{R_\mathrm{T}}+k_\mathrm{q}\frac{Q_0}{Q_\mathrm{T}})X_1 + k_{-1}^\mathrm{o}X_2, \\
\frac{dX_2(t)}{dt} & = k_1^\mathrm{o}X_1 - (k_2+k_{-1}^\mathrm{o}+k_\mathrm{tr}+k_\mathrm{nr}^\mathrm{ind}+k_3\frac{T_0}{T_\mathrm{T}})X_2 + k_{-3}\frac{T_1}{T_\mathrm{T}}X_3 + k_{-2}Y_4 \\
 & +\frac{k_{41}Z_0+k_{42}Z_1}{Z_\mathrm{T}}Y_2 - (k_{-41}Z_1+k_{-42}Z_2)\frac{X_2}{R_\mathrm{T}}, \\
\frac{dX_3(t)}{dt} & = k_3\frac{T_0}{T_\mathrm{T}}X_2 - (k_2+k_{-3}\frac{T_1}{T_\mathrm{T}})X_3 + k_{-2}Y_0 \\
 & +\frac{k_{41}Z_0+k_{42}Z_1}{Z_\mathrm{T}}Y_3 - (k_{-41}Z_1+k_{-42}Z_2)\frac{X_3}{R_\mathrm{T}}, \\
\frac{dX_4(t)}{dt} & = -k_3\frac{T_0}{T_\mathrm{T}}X_4 + k_{-3}\frac{T_1}{T_\mathrm{T}}X_0 + \frac{k_{41}Z_0+k_{42}Z_1}{Z_\mathrm{T}}Y_4 - (k_{-41}Z_1+k_{-42}Z_2)\frac{X_4}{R_\mathrm{T}}, \\
\frac{dX_2^\mathrm{tr}(t)}{dt} & = k_\mathrm{tr}X_2 - k_{02}^\mathrm{tr}X_2^\mathrm{tr}, \\
\frac{dX_0^\mathrm{tr}(t)}{dt} & = k_{02}^\mathrm{tr}X_2^\mathrm{tr} - k_0^\mathrm{ntr}X_0^\mathrm{tr}, \\
\frac{dY_0(t)}{dt} & = -\frac{Y_0}{W_\mathrm{T}+V_\mathrm{T}+R_\mathrm{T}}V_\mathrm{in} - \bar{k}_\mathrm{t}\frac{Y_0}{R_\mathrm{T}}W_1 + \bar{k}_{-\mathrm{t}}\frac{W_0}{W_\mathrm{T}}Y_1 \\
 & +(k_\mathrm{F}+k_\mathrm{d}+k_\mathrm{c}\frac{X_2+X_4+Y_2+Y_4}{R_\mathrm{T}}+k_\mathrm{q}\frac{Q_0}{Q_\mathrm{T}})Y_1 + k_2X_3 + k_0^\mathrm{ntr}Y_0^\mathrm{tr} + k_\mathrm{nr}^\mathrm{ind}Y_2 \\
 & +k_3\frac{T_0}{T_\mathrm{T}}Y_4 - (k_{-2}+k_{-3}\frac{T_1}{T_\mathrm{T}}+\frac{k_{41}Z_0+k_{42}Z_1}{Z_\mathrm{T}})Y_0 + (k_{-41}Z_1+k_{-41}Z_2)\frac{X_0}{R_\mathrm{T}}, \\
\frac{dY_1(t)}{dt} & = \frac{Y_0}{W_\mathrm{T}+V_\mathrm{T}+R_\mathrm{T}}V_\mathrm{in} + \bar{k}_\mathrm{t}\frac{Y_0}{R_\mathrm{T}}W_1 - \bar{k}_{-\mathrm{t}}\frac{W_0}{W_\mathrm{T}}Y_1 \\
 & -(k_1^\mathrm{c}+k_\mathrm{F}+k_\mathrm{d}+k_\mathrm{c}\frac{X_2+X_4+Y_2+Y_4}{R_\mathrm{T}}+k_\mathrm{q}\frac{Q_0}{Q_\mathrm{T}})Y_1 + k_{-1}^\mathrm{c}Y_2, \\
\frac{dY_2(t)}{dt} & = k_1^\mathrm{c}Y_1 - (k_{-1}^\mathrm{c}+k_\mathrm{tr}+k_\mathrm{nr}^\mathrm{ind}+k_3\frac{T_0}{T_\mathrm{T}}+k_{-3}\frac{T_1}{T_\mathrm{T}}Y_3+\frac{k_{41}Z_0+k_{42}Z_1}{Z_\mathrm{T}})Y_2 \\
 & +(k_{-41}Z_1+k_{-42}Z_2)\frac{X_2}{R_\mathrm{T}}, \\
\frac{dY_3(t)}{dt} & = k_3\frac{T_0}{T_\mathrm{T}}Y_2 - (k_{-3}\frac{T_1}{T_\mathrm{T}}+\frac{k_{41}Z_0+k_{42}Z_1}{Z_\mathrm{T}})Y_3 + (k_{-41}Z_1+k_{-42}Z_2)\frac{X_3}{R_\mathrm{T}}, \\
\frac{dY_4(t)}{dt} & = k_2X_2 - (k_3\frac{T_0}{T_\mathrm{T}}+\frac{k_{41}Z_0+k_{42}Z_1}{Z_\mathrm{T}}+k_{-2}+k_\mathrm{nr}^\mathrm{d})Y_4 + k_{-3}\frac{T_1}{T_\mathrm{T}}Y_0 \\
 & +(k_{-41}Z_1+k_{-42}Z_2)\frac{X_4}{R_\mathrm{T}}, \\
\frac{dY_2^\mathrm{tr}(t)}{dt} & = k_\mathrm{tr}Y_2 - k_{02}^\mathrm{tr}Y_2^\mathrm{tr}, \\
\frac{dY_0^\mathrm{tr}(t)}{dt} & = k_{02}^\mathrm{tr}Y_2^\mathrm{tr} - k_0^\mathrm{ntr}Y_0^\mathrm{tr}, \\
\frac{dZ_1(t)}{dt} & = k_{41}\frac{Z_0}{Z_\mathrm{T}}(Y_0+Y_2+Y_3+Y_4) - k_{-41}\frac{X_0+X_2+X_3+X_4}{R_\mathrm{T}}Z_1 \\
 & -k_{42}\frac{Z_1}{Z_\mathrm{T}}(Y_0+Y_2+Y_3+Y_4) + k_{-42}\frac{X_0+X_2+X_3+X_4}{R_\mathrm{T}}Z_2, \\
\frac{dZ_2(t)}{dt} & = k_{42}\frac{Z_1}{Z_\mathrm{T}}(Y_0+Y_2+Y_3+Y_4) - k_{-42}\frac{X_0+X_2+X_3+X_4}{R_\mathrm{T}}Z_2 \\
 & -k_5Z_2\frac{Q_0}{Q_\mathrm{T}} + k_{-5}Z_0\frac{Q_1}{Q_\mathrm{T}}, \\
\frac{dQ_1(t)}{dt} & = k_5Z_2\frac{Q_0}{Q_\mathrm{T}} - k_{-5}Z_0\frac{Q_1}{Q_\mathrm{T}} - k_6Q_1,
\end{cases}
\tag{4.1a}
$$

$$\begin{cases} V_0(t) &= V_\mathrm{T} - V_1, \\ W_0(t) &= W_\mathrm{T} - W_1, \\ Z_0(t) &= Z_\mathrm{T} - Z_1 - Z_2, \\ Q_0(t) &= Q_\mathrm{T} - Q_1, \end{cases} \tag{4.1b}$$

where V, W, X, Y, Z and Q represent the concentrations of different states of the peripheral antenna, core antenna, $\mathrm{Q_A}$-neutral (open) RC, $\mathrm{Q_A}$-reduced (closed) RC, secondary quinone electron acceptor ($\mathrm{Q_B}$) and plastoquinone pool ($\mathrm{PQ}, \mathrm{PQH_2}$), respectively, as follows. V_0: ground states of peripheral antenna; W_0: ground states of core antenna; V_1: excited states of peripheral antenna; W_1: excited states of core antenna; X_0: $[\mathrm{P_{680}PheQ_A}]$; X_1: $[\mathrm{P^*_{680}PheQ_A}]$; X_2: $[\mathrm{P^+_{680}Phe^-Q_A}]$; X_3: $[\mathrm{P_{680}Phe^-Q_A}]$; X_4: $[\mathrm{P^+_{680}PheQ_A}]$; Y_0: $[\mathrm{P_{680}PheQ^-_A}]$; Y_1: $[\mathrm{P^*_{680}PheQ^-_A}]$; Y_2: $[\mathrm{P^+_{680}Phe^-Q^-_A}]$; Y_3: $[\mathrm{P_{680}Phe^-Q^-_A}]$; Y_4: $[\mathrm{P^+_{680}PheQ^-_A}]$; Z_0: $[\mathrm{Q_B}]$; Z_1: $[\mathrm{Q^-_B}]$; Z_2: $[\mathrm{Q^{2-}_B}]$; Q_0: $[\mathrm{PQ}]$; Q_1: $[\mathrm{PQH_2}]$, where [ ] means the concentration. The superscript "tr" indicates the triplet state. The right-hand sides of ODEs represent the rates of electron and exciton transfers. For example, the X_1 state changes in time with the rates of light absorption, exciton transfer and electron transfer. The rate of excitation of open RC by light absorption is given as the product of the flux V_in of incident light for PS II and the ratio $X_0/(W_\mathrm{T} + V_\mathrm{T} + R_\mathrm{T})$ of the open RC in the ground state to all the light absorbing pigments. With regard to the exciton transfer, the open RC is connected with the core antenna. The trapping rate from core antenna to open RC is proportional to the concentration W_1 of the excited core antenna, and the ratio X_0/R_T of open RC in the ground state to all of RC. The detrapping rate for the exciton from open RC to core antenna is proportional to the concentration of the excited open RC, X_1, and the ratio of core antenna in the ground state, W_0/W_T. In addition, the X_1 state changes to the ground state (X_0) via charge separation, fluorescence emission, dissipation, $\mathrm{P^+_{680}}$ quenching and PQ quenching, where the quenching rates of $\mathrm{P^+_{680}}$ and PQ are proportional to the populations of quenchers, $X_2 + X_4 + Y_2 + Y_4$ and Q_0, respectively. Further, the charge recombination of the X_2 state produces the X_1 state with the rate proportional to the population of X_2. All other states of electron donors/acceptors and light absorbing pigments change in similar ways to X_1.

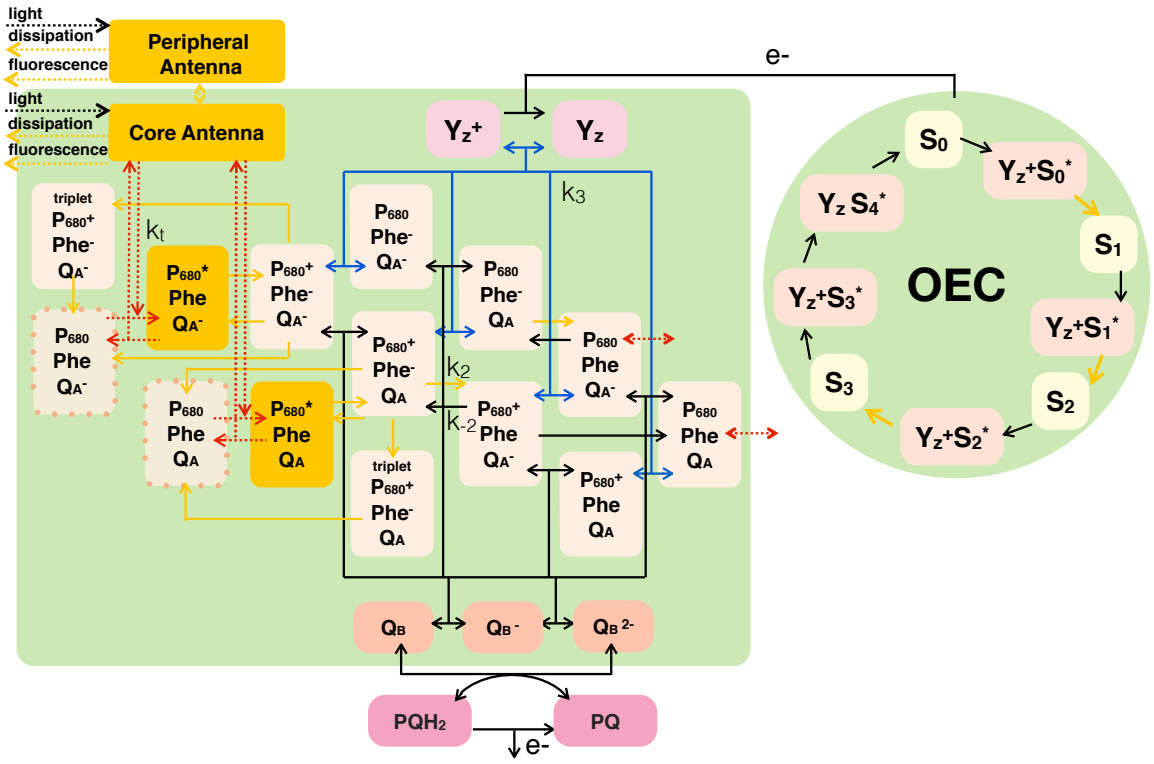

Figure 4.2 Schematic diagram of excitation-energy and electron transfer processes for PS II.
The EDST-like model is described by eqs 4.1a, 4.1b and 4.2. Solid and dashed lines indicate the electron transfer and the excitation-energy transfer, respectively. Each color indicates different time-scales as follows. Red: picoseconds, yellow: nanoseconds, blue: microseconds, black: milliseconds.

The reaction diagram of PS II and the associated parameters of the model are shown in Fig. 4.2 and Table 4.1, respectively. Each box in Fig. 4.2 represents each different state of electron donors/acceptors. Besides, each arrow represents the transport of excitation energy or electron. Electrons are supplied from OEC to PS II. These electrons reduce the oxidized tyrosine and P_{680}^{+} in turn. Meanwhile, light is absorbed by peripheral antenna and core antenna, and then excitation energy (exciton) is generated. The excitation energy is transported to RC from core antenna. Here, it is assumed that the exciton is received only by the RC in which both P_{680} and Phe are in ground states. Once the RC receives the excitation energy, charge separation occurs, and then Phe and Q_A are reduced in turn. Quinone B receives an electron

from Q_A twice and then forms the doubly reduced state. The doubly reduced Q_B forms plastoquinol. Plastoquinol diffuses in thylakoid membrane and then is oxidized by the Cyt b_6f complex.

Concerning Eq. (4.1a), we note that $\bar{k_t}$ and $\bar{k}_{-t}$ are connected to microscopic information in terms of the perturbed-two-level model [44] as below: $\bar{k_t} = zk_t/(N_c - 1)$ and $\bar{k}_{-t} = zk_{-t}$, where z is a coordination number (the number of pigments next to RC) and N_c is the number of pigments at one core antenna; k_t and k_{-t} are the rate constants of trapping and de-trapping, respectively, of the excitation-energy transfer between the RC and its nearest pigments at antenna. In regard to the diffusion of excitation energy, the trap-limited condition is assumed in this model.

The ODEs for the oxygen-evolving complex (OEC) that exists on the donor side of PS II are given by

$$\begin{cases} \dfrac{dT_1(t)}{dt} & = -\displaystyle\sum_{i=0}^{3} k_{i*,i}\frac{S_i}{S_T}T_1 + k_3\frac{T_0}{T_T}(X_2 + X_4 + Y_2 + Y_4) \\ & \quad -k_{-3}\dfrac{T_1}{T_T}(X_0 + X_4 + Y_0 + Y_4), \\ \dfrac{dS_0(t)}{dt} & = k_{0,4}TS_4 - k_{0*,0}\dfrac{S_0}{S_T}T_1, \\ \dfrac{dS_i(t)}{dt} & = k_{i,(i-1)*}TS^*_{i-1} - k_{i*,i}\dfrac{S_i}{S_T}T_1 \qquad (i = 1-3), \\ \dfrac{dTS^*_i(t)}{dt} & = k_{i*,i}\dfrac{S_i}{S_T}T_1 - k_{i+1,i*}TS^*_i \qquad (i = 0-2), \\ \dfrac{dTS^*_3(t)}{dt} & = k_{3*,3}\dfrac{S_3}{S_T}T_1 - k_{4,3*}TS^*_3 + k_{3*,4}TS_4, \\ \dfrac{dTS_4(t)}{dt} & = k_{4,3*}TS^*_3 - (k_{3*,4} + k_{0,4})TS_4, \end{cases} \tag{4.2}$$

where the conservation relations hold as below: $T_T = T_0 + T_1 + \sum TS^*_i + TS_4$, $S_T = \sum S_i + \sum TS^*_i + TS_4$. The concentrations of the states of tyrosine Z (Y_Z^+) of the D1 protein are represented by T's, T_0: $[Y_Z]$ and T_1: $[Y_Z^+]$, where [ ] means the concentration. The OEC is described on the basis of the model proposed by [63] ("Kok cycle") that accounts for the oxidative water splitting by four sequential steps. The concentrations of the five states of OEC are denoted as $S_i\,(i = 0-4)$, where S_0 and S_4 indicate the concentrations of the states with the redox levels of H_2O and O_2, respectively, and S_1, S_2 and S_3 indicate the concentrations of the states with the redox levels of hydroxyl radical, peroxide and superoxide, respectively. Besides, the triggering processes of S_i states by Y_Z^+ are included, and the "triggered" redox states of S_i's are denoted by S^*_i's. The "triggered" redox states of OEC and S_4 state are

treated as being coupled with Y_Z^+ and thus described as TS_i^*'s and TS_4, respectively. With respect to S_3 modeling, "S_4 dogma" [77,78] is employed in this model (Fig. 4.2).

The parameters that belong to significantly different timescales coexist in the PS II model. To clearly represent the multi-timescale property, we characterize each timescale by means of the representative rate constant. As the hierarchical structure in the time scales of this system proves to be decomposed into four classes, we introduce the dimensionless times τ_{I}, τ_{II}, τ_{III} and τ_{IV} normalized by the characteristic rate constants as

$$\begin{aligned} \tau_{\mathrm{I}} &\equiv \bar{k_{\mathrm{t}}} t, \\ \tau_{\mathrm{II}} &\equiv k_2 t, \\ \tau_{\mathrm{III}} &\equiv k_3 t, \\ \tau_{\mathrm{IV}} &\equiv k_{-2} t. \end{aligned} \tag{4.3}$$

Here, the characteristic parameters satisfy the relation: $\bar{k_{\mathrm{t}}} \gg k_2 \gg k_3 \gg k_{-2}$. The rate constants k_{t}, k_2, k_3 and k_{-2} have the picosecond, nanosecond, microsecond and millisecond orders of magnitude, respectively. Therefore, each unit of each dimensionless time τ_{I}, τ_{II}, τ_{III} and τ_{IV} is characterized by the timescale of picosecond, nanosecond, microsecond and millisecond, respectively. The ratios of the time scales are then introduced as $\varepsilon_{\mathrm{I,II}} \equiv k_2/\bar{k_{\mathrm{t}}}, \varepsilon_{\mathrm{II,III}} \equiv k_3/k_2, \varepsilon_{\mathrm{III,IV}} \equiv k_{-2}/k_3$ and $\varepsilon_{\mathrm{II,IV}} \equiv \varepsilon_{\mathrm{II,III}}\varepsilon_{\mathrm{III,IV}} = k_{-2}/k_2$, satisfying the following relations: $\varepsilon_{\mathrm{II,IV}} \ll \varepsilon_{\mathrm{I,II}} \sim \varepsilon_{\mathrm{II,III}} \sim \varepsilon_{\mathrm{III,IV}} \ll 1$.

The rate constants are classified on the basis of their time scales as $A_{\mathrm{I}} = \{k_j \mid \mathcal{O}(k_j) \sim \mathcal{O}(\bar{k_{\mathrm{t}}})\}, A_{\mathrm{II}} = \{k_j \mid \mathcal{O}(k_j) \sim \mathcal{O}(k_2)\}, A_{\mathrm{III}} = \{k_j \mid \mathcal{O}(k_j) \sim \mathcal{O}(k_3)\}$ and $A_{\mathrm{IV}} = \{k_j \mid \mathcal{O}(k_j) \sim \mathcal{O}(k_{-2})\}$. We introduce dimensionless rate constants κ_j defined as each k_j scaled by the characteristic rate constants of time-scale groups to which each k_j belongs:

$$\kappa_j = \begin{cases} k_j/\bar{k_{\mathrm{t}}} & k_j \in A_{\mathrm{I}}, \\ k_j/k_2 & k_j \in A_{\mathrm{II}}, \\ k_j/k_3 & k_j \in A_{\mathrm{III}}, \\ k_j/k_{-2} & k_j \in A_{\mathrm{IV}}, \end{cases} \tag{4.4}$$

thus each κ_j being of the order of unity. The light excitation rate v, which is defined by the ratio (radiation flux density V_{in})/(concentration of PS II R_{T}), is also normalized as $\nu = v/k_j$. The timescale classes to which each rate constant belongs are shown in Table 1. Parameters used in this model were obtained in experiments [11, 65, 79–90]

except for radiation flux density V_{in} for PS II, which is an environmental factor. The present study is concerned with the changes of FI pattern depending on this V_{in} value.

4.2.2 Coarse graining

In general, the complexity and the multi-timescale property of a system cause difficulties in understanding the object intuitively and calculating the slow dynamics. Photosynthesis reaction system is one of the systems which have the characteristics addressed above. If one intends to understand the dynamical properties of photosynthesis reaction system reflected by FI, the whole reactions inside chloroplast from excitation energy transfer (picosecond scale) to membrane protein diffusion (minute scale) over the wide timescale range should be taken into account. The picture of this whole reaction system is too complex to understand intuitively. Besides, the wide-range timescale property makes it difficult to simulate the dynamics at slow scales on the basis of a kinetic reaction model because the computational cost becomes too high to integrate over time. The coarse-graining treatment, which extracts the mathematical structure of concerned dynamical system and reduces the degrees of freedom, is an approach to deal with such difficulties as above [91–93]. In the following, the hierarchical time-coarse-graining of a reaction network of PS II that has a multi-timescale property as described above is attempted by repeatedly applying the HCG method proposed by Matsuoka et al. [70]. This temporal coarse-graining scheme consists of three steps. At step 0, the original ODEs with respect to time t are converted to the ODEs with dimensionless time in which the fastest scale reactions have $\mathcal{O}(1)$ rates. Then at step 1, the coarse-graining functions Γ's, which give the values of some fast variables in terms of slow variables, are derived by means of the steady-state approximation. If possible, quasi-conserved quantities which vary with $\mathcal{O}(\varepsilon)$ rates at concerned time scales are introduced. At step 2, the transformation of the dimensionless-time ODEs to those with slower time scale is conducted through the results of step 1. The coarse-graining of PS II with four classes of time scales is performed by applying this scheme three times repeatedly. As a result, the hierarchical ODEs are obtained with $\tau_{\mathrm{I}}, \tau_{\mathrm{II}}, \tau_{\mathrm{III}}$ and τ_{IV}, respectively. It is noted that the accuracies of the coarse-grained ODEs can be controlled by means of the timescale ratios $\varepsilon_{\mathrm{I,II}}, \varepsilon_{\mathrm{II,III}}, \varepsilon_{\mathrm{III,IV}}$ and $\varepsilon_{\mathrm{II,IV}}$ introduced in this method. The accuracies of the hierarchical ODEs were also evaluated numerically in our previous study [70]. Besides, with respect to the stability of the concerned system, a prototypical three-state model

Table 4.1 Parameter List of PS II Model

Description	Notation	Value (Time-scale class)	Reference
Rate constant of excitation transfer from core antenna to special pair	k_{t}	(A_{I})	Implicit
Rate constant of excitation transfer from special pair to core antenna	$k_{-\mathrm{t}}$	$k_{\mathrm{t}} \exp[\frac{hc(1/\lambda_{\mathrm{Chl}}-1/\lambda_{\mathrm{p}})}{k_{\mathrm{B}}T}]^{*}(A_{\mathrm{I}})$	Implicit
Rate constant of excitation transfer between core and peripheral antenna	k_{U}	$10^{10}\,\mathrm{s}^{-1}$ (A_{II})	[90]
Rate constant of excitation dissipation from antenna	k_{d}	$10^{8}\,\mathrm{s}^{-1}$ (A_{II})	[48, 65]
Rate constant of excitation fluorescence from antenna	k_{F}	$3\times10^{7}\,\mathrm{s}^{-1}$ (A_{II})	[11]
Rate constant of charge separation in open ($\mathrm{Q_A}$ is neutral) reaction center	k_{1}^{o}	$2.5\times10^{10}\,\mathrm{s}^{-1}$ (A_{II})	[88]
Rate constant of charge recombination in open reaction center	k_{-1}^{o}	$3\times10^{8}\,\mathrm{s}^{-1}$ (A_{II})	[88]
Rate constant of charge separation in closed ($\mathrm{Q_A}$ is reduced) reaction center	k_{1}^{c}	$4\times10^{9}\,\mathrm{s}^{-1}$ (A_{II})	[88]
Rate constant of charge recombination in closed reaction center	k_{-1}^{c}	$9\times10^{8}\,\mathrm{s}^{-1}$ (A_{II})	[88]
Rate constant of electron transfer from Phe^{-} to $\mathrm{Q_A}$	k_{2}	$2\times10^{9}\,\mathrm{s}^{-1}$ (A_{II})	[88]
Rate constant of electron transfer from $\mathrm{Q_A^{-}}$ to Phe^{-}	k_{-2}	$2,000\,\mathrm{s}^{-1}$ (A_{IV})	Model estimate [48]
Rate constant of $\mathrm{P680}^{+}$ quenching of antenna	k_{c}	$10^{9}\,\mathrm{s}^{-1}$ (A_{II})	[65]
Rate constant of PQ quenching	k_{q}	$3\times10^{6}\,\mathrm{s}^{-1}$ (A_{II})	[57]
Rate constant of non-radiative recombination from $\mathrm{P_{680}^{+}Phe^{-}}$	$k_{\mathrm{nr}}^{\mathrm{ind}}$	$10^{8}\,\mathrm{s}^{-1}$ (A_{II})	[75, 76]
Rate constant of non-radiative recombination from $\mathrm{P_{680}^{+}Q_A^{-}}$	$k_{\mathrm{nr}}^{\mathrm{d}}$	$500\,\mathrm{s}^{-1}$ (A_{IV})	[76]
Rate constant of intersystem crossing to the triplet state from $\mathrm{P_{680}^{+}Phe^{-}}$	k_{tr}	$10^{8}\,\mathrm{s}^{-1}$ (A_{II})	[76]
Rate constant of non-radiative recombination from $\mathrm{{}^{3}P_{680}^{+}Phe^{-}}$	k_{02}^{tr}	$3.3\times10^{9}\,\mathrm{s}^{-1}$ (A_{II})	[76]
Rate constant of decay into the ground state from $\mathrm{{}^{3}P_{680}Phe}$	k_{0}^{ntr}	$1.5\times10^{9}\,\mathrm{s}^{-1}$ (A_{II})	[75]
Rate constant of electron transfer from $\mathrm{Y_Z}$ to $\mathrm{P_{680}^{+}}$	k_{3}	$5\times10^{6}-10^{7}\,\mathrm{s}^{-1}$ (A_{III})	[78, 85]
Rate constant of electron transfer from $\mathrm{P_{680}}$ to $\mathrm{Y_Z^{+}}$	k_{-3}	$10^{6}\,\mathrm{s}^{-1}$ (A_{III})	[57, 78]

(To be continued)

* k_{B}: Boltzmann constant, h: Planck constant, c: speed of light, T: temperature (298K), λ_{Chl}: wavelength for the maximum absorbance by antenna chlorophyll (678nm), λ_{p}: wavelength for the maximum absorbance by special pair (680nm).

(Continued)

Rate constant of OEC from S_i "triggered" redox state: $Y_Z^+ S_i^*$ to S_{i+1} state (i=0-2)	$k_{i+1,i}$	$10^9\,s^{-1}(A_{II})$	[78]
Rate constant of OEC from S_3 "triggered" redox state: $Y_Z^+ S_3^*$ to S_4 state	$k_{4,3}$	$1,000\,s^{-1}$ (A_{IV})	[78]
Rate constant of OEC from S_0 state to S_0 "triggered" redox state: $Y_Z^+ S_0^*$	$k_{0*,0}$	$1.4 \times 10^4\,s^{-1}$ (A_{IV})	[78]
Rate constant of OEC from S_1 state to S_1 "triggered" redox state: $Y_Z^+ S_1^*$	$k_{1*,1}$	$7,000\,s^{-1}$ (A_{IV})	[78]
Rate constant of OEC from S_2 state to S_2 "triggered" redox state: $Y_Z^+ S_2^*$	$k_{2*,2}$	$3,300\,s^{-1}$ (A_{IV})	[78]
Rate constant of OEC from S_3 state to S_3 "triggered" redox state: $Y_Z^+ S_3^*$	$k_{3*,3}$	$5,000\,s^{-1}$ (A_{IV})	[78]
Rate constant of OEC from S_4 state to $Y_Z^+ S_3^*$	$k_{3*,4}$	$1 \times 10^4\,s^{-1}$ (A_{IV})	[78]
Radiation flux density to PS II	V_{in}	$(A_{III}) \cup (A_{IV})$	
Rate constant of electron transfer from $Q_A^-$to Q_B	k_{41}	$2,500\,s^{-1}$ (A_{IV})	[82–84, 89]
Rate constant of electron transfer from Q_A^- to Q_B^-	k_{42}	$3,300\,s^{-1}$ (A_{IV})	[82–84, 89]
Rate constant of electron transfer from $Q_B^-$to Q_A	k_{-41}	$175\,s^{-1}$ (A_{IV})	[82]
Rate constant of electron transfer from Q_B^{2-} to Q_A	k_{-42}	$250\,s^{-1}$ (A_{IV})	[80]
Rate constant of electron transfer from Q_B^{2-} to PQ	k_5	$800\,s^{-1}$ (A_{IV})	[87, 89]
Rate constant of electron transfer from PQH_2 to Q_B^{2-}	k_{-5}	$80\,s^{-1}$ (A_{IV})	[81]
Rate constant of electron transfer from PQH_2 to Cyt b_6f protein complex	k_6	$50\,s^{-1}$ (A_{IV})	[79]
Concentration of all reaction center's states (conserved quantity)	R_T	-	-
Concentration of all Q_B site (conserved quantity)	Z_T	-	-
Concentration of PQ pool in thylakoid membrane (conserved quantity)	Q_T	-	-
Concentration of all OEC states (conserved quantity)	S_T	-	-
Concentration of all Y_Z states (conserved quantity)	T_T	-	-
Concentration of total pigments in peripheral antenna (conserved quantity)	V_T	-	-
Concentration of total pigments in core antenna (conserved quantity)	W_T	-	-
Number of pigments at one peripheral antenna	N_P	200	[86]
Number of pigments at one core antenna	N_C	40	[75]
Ratio of amount of plastoquinon to PS II in thylakoid membrane	N_Q	8	Model estimate [19]

which possesses the characteristics of photosynthesis reaction system was also analyzed. Though the system treated in the present study has higher degrees of freedom than those of the earlier three-state model, the essential feature about the stability of EDST-like model would be the same as that of three-state model because these models have the dynamical characteristics of photosynthetic reaction system in common. Hereafter, the case $v \in A_{\mathrm{IV}}$ is treated. This illumination condition is almost certainly satisfied on the surface of the Earth.

From picosecond scale to nanosecond scale

To transform the original ODEs with t to the dimensionless-time ODEs with τ_{I}, the step 0 of coarse-graining scheme is applied, i.e., Eq. (4.1a) is divided by $\bar{k_{\mathrm{t}}}$. The variables changing with $\mathcal{O}(1)$ rates at the τ_{I} scale are W_1, W_0, X_1, X_0, Y_1 and Y_0 (see Appendix B.1.1).

In step 1, quasi-conserved quantities at τ_{I} scale are introduced [70] as follows:

$$\begin{aligned} U_1 &\equiv W_1 + X_1 + Y_1, \\ X_{01} &\equiv X_0 + X_1, \\ Y_{01} &\equiv Y_0 + Y_1. \end{aligned} \tag{4.5}$$

Provided that the processes at τ_{I} scale are in pseudo-steady states for $\tau_{\mathrm{I}} \to \infty$, the asymptotic behaviors of W_1, X_1, Y_1 as $\tau_{\mathrm{I}} \to \infty$ can be described in terms of slow variables U_1, X_{01}, Y_{01} as $\lim_{\tau_{\mathrm{I}}\to\infty} W_1(\tau_{\mathrm{I}}) = p(W_1 \mid U_1)U_1, \lim_{\tau_{\mathrm{I}}\to\infty} X_1(\tau_{\mathrm{I}}) = p(X_1 \mid U_1)U_1$ and $\lim_{\tau_{\mathrm{I}}\to\infty} Y_1(\tau_{\mathrm{I}}) = p(Y_1 \mid U_1)U_1$, where $p(W_1 \mid U_1) = \bar{\kappa}_{-\mathrm{t}}R_{\mathrm{T}}/(X_{01} + Y_{01} + \bar{\kappa}_{-\mathrm{t}}R_{\mathrm{T}})$, $p(X_1 \mid U_1) = X_{01}/(X_{01} + Y_{01} + \bar{\kappa}_{-\mathrm{t}}R_{\mathrm{T}})$ and $p(Y_1 \mid U_1) = Y_{01}/(X_{01} + Y_{01} + \bar{\kappa}_{-\mathrm{t}}R_{\mathrm{T}})$ are the fraction (probability) functions which represent the partition ratios of U_1 (population of the total exciton over the core antenna and the RC) at the core antenna, the open RC, and the closed RC, respectively [70]. We note that we refer to U_1 as excited population in the "core antenna" in the following (meaning the RC included). By substituting these relations into the original ODEs and expressing them in terms of the quasi-conserved quantities, the ODEs with $\tau_{\mathrm{I}} \to \infty$ are obtained.

As the treatment of step 2, the transformation from the ODEs with $\tau_{\mathrm{I}} \to \infty$ to those with τ_{II} is achieved by dividing the ODEs by $\varepsilon_{\mathrm{I,II}}$.

From nanosecond scale to microsecond scale

The variables that change with $\mathcal{O}(1)$ rates in the ODEs with τ_{II} are V_1, U_1, X_2, Y_2, X_3, $X_2^{\mathrm{tr}}, X_0^{\mathrm{tr}}, Y_2^{\mathrm{tr}}$ and Y_0^{tr}. In step 1, the variables that exponentially decay with $\mathcal{O}(1)$

rates at the τ_{II} scale are assumed to be in nonequilibrium pseudo-steady states for $\tau_{\text{II}} \to \infty$, i.e., the total influx and total outflux in each state are in balance. In this case, there is no quasi-conserved quantity at the τ_{II} scale and the detailed balance is not achieved at each state for $\tau_{\text{II}} \to \infty$. As a result, coarse-graining functions for $\tau_{\text{II}} \to \infty$ that represent $V_1, U_1, X_2, Y_2, X_3, X_2^{\text{tr}}, X_0^{\text{tr}}, Y_2^{\text{tr}}, Y_0^{\text{tr}}$ in terms of the slower variables are obtained as $\lim_{\tau_{\text{II}}\to\infty} U_1(\tau_{\text{II}}) \equiv \varepsilon_{\text{II,IV}}\Gamma_{U_1}$, $\lim_{\tau_{\text{II}}\to\infty} V_1(\tau_{\text{II}}) \equiv \varepsilon_{\text{II,IV}}\Gamma_{V_1}$, $\lim_{\tau_{\text{II}}\to\infty} X_2(\tau_{\text{II}}) \equiv \varepsilon_{\text{II,IV}}\Gamma_{X_2}$, $\lim_{\tau_{\text{II}}\to\infty} Y_2(\tau_{\text{II}}) \equiv \varepsilon_{\text{II,IV}}\Gamma_{Y_2}$, $\lim_{\tau_{\text{II}}\to\infty} X_3(\tau_{\text{II}}) \equiv \varepsilon_{\text{II,IV}}\Gamma_{X_3}$, $\lim_{\tau_{\text{II}}\to\infty} X_2^{\text{tr}}(\tau_{\text{II}}) \equiv \varepsilon_{\text{II,IV}}\Gamma_{X_2^{\text{tr}}}$, $\lim_{\tau_{\text{II}}\to\infty} X_0^{\text{tr}}(\tau_{\text{II}}) \equiv \varepsilon_{\text{II,IV}}\Gamma_{X_0^{\text{tr}}}$, $\lim_{\tau_{\text{II}}\to\infty} Y_2^{\text{tr}}(\tau_{\text{II}}) \equiv \varepsilon_{\text{II,IV}}\Gamma_{Y_2^{\text{tr}}}$, $\lim_{\tau_{\text{II}}\to\infty} Y_0^{\text{tr}}(\tau_{\text{II}}) \equiv \varepsilon_{\text{II,IV}}\Gamma_{Y_0^{\text{tr}}}$. The explicit forms of coarse-graining functions are presented in Appendix B.1.2.

In regard to the model of OEC, its ODEs with τ_{II} are obtained by dividing Eq. (4.2) by k_2. Provided that the variables that exponentially decay with $\mathcal{O}(1)$ rates at the τ_{II} scale are in nonequilibrium pseudo-steady states for $\tau_{\text{II}} \to \infty$ as the treatment of step 1, the coarse-graining functions, $\lim_{\tau_{\text{II}}\to\infty} TS_i^*(\tau_{\text{II}}) \equiv \varepsilon_{\text{II,IV}}\Gamma_{TS_i^*}$ for $i = 0-2$, are obtained (see Appendix B.1.2).

By substituting these coarse-graining functions into the ODEs with τ_{II}, the ODEs with $\tau_{\text{II}} \to \infty$ are obtained. Then, in step 2, the transformation from the ODEs with $\tau_{\text{II}} \to \infty$ to those with τ_{III} can be achieved by dividing the former by $\varepsilon_{\text{II,III}}$.

From microsecond scale to millisecond scale

In the ODEs with τ_{III}, the variables that change with $\mathcal{O}(1)$ rates are X_{01}, X_4, Y_{01}, Y_4, T_0 and T_1 (see Appendix B.1.1). There are some combinations among the above variables whose sums only change with $\mathcal{O}(\varepsilon_{\text{III,IV}})$ at τ_{III} scale as $X_{01} + X_4$, $Y_{01} + Y_4$, $T_0 + T_1$, $X_{01} + Y_{01} + T_0$ and $Y_4 + X_4 + T_1$. With the application of step 1, these combinations are introduced as quasi-conserved quantities X_{04}, Y_{04}, T_{01}, E and H:

$$\begin{aligned} X_{04} &\equiv X_{01} + X_4, \\ Y_{04} &\equiv Y_{01} + Y_4, \\ T_{01} &\equiv T_0 + T_1, \\ E &\equiv X_{01} + Y_{01} + T_0, \\ H &\equiv X_4 + Y_4 + T_1 \\ &= X_{04} + Y_{04} + T_{01} - E. \end{aligned} \tag{4.6}$$

Here, X_{04} is the sum of the oxidized and neutral special pairs in the open RC, Y_{04} is the sum of the contributions of oxidized and neutral special pairs in the closed RC, T_{01} is the sum of Y_Z and Y_Z^+ in PS II whose OEC states are S_0, S_1, S_2 and S_3 except for triggered S_3 (S_3^*), E is the sum of neutral states of tyrosine and special

pair, and H is the sum of oxidized (hole) states of tyrosine and special pair. Besides, by assuming the processes at τ_{III} scale are in detailed balance, i.e., by applying the nonequilibrium pseudo-steady state approximation, following coarse-graining functions of X_4, Y_4 and T_1 are derived: $\lim_{\tau_{\text{III}}\to\infty} X_4(\tau_{\text{III}}) \equiv \Gamma_{X_4}, \lim_{\tau_{\text{III}}\to\infty} Y_4(\tau_{\text{III}}) \equiv \Gamma_{Y_4}$ and $\lim_{\tau_{\text{III}}\to\infty} T_1(\tau_{\text{III}}) \equiv \Gamma_{T_1}$. In particular, the first two functions are described as $\Gamma_{X_4} = p(X_4 \mid X_{04})X_{04}$, and $\Gamma_{Y_4} = p(Y_4 \mid Y_{04})Y_{04}$, where $p(X_4 \mid X_{04})$ and $p(Y_4 \mid Y_{04})$ are the probabilities of special pairs to be in neutral states at the open and the close RCs, respectively. (The explicit forms are described in Appendix B.1.2.) The coarse-graining functions of Y_0, X_0 and T_0 are obtained by the quasi-conservation relations: $\lim_{\tau_{\text{III}}\to\infty} X_{01}(\tau_{\text{III}}) \equiv \Gamma_{X_{01}} = X_{04} - \Gamma_{X_4}$, $\lim_{\tau_{\text{III}}\to\infty} Y_{01}(\tau_{\text{III}}) \equiv \Gamma_{Y_{01}} = Y_{04} - \Gamma_{Y_4}$, $\lim_{\tau_{\text{III}}\to\infty} T_0(\tau_{\text{III}}) \equiv \Gamma_{T_0} = T_{01} - \Gamma_{T_1}$.

The coarse-graining of Y_3, which decays with $\mathcal{O}(1)$ at τ_{III} scale, is performed by assuming that the state is in nonequilibrium pseudo-steady state for $\tau_{\text{III}} \to \infty$. The coarse-graining function is thus defined as $\lim_{\tau_{\text{III}}\to\infty} Y_3(\tau_{\text{III}}) \equiv \varepsilon_{\text{II,IV}}\Gamma_{Y_3}$.

Then, the ODEs with $\tau_{\text{III}} \to \infty$ are obtained by employing these coarse-graining functions in the ODEs with τ_{III}. The transformation from the ODEs with $\tau_{\text{III}} \to \infty$ to those with τ_{IV} is achieved by applying step 2, i.e., by dividing the ODEs with $\tau_{\text{III}} \to \infty$ by $\varepsilon_{\text{III,IV}}$. The ODEs with τ_{IV} are thus given (see Appendix B.1.1).

Coarse-grained model of PS II at millisecond scale

The ODEs with τ_{IV} obtained through the HCG method is concisely represented with good accuracy by neglecting the terms which have $\mathcal{O}(\varepsilon_{\text{III,IV}})$ and $\mathcal{O}(\varepsilon_{\text{II,III}})$ of magnitudes. Besides, to represent the ODEs in much simpler way, we normalize the variables as $P_E = E/(R_{\text{T}}+T_{\text{T}})$, $P_{X_{04}} = X_{04}/R_{\text{T}}$, $P_{Z_1} = Z_1/Z_{\text{T}}$, $P_{Z_2} = Z_2/Z_{\text{T}}$, $P_{Q_1} = Q_1/Q_{\text{T}}$, $P_{S_i} = S_i/S_{\text{T}}$, $P_{TS_3^*} = TS_3^*/T_{\text{T}}$ and $P_{TS_4} = TS_4/T_{\text{T}}$. Then, the ODEs with τ_{IV} are represented as

$$
\begin{cases}
\dfrac{dP_E}{d\tau_{\mathrm{IV}}} & = \left[-\Phi_{\mathrm{P}}\nu' + \left\{\kappa_{-2}[\gamma^{\mathrm{d}}_{X_2} + \gamma^{\mathrm{b}}_{X_2}(1-\Phi_{\mathrm{P}})] + \kappa^{\mathrm{d}}_{\mathrm{nr}}\right\}\dfrac{\Gamma_{Y_4}}{R_{\mathrm{T}}}\right]\dfrac{R_{\mathrm{T}}}{R_{\mathrm{T}}+T_{\mathrm{T}}} \\
& \quad + \left[\sum_{i=0}^{2}\kappa_{i*,i}P_{S_i}\dfrac{\Gamma_{T_1}}{T_{\mathrm{T}}} + \kappa_{0,4}P_{TS_4}\right]\dfrac{T_{\mathrm{T}}}{R_{\mathrm{T}}+T_{\mathrm{T}}}, \\
\dfrac{dP_{X_{04}}}{d\tau_{\mathrm{IV}}} & = -\Phi_{\mathrm{P}}\nu' + \left\{\kappa_{-2}[\gamma^{\mathrm{d}}_{X_2} + \gamma^{\mathrm{b}}_{X_2}(1-\Phi_{\mathrm{P}})] + \kappa^{\mathrm{d}}_{\mathrm{nr}}\right\}\dfrac{\Gamma_{Y_4}}{R_{\mathrm{T}}} \\
& \quad + (\kappa_{41}P_{Z_0} + \kappa_{42}P_{Z_1})P_{Y_{04}} - (\kappa_{-41}P_{Z_1} + \kappa_{-42}P_{Z_2})P_{X_{04}}, \\
\dfrac{dP_{Z_1}}{d\tau_{\mathrm{IV}}} & = \kappa_{41}P_{Y_{04}}P_{Z_0} - (\kappa_{42}P_{Y_{04}} + \kappa_{-41}P_{X_{04}})P_{Z_1} + \kappa_{-42}P_{X_{04}}P_{Z_2}, \\
\dfrac{dP_{Z_2}}{d\tau_{\mathrm{IV}}} & = \kappa_{42}P_{Y_{04}}P_{Z_1} - (\kappa_{-42}P_{X_{04}} + \kappa_5 P_{Q_0})P_{Z_2} + \kappa_{-5}P_{Z_0}P_{Q_1}, \\
\dfrac{dP_{Q_1}}{d\tau_{\mathrm{IV}}} & = \dfrac{\kappa_5}{N_{\mathrm{Q}}}P_{Z_2}P_{Q_0} - (\dfrac{\kappa_{-5}}{N_{\mathrm{Q}}}P_{Z_0} + \kappa_6)P_{Q_1}, \\
\dfrac{dP_{S_i}}{d\tau_{\mathrm{IV}}} & = \kappa_{i-1*,i-1}P_{S_{i-1}}\dfrac{\Gamma_{T_1}}{T_{\mathrm{T}}} - \kappa_{i*,i}P_{S_i}\dfrac{\Gamma_{T_1}}{T_{\mathrm{T}}} \qquad (i = 1-3), \\
\dfrac{dP_{TS_3^*}}{d\tau_{\mathrm{IV}}} & = \kappa_{3*,3}P_{S_3}\dfrac{\Gamma_{T_1}}{T_{\mathrm{T}}} - \kappa_{4,3*}P_{TS_3^*} + \kappa_{3*,4}P_{TS_4}, \\
\dfrac{dP_{TS_4}}{d\tau_{\mathrm{IV}}} & = \kappa_{4,3*}P_{TS_3^*} - (\kappa_{3*,4} + \kappa_{0,4})P_{TS_4},
\end{cases}
\tag{4.7a}
$$

where

$$
\begin{cases}
\Phi_{\mathrm{P}} & = \Phi_{\mathrm{P}}(P_E, P_{X_{04}}, P_{Y_{04}}, P_{T_{01}}, P_{Q_1}), \\
\Gamma_{Y_4} & = \Gamma_{Y_4}(P_E, P_{X_{04}}, P_{Y_{04}}, P_{T_{01}}), \\
\Gamma_{T_1} & = \Gamma_{T_1}(P_E, P_{X_{04}}, P_{Y_{04}}, P_{T_{01}}), \\
P_{Y_{04}} & = 1 - P_{X_{04}}, \\
P_{Z_0} & = 1 - P_{Z_1} - P_{Z_2}, \\
P_{Q_0} & = 1 - P_{Q_1}, \\
P_{T_{01}} & = 1 - P_{TS_3^*} - P_{TS_4}, \\
P_{S_0} & = 1 - \sum_{i=1}^{3}P_{S_i} - P_{TS_3^*} - P_{TS_4}.
\end{cases}
\tag{4.7b}
$$

Here, we set $R_{\mathrm{T}} = T_{\mathrm{T}} = S_{\mathrm{T}}$ by assuming that there is no dameged PS II. Besides, we introduce an effective light-excitation rate of core antenna (U_1), $\nu' = (\nu_{U_1} + \nu_{V_1}\gamma^{\mathrm{f}}_{V_1})/R_{\mathrm{T}}$, the quantum efficiency of photochemical process in core antenna, $\Phi_{\mathrm{P}} \equiv \kappa^{\mathrm{o}}_{\mathrm{P}}/(\kappa^{\mathrm{o}}_{\mathrm{P}} + \kappa_{\mathrm{F}} + \kappa_{\mathrm{D}} + \kappa_{\mathrm{C}} + \kappa_{\mathrm{Q}})$, and the ratio of the amount of plastoquinone pool to the amount of PS II (which is equivalent to that of RC or secondary quinone electron acceptor, $\mathrm{Q_B}$), $N_{\mathrm{Q}} = Q_{\mathrm{T}}/Z_{\mathrm{T}}$. Dimensionless rate constants, $\kappa^{\mathrm{o}}_{\mathrm{P}}$, κ_{F}, κ_{D}, κ_{C} and κ_{Q}, are the effective rates of deactivation of excited energy in core antenna (U_1) by charge separation from $\mathrm{P^*_{680}PheQ_A}$, fluorescence, non-radiative dissipation, $\mathrm{P^+_{680}}$ quenching and PQ quenching, respectively. The explicit forms of these effective rates and those

of ν_{U_1}, ν_{V_1} and $\gamma^{\rm f}_{V_1}$ are given in Appendix B.1.2. The diagram of this coarse-grained model is illustrated in Fig. 4.3.

The results of coarse-graining are reflected in the equations for P_E and $P_{X_{04}}$. First, RC is coarse-grained to take two states: X_{04} state ($\mathrm{P_{680}PheQ_A}$ $+\mathrm{P^+_{680}PheQ_A}$) and Y_{04} state ($\mathrm{P_{680}PheQ^-_A + P^+_{680}PheQ^-_A}$). The special pair in each state is in quasi-equilibrium between oxidized and neutral states. Thus, we name this model as double state trapping model (DSTM) in contrast to TSTM. The transition from X_{04} state to Y_{04} state takes place with the rate given by the product of the effective light-excitation rate ν' of the core antenna and the probability $\Phi_{\rm P}$ that an exciton in the core antenna is quenched via charge separation at the open RC. The back transfer from Y_{04} to X_{04} occurs through the non-radiative pathway from Y_4 state ($\mathrm{P^+_{680}Q^-_A}$) to the ground state, the indirect non-radiative pathway from Y_4 state to the ground state via charge separation or intersystem crossing of X_2 state ($\mathrm{P^+_{680}Phe^-}$), and the indirect non-radiative pathway from Y_4 state to the ground state via non-photochemical quenching from the excited state created by charge recombination of X_2 state. The rate of each path is given as the product of the fraction of Y_4 state in RC, $\Gamma_{Y_4}/R_{\rm T}$, and $\kappa^{\rm d}_{\rm nr}$, $\kappa_{-2}\gamma^{\rm d}_{X_2}$ or $\kappa_{-2}\gamma^{\rm b}_{X_2}(1-\Phi_P)$, respectively. Here $\gamma^{\rm d}_{X_2}$ and $\gamma^{\rm b}_{X_2}$ represent the ratios of dissipation flow and back flow to the total outflow from X_2 state, respectively (see Appendix B.1.2).

Second, the equation of the sum of the probabilities of neutral states in $\mathrm{P_{680}}$ and $\mathrm{Y_Z}$, $P_E \equiv P_{X_{01}} + P_{Y_{01}} + P_{T_0}$, describes the electron transfer processes between RC and OEC. This quantity changes temporally with the rate of RC transition (first term on the right-hand side in the first equation of Eq. (4.7a)) and the rate of $\mathrm{Y_Z}$ transition (second term in the first equation of Eq. (4.7a)). Here, the schematic diagram is illustrated in Fig. 4.3(c). On one hand, in regard to the effect of RC, P_E decreases via charge separation from open RC and increases via back transfer from Y_4 to the ground state via direct non-radiative pathway or indirect non-radiative pathway. On the other hand, in regard to the effect of $\mathrm{Y_Z}$, P_E increases via the reduction of $\mathrm{Y^+_Z}$ by S_i $(i = 0-2)$ and via the separation of TS_4 state.

With respect to the pathways of quenching from core antenna except for photochemical quenching, the quantum efficiencies of fluorescence $\Phi_{\rm F}$ and non-radiative dissipation Φ_D are derived through coarse-graining procedure as

$$\begin{aligned}
\Phi_{\rm F} &\equiv \kappa_{\rm F}/(\kappa^{\rm o}_{\rm P} + \kappa_{\rm F} + \kappa_{\rm D} + \kappa_{\rm C} + \kappa_{\rm Q}),\\
\Phi_{\rm D} &\equiv (\kappa_{\rm D} + \kappa_{\rm C} + \kappa_{\rm Q})/(\kappa^{\rm o}_{\rm P} + \kappa_{\rm F} + \kappa_{\rm D} + \kappa_{\rm C} + \kappa_{\rm Q}),
\end{aligned} \tag{4.8}$$

where the relation $\Phi_{\mathrm{P}} + \Phi_{\mathrm{F}} + \Phi_{\mathrm{D}} = 1$ holds.

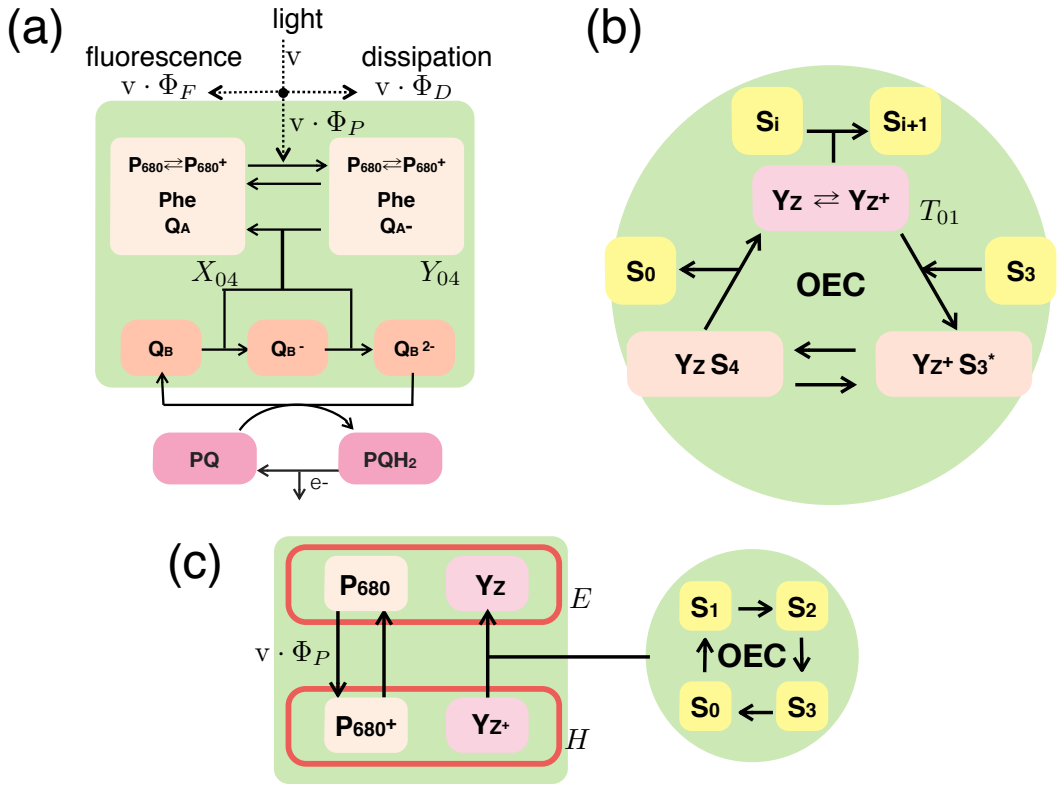

Figure 4.3 Schematic diagram of processes in double state trapping model (DSTM) of PS II, expressed by Eqs. (4.7a) and (4.7b). Solid and dotted lines represent the transfers of electron and excitation energy, respectively. (a) Diagram of processes on the acceptor side of PS II, (b) diagram of processes on the donor side of PS II and (c) diagram of transition of quasi-conserved quantities. The RC takes two quasi variable states in the case (a). S_i for $i = 0 - 2$ react with $\mathrm{Y_Z^+}$ in the case (b). For simplicity, intermediate states of OEC, $\mathrm{Y_Z^+S_3^*}$ and $\mathrm{Y_ZS_4}$ are not indicated in (c). X_{04}, Y_{04}, T_{01}, E and H represent quasi-conserved quantities.

4.2.3 Treatment of the hole transfer from $\mathrm{Y_Z^+}$ to $\mathrm{P_{680}}$

In the studies of PS II based on mathematical models, the hole transfer from $\mathrm{Y_Z^+}$ to $\mathrm{P_{680}}$ has often been neglected when the electron transfer between RC and OEC is considered [19, 67, 68]. In particular, Vredenberg [67–69] constructed a model called three state trapping model (TSTM) which describes the RC with three states based

on the assumption that this hole-transfer process is negligible. While this model is often classified as a different model from EDSTs [15], we will show in the following that a kind of TSTM can be derived from our EDST-like model through the HCG procedure.

The coarse-graining of PS II model in the case that the hole transfer from Y_Z^+ to P_{680} is neglected is carried out in the same way as in the preceding section up to the derivation of the ODEs with τ_{III} because this process is situated in τ_{III} scale. In the following, the ODEs with τ_{IV} in this case are derived. In particular, two different conditions of light intensity are concerned: $v \in A_{IV}$ and $v \in A_{III}$. It is also noted that the rate constant of electron transfer from P_{680} to Y_Z^+ is set as $5 \times 10^6\,\mathrm{s}^{-1}$ in accordance with the literature [19, 68], and the Y_Z^+-quenching, which is assumed to exist in the literature [68, 69], is also taken into account.

From microsecond scale to millisecond scale for $v \in A_{IV}$

First, we consider the coarse-graining in the case of $v \in A_{IV}$. In the case that the hole transfer from Y_Z^+ to P_{680} is neglected, i.e., $k_{-3} = 0$, there is no quasi-conserved quantity in the ODEs with τ_{III} (Eq. (B.9)). Then, we assume that the variables which decay with $\mathcal{O}(1)$, X_4 and Y_4, are in nonequilibrium pseudo-steady states for $\tau_{III} \to \infty$ in step 1. As a result, the coarse-graining functions of X_4 and Y_4, $\lim_{\tau_{III}\to\infty} Y_4(\tau_{III}) \equiv \varepsilon_{III,IV}\Gamma_{Y_4}$ and $\lim_{\tau_{III}\to\infty} X_4(\tau_{III}) \equiv \varepsilon_{III,IV}^2\Gamma_{X_4}$, are obtained (Appendix B.2.2). By substituting these coarse-graining functions into the ODEs with τ_{III}, the ODEs with $\tau_{III} \to \infty$ are obtained.

Then, by applying step 2, the ODEs with $\tau_{III} \to \infty$ are transformed to the ODEs with τ_{IV}. The ODEs with τ_{IV} considering up to $\mathcal{O}(\varepsilon_{III,IV})$ and $\mathcal{O}(\varepsilon_{II,III})$ terms are expressed as

$$
\begin{cases}
\dfrac{dX_{01}}{d\tau_{\mathrm{IV}}} & = -\kappa_1^{\mathrm{o}}\Gamma_{X_1} + (\kappa_{-1}^{\mathrm{o}} + \kappa_{\mathrm{tr}} + \kappa_{\mathrm{nr}}^{\mathrm{ind}})\Gamma_{X_2} + \varepsilon_{\mathrm{III,IV}}\kappa_3\dfrac{T_0}{T_{\mathrm{T}}}\Gamma_{X_4} \\
& + \dfrac{\kappa_{41}Z_0 + \kappa_{42}Z_1}{Z_{\mathrm{T}}}Y_{01} - (\kappa_{-41}Z_1 + \kappa_{-42}Z_2)\dfrac{X_{01}}{R_{\mathrm{T}}} + \varepsilon_{\mathrm{III,IV}}\kappa_{\mathrm{nr}}^{\mathrm{d}}\Gamma_{Y_4}, \\
\dfrac{dY_{01}}{d\tau_{\mathrm{IV}}} & = -\kappa_1^{\mathrm{c}}\Gamma_{Y_1} + (\kappa_{-1}^{\mathrm{c}} + \kappa_{\mathrm{tr}} + \kappa_{\mathrm{nr}}^{\mathrm{ind}})\Gamma_{Y_2} + \kappa_2\Gamma_{X_3} + \kappa_3\dfrac{T_0}{T_{\mathrm{T}}}\Gamma_{Y_4} \\
& - \dfrac{\kappa_{41}Z_0 + \kappa_{42}Z_1}{Z_{\mathrm{T}}}Y_{01} + (\kappa_{-41}Z_1 + \kappa_{-42}Z_2)\dfrac{X_{01}}{R_{\mathrm{T}}} - \kappa_{-2}Y_{01}, \\
\dfrac{dY_3}{d\tau_{\mathrm{IV}}} & = \varepsilon_{\mathrm{II,III}}\kappa_3\dfrac{T_0}{T_{\mathrm{T}}}\Gamma_{Y_2} - \dfrac{\kappa_{41}Z_0 + \kappa_{42}Z_1}{Z_{\mathrm{T}}}Y_3, \\
\dfrac{dZ_1}{d\tau_{\mathrm{IV}}} & = \kappa_{41}\dfrac{Z_0}{Z_{\mathrm{T}}}(Y_{01} + Y_3 + \varepsilon_{\mathrm{III,IV}}\Gamma_{Y_4}) - \kappa_{-41}\dfrac{X_{01}}{R_{\mathrm{T}}}Z_1 \\
& - \kappa_{42}\dfrac{Z_1}{Z_{\mathrm{T}}}(Y_{01} + Y_3 + \varepsilon_{\mathrm{III,IV}}\Gamma_{Y_4}) + \kappa_{-42}\dfrac{X_{01}}{R_{\mathrm{T}}}Z_2, \\
\dfrac{dZ_2}{d\tau_{\mathrm{IV}}} & = \kappa_{42}\dfrac{Z_1}{Z_{\mathrm{T}}}(Y_{01} + Y_3 + \varepsilon_{\mathrm{III,IV}}\Gamma_{Y_4}) - \kappa_{-42}\dfrac{X_{01}}{R_{\mathrm{T}}}Z_2 - \kappa_5 Z_2\dfrac{Q_0}{Q_{\mathrm{T}}} + \kappa_{-5}Z_0\dfrac{Q_1}{Q_{\mathrm{T}}}, \\
\dfrac{dQ_1}{d\tau_{\mathrm{IV}}} & = \kappa_5 Z_2\dfrac{Q_0}{Q_{\mathrm{T}}} - \kappa_{-5}Z_0\dfrac{Q_1}{Q_{\mathrm{T}}} - \kappa_6 Q_1, \\
\dfrac{dT_1}{d\tau_{\mathrm{IV}}} & = -\sum_{i=0}^{3}\kappa_{i*,i}\dfrac{S_i}{S_{\mathrm{T}}}T_1 + \kappa_3\dfrac{T_0}{T_{\mathrm{T}}}[\varepsilon_{\mathrm{II,III}}(\Gamma_{X_2} + \Gamma_{Y_2}) + \Gamma_{Y_4} + \varepsilon_{\mathrm{III,IV}}\Gamma_{X_4}], \\
\dfrac{dS_i}{d\tau_{\mathrm{IV}}} & = \kappa_{i-1*,i-1}\dfrac{S_{i-1}}{S_{\mathrm{T}}}T_1 - \kappa_{i*,i}\dfrac{S_i}{S_{\mathrm{T}}}T_1 \qquad (i = 1-3), \\
\dfrac{dTS_3^*}{d\tau_{\mathrm{IV}}} & = \kappa_{3*,3}\dfrac{S_3}{S_{\mathrm{T}}}T_1 - \kappa_{4,3*}TS_3^* + \kappa_{3*,4}TS_4, \\
\dfrac{dTS_4}{d\tau_{\mathrm{IV}}} & = \kappa_{4,3*}TS_3^* - (\kappa_{3*,4} + \kappa_{0,4})TS_4,
\end{cases}
\tag{4.9a}
$$

$$
\begin{cases}
T_0 & = T_{\mathrm{T}} - T_1 - TS_3^* - TS_4, \\
S_0 & = S_{\mathrm{T}} - \sum_{i=1}^{3} S_i - TS_3^* - TS_4, \\
Z_0 & = Z_{\mathrm{T}} - Z_1 - Z_2, \\
Q_0 & = Q_{\mathrm{T}} - Q_1.
\end{cases}
\tag{4.9b}
$$

The schematic diagram of this model is illustrated in Fig. 4.2.3. In this coarse-grained model, the RC takes three different states, X_{01}, Y_{01} and Y_3. These three states, $\mathrm{P_{680}PheQ_A}$, $\mathrm{P_{680}PheQ_A^-}$ and $\mathrm{P_{680}Phe^-Q_A^-}$, are the same as the states which were assumed for RC in TSTM by Vredenberg [67–69].

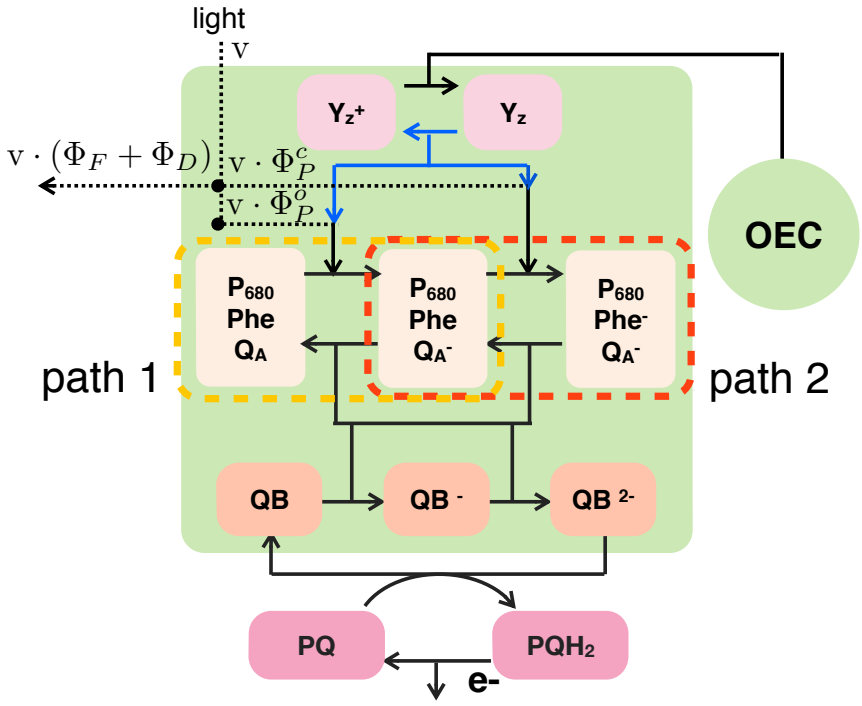

Figure 4.4 Schematic diagram of three state trapping model (TSTM) of PS II expressed by eqs 4.9a and 4.9b. Solid and dotted lines represent the transfers of electron and excitation energy, respectively. Each yellow and red dashed line indicates the transition path 1 of RC state that is dominant for $v \in A_{\mathrm{IV}}$, and the path 2 that is not negligible for $v \in A_{\mathrm{III}}$.

In particular, by neglecting the terms of $\mathcal{O}(\varepsilon_{\mathrm{III,IV}})$ and $\mathcal{O}(\varepsilon_{\mathrm{II,III}})$, and normalizing the variables as $P_{X_{01}} = X_{01}/R_{\mathrm{T}}$, $P_{Z_1} = Z_1/Z_{\mathrm{T}}$, $P_{Z_2} = Z_2/Z_{\mathrm{T}}$, $P_{Q_1} = Q_1/Q_{\mathrm{T}}$, $P_{S_i} = S_i/S_{\mathrm{T}}$, $P_{TS_3^*} = TS_3^*/S_{\mathrm{T}}$ and $P_{TS_4} = TS_4/S_{\mathrm{T}}$, the ODEs on the acceptor side of PS II are concisely represented as

$$\begin{cases} \dfrac{dP_{X_{01}}}{d\tau_{\mathrm{IV}}} &= -\nu'\Phi_{\mathrm{P}}^{\mathrm{o}} + (\kappa_{41}P_{Z_0} + \kappa_{42}P_{Z_1})P_{Y_{01}} - (\kappa_{-41}P_{Z_1} + \kappa_{-42}P_{Z_2})P_{X_{01}}, \\ \dfrac{dP_{Z_1}}{d\tau_{\mathrm{IV}}} &= (\kappa_{41}P_{Z_0} - \kappa_{42}P_{Z_1})P_{Y_{01}} - (\kappa_{-41}P_{Z_1} - \kappa_{-42}P_{Z_2})P_{X_{01}}, \\ \dfrac{dP_{Z_2}}{d\tau_{\mathrm{IV}}} &= \kappa_{42}P_{Z_1}P_{Y_{01}} - \kappa_{-42}P_{Z_2}P_{X_{01}} - \kappa_5 P_{Z_2}P_{Q_0} + \kappa_{-5}P_{Z_0}P_{Q_1}, \\ \dfrac{dP_{Q_1}}{d\tau_{\mathrm{IV}}} &= \dfrac{\kappa_5}{N_{\mathrm{Q}}}P_{Z_2}P_{Q_0} - \dfrac{\kappa_{-5}}{N_{\mathrm{Q}}}P_{Z_0}P_{Q_1} - \kappa_6 P_{Q_1}, \end{cases} \tag{4.10a}$$

$$\begin{cases} P_{Y_{01}} &= 1 - P_{X_{01}}, \\ P_{Z_0} &= 1 - P_{Z_1} - P_{Z_2}, \\ P_{Q_0} &= 1 - P_{Q_1}, \end{cases} \tag{4.10b}$$

and those on the donor side are expressed as

$$\begin{cases} \dfrac{dP_{T_1}}{d\tau_{\mathrm{IV}}} &= \nu' \Phi_{\mathrm{P}}^{\mathrm{o}} - \displaystyle\sum_{i=0}^{3} \kappa_{i*,i} P_{S_i} P_{T_1}, \\ \dfrac{dP_{S_i}}{d\tau_{\mathrm{IV}}} &= \kappa_{i-1*,i-1} P_{S_{i-1}} P_{T_1} - \kappa_{i*,i} P_{S_i} P_{T_1} \qquad (i = 1-3), \\ \dfrac{dP_{TS_3^*}}{d\tau_{\mathrm{IV}}} &= \kappa_{3*,3} P_{S_3} P_{T_1} - \kappa_{4,3*} P_{TS_3^*} + \kappa_{3*,4} P_{TS_4}, \\ \dfrac{dP_{TS_4}}{d\tau_{\mathrm{IV}}} &= \kappa_{4,3*} P_{TS_3^*} - (\kappa_{3*,4} + \kappa_{0,4}) P_{TS_4}, \end{cases} \tag{4.11a}$$

$$\begin{cases} P_{T_0} &= 1 - P_{T_1} - P_{TS_3^*} - P_{TS_4}, \\ P_{S_0} &= 1 - \displaystyle\sum_{i=1}^{3} P_{S_i} - P_{TS_3^*} - P_{TS_4}. \end{cases} \tag{4.11b}$$

Here the effective light-excitation rate of core antenna, $\nu' = (\nu_{U_1} + \nu_{V_1}\gamma_{V_1}^{\mathrm{f}})/R_{\mathrm{T}}$, the ratio $N_{\mathrm{Q}} = Q_{\mathrm{T}}/Z_{\mathrm{T}}$ of the amount of plastoquinon to the whole PS II, the quantum efficiency of charge separation in open RC at core antenna, $\Phi_{\mathrm{P}}^{\mathrm{o}} = \kappa_{\mathrm{P}}^{\mathrm{o}}/(\kappa_{\mathrm{F}} + \kappa_{\mathrm{P}}^{\mathrm{o}} + \kappa_{\mathrm{D}} + \kappa_{\mathrm{C}} + \kappa_{\mathrm{Q}} + \kappa_{\mathrm{Z}})$, and the $\mathrm{Y_Z^+}$-quenching rate, $\kappa_{\mathrm{Z}} \equiv \kappa_{\mathrm{z}}(T_1 + TS_3^*)$, are introduced. This coarse-grained model is separated into RC system (Eqs. (4.10a) and (4.10b)) and OEC system (Eqs. (4.11a) and (4.11b)) with respect to electron transfer. This means that the supply of electron from donor side of PS II to RC is always enough (sufficiently fast in time) and thus the rate of charge separation is not limited by the Kok cycle in OEC. However, in the case that $\mathrm{Y_Z^+}$ quenching is taken into account, the temporal evolution of RC is affected by that of $\mathrm{Y_Z^+}$. Besides, the RC takes two states which do not include the oxidized special pair in this case. This means that reaction pathway "path 2" indicated in Fig. 4.2.3 is negligible and thus the "path 1" reaction is dominant with respect to the transition of RC state. Because of little accumulation of Y_4 state ($\mathrm{P_{680}^+Q_A^-}$), which is associated with the absence of hole transfer from $\mathrm{Y_Z^+}$ to $\mathrm{P_{680}}$, the effect of non-radiative pathways from Y_4 state to the ground state of open RC is negligible and thus not included in this model. In this way, the transition of RC proceeds only in path 1 in Fig. 4.2.3.

From microsecond scale to millisecond scale for $v \in A_{\text{III}}$

In this subsection, the coarse graining in the case of $v \in A_{\text{III}}$ is considered. In this case, the light-excitation rate is scaled as $\nu = v/k_3$ and the coarse graining functions are defined by factoring out $\varepsilon_{\text{II,III}}$ as $\lim_{\tau_{\text{II}}\to\infty} U_1(\tau_{\text{II}}) \equiv \varepsilon_{\text{II,III}}\Gamma_{U_1}$, $\lim_{\tau_{\text{II}}\to\infty} X_1(\tau_{\text{II}}) \equiv \varepsilon_{\text{II,III}}\Gamma_{X_1}$, $\lim_{\tau_{\text{II}}\to\infty} Y_1(\tau_{\text{II}}) \equiv \varepsilon_{\text{II,III}}\Gamma_{Y_1}$, $\lim_{\tau_{\text{II}}\to\infty} X_2(\tau_{\text{II}}) \equiv \varepsilon_{\text{II,III}}\Gamma_{X_2}$, $\lim_{\tau_{\text{II}}\to\infty} Y_2(\tau_{\text{II}}) \equiv \varepsilon_{\text{II,III}}\Gamma_{Y_2}$ and $\lim_{\tau_{\text{II}}\to\infty} X_3(\tau_{\text{II}}) \equiv \varepsilon_{\text{II,IV}}\Gamma_{X_3}$. (The explicit forms of coarse-graining functions are given in Appendix B.2.3.)

The variables which decay with $\mathcal{O}(1)$ rates in the ODEs with τ_{III} are X_{01}, X_4 and Y_4. In step 1 treatments, these variables are assumed to be in nonequilibrium quasi-steady states for $\tau_{\text{III}} \to \infty$. Thus, the coarse-graining functions of these variables are obtained as $\lim_{\tau_{\text{III}}\to\infty} X_{01}(\tau_{\text{III}}) \equiv \varepsilon_{\text{III,IV}}\Gamma_{X_{01}}$,
$\lim_{\tau_{\text{III}}\to\infty} Y_4(\tau_{\text{III}}) \equiv \varepsilon_{\text{III,IV}}\Gamma_{Y_4}$, and $\lim_{\tau_{\text{III}}\to\infty} X_4(\tau_{\text{III}}) \equiv \varepsilon^2_{\text{III,IV}}\Gamma_{X_4}$. By substituting these results to the ODEs with τ_{III}, the ODEs with $\tau_{\text{III}} \to \infty$ are obtained. Then, by applying step 2, the transformation to the ODEs with τ_{IV} is carried out.

By neglecting the $\mathcal{O}(\varepsilon_{\text{III,IV}})$ and $\mathcal{O}(\varepsilon_{\text{II,III}})$ terms, and normalizing the variables as $P_{Y_{01}} = Y_{01}/R_{\text{T}}, P_{Z_1} = Z_1/Z_{\text{T}}, P_{Z_2} = Z_2/Z_{\text{T}}$, $P_{Q_1} = Q_1/Q_{\text{T}}$, $P_{S_i} = S_i/S_{\text{T}}$, $P_{TS_3^*} = TS_3^*/S_{\text{T}}$ and $P_{TS_4} = TS_4/S_{\text{T}}$, the ODEs with τ_{IV} on the acceptor and donor sides of PS II are concisely expressed as

$$\begin{cases} \dfrac{dP_{Y_{01}}}{d\tau_{\text{IV}}} &= -\dfrac{\nu'}{\varepsilon_{\text{III,IV}}}\Phi_{\text{P}}^{\text{c}} + (\kappa_{41}P_{Z_0} + \kappa_{42}P_{Z_1})P_{X_{01}}, \\ \dfrac{dP_{Z_1}}{d\tau_{\text{Iv}}} &= \kappa_{41}P_{Z_0} - \kappa_{42}P_{Z_1}, \\ \dfrac{dP_{Z_2}}{d\tau_{\text{IV}}} &= \kappa_{42}P_{Z_1} - \kappa_5 P_{Z_2}P_{Q_0} + \kappa_{-5}P_{Z_0}P_{Q_1}, \\ \dfrac{dP_{Q_1}}{d\tau_{\text{IV}}} &= \dfrac{\kappa_5}{N_{\text{Q}}}P_{Z_2}P_{Q_0} - \dfrac{\kappa_{-5}}{N_{\text{Q}}}P_{Z_0}P_{Q_1} - \kappa_6 P_{Q_1}, \end{cases} \tag{4.12a}$$

$$\begin{cases} P_{Y_3} &= 1 - P_{Y_{01}}, \\ P_{Z_0} &= 1 - P_{Z_1} - P_{Z_2}, \\ P_{Q_0} &= 1 - P_{Q_1}, \end{cases} \tag{4.12b}$$

and

$$\begin{cases} \dfrac{dP_{T_1}}{d\tau_{\mathrm{IV}}} & = \dfrac{\nu'}{\varepsilon_{\mathrm{III,IV}}}\Phi_{\mathrm{P}}^{\mathrm{c}} + \kappa_3 P_{T_0}\dfrac{\Gamma_{Y_4}}{R_{\mathrm{T}}} - \displaystyle\sum_{i=0}^{3}\kappa_{i*,i}P_{S_i}P_{T_1}, \\ \dfrac{dP_{S_i}}{d\tau_{\mathrm{IV}}} & = \kappa_{i-1*,i-1}P_{S_{i-1}}P_{T_1} - \kappa_{i*,i}P_{S_i}P_{T_1} \qquad (i=1-3), \\ \dfrac{dP_{TS_3^*}}{d\tau_{\mathrm{IV}}} & = \kappa_{3*,3}P_{S_3}P_{T_1} - \kappa_{4,3*}P_{TS_3^*} + \kappa_{3*,4}P_{TS_4}, \\ \dfrac{dP_{TS_4}}{d\tau_{\mathrm{IV}}} & = \kappa_{4,3*}P_{TS_3^*} - (\kappa_{3*,4}+\kappa_{0,4})P_{TS_4}, \end{cases} \tag{4.13a}$$

$$\begin{cases} P_{T_0} & = 1 - P_{T_1} - P_{TS_3^*} - P_{TS_4}, \\ P_{S_0} & = 1 - \displaystyle\sum_{i=1}^{3}P_{S_i} - P_{TS_3^*} - P_{TS_4}, \end{cases} \tag{4.13b}$$

respectively. Here, the light-excitation rate of core antenna, $\nu' = (\nu_{U_1} + \nu_{V_1}\gamma_{V_1}^{\mathrm{f}})/R_{\mathrm{T}}$, the ratio of plastoquinone to PS II, $N_{\mathrm{Q}} = Q_{\mathrm{T}}/Z_{\mathrm{T}}$, and the quantum efficiency of charge separation from closed RC, $\Phi_{\mathrm{P}}^{\mathrm{c}} = \kappa_{\mathrm{P}}^{\mathrm{c}}/(\kappa_{\mathrm{F}} + \kappa_{\mathrm{D}} + \kappa_{\mathrm{P}}^{\mathrm{o}} + \kappa_{\mathrm{P}}^{\mathrm{c}} + \kappa_{\mathrm{C}} + \kappa_{\mathrm{Q}} + \kappa_{\mathrm{Z}})$, are introduced. In this model, the RC takes two states, Y_{01} and Y_3, which are different from those for the model in the $v \in A_{\mathrm{IV}}$ case. This difference reflects that the path 2, which is negligible in $v \in A_{\mathrm{IV}}$ case, is not negligible in this case. The transition from Y_{01} state ($\mathrm{P_{680}PheQ_A^-}$) to Y_3 state ($\mathrm{P_{680}Phe^-Q_A^-}$)occurs with the rate given as the product of the effective light-excitation rate $\varepsilon_{\mathrm{III,IV}}^{-1}\nu$ of core antenna scaled to τ_{IV} scale and the quantum efficiency of charge separation $\Phi_{\mathrm{P}}^{\mathrm{c}}$ ($\sim \mathcal{O}(\varepsilon_{\mathrm{II,III}})$) from the closed RC at core antenna. We note that the path 1 is active in this model though there is no variable which explicitly expresses this path. The effects of this path are reflected in the term describing the electron transfer rate from RC to Z_0 and Z_1 states. The reason why these rate are proportional to the amount of donors is that all RCs in this model, Y_{01} and Y_3 states, always have the ability to supply electrons to the downstream side. This means that the electron flow from Y_{01} state to X_{01} state ($\mathrm{P_{680}PheQ_A}$) exists. In this case the transition from X_{01} to Y_{01} proceeds sufficiently fast in contrast to the transition from Y_{01} to X_{01}, and thus the transition of X_{01} is invisible at the τ_{IV} scale.

4.3 Results

FI is known to change the time-course pattern from the O-J-I-P type to the O-J-D-I-P type, the latter having a dip D after the inflection point J depending on the light intensity [71, 72]. The experimental results at various light-intensity conditions

are illustrated in Fig. 4.5. In this section, this light-intensity dependent change of FI pattern is simulated and analyzed based on the coarse-grained models derived in the preceding section by assuming the dark adapted condition.

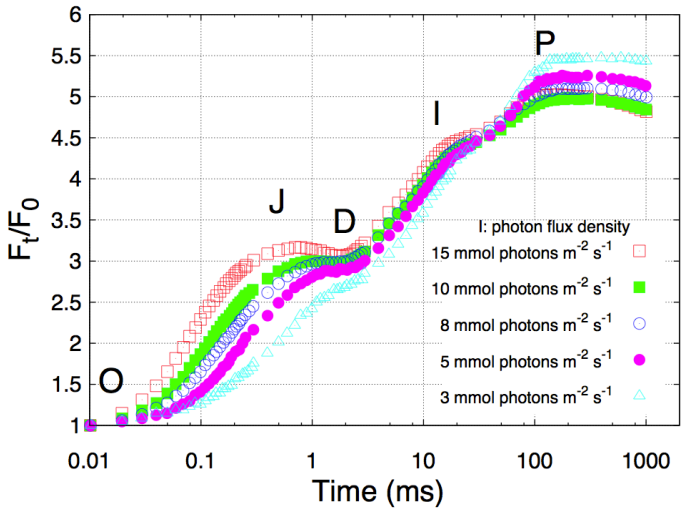

Figure 4.5 The intensity of fluorescence as a function of time for various incident photon flux densities. The change of pattern of FI is observed depending on the incident photon intensity at, $I = 3,\ 5,\ 8,\ 10,\ 15\,\mathrm{mmol\,photons\,m^{-2}\,s^{-1}}$, from Pea Leaf. The intensity of fluorescence is normalized by the value at $t = 0$, F_0. (Modified from Schansker *et al.* [71].)

4.3.1 Results based on the DSTM

I present here the results of the reduced set of ordinary differential equations based on the DSTM, which are expressed by Eqs. (4.7a) and (4.7b), and illustrated in Fig. 4.3. These equations are obtained by applying the HCG method to the full PS II model including the process of hole transfer from $\mathrm{Y_Z^+}$ to $\mathrm{P_{680}}$. The initial condition of the variables are set as those for non-reduced states, i.e., $P_E = 2, P_{X_{04}} = 1, P_{Z_0} = 1, P_{Q_0} = 1, P_{T_{01}} = 1, P_{S_0} = 0.25, P_{S_1} = 0.75$, and otherwise 0.

In the following results, there are no units of concentration because we simulate the dynamics of the probabilities of each variable state which are defined as the ratios of each concentration to the total concentration. The ratio of total amounts, PSII/ OEC/ LHC II / PQ pool, is assumed to be 1/1/1/8 for the simulation. Besides, the light-excitation rate v for PS II is employed for the simulation. Here, $v = 4,000\,\mathrm{s^{-1}}$

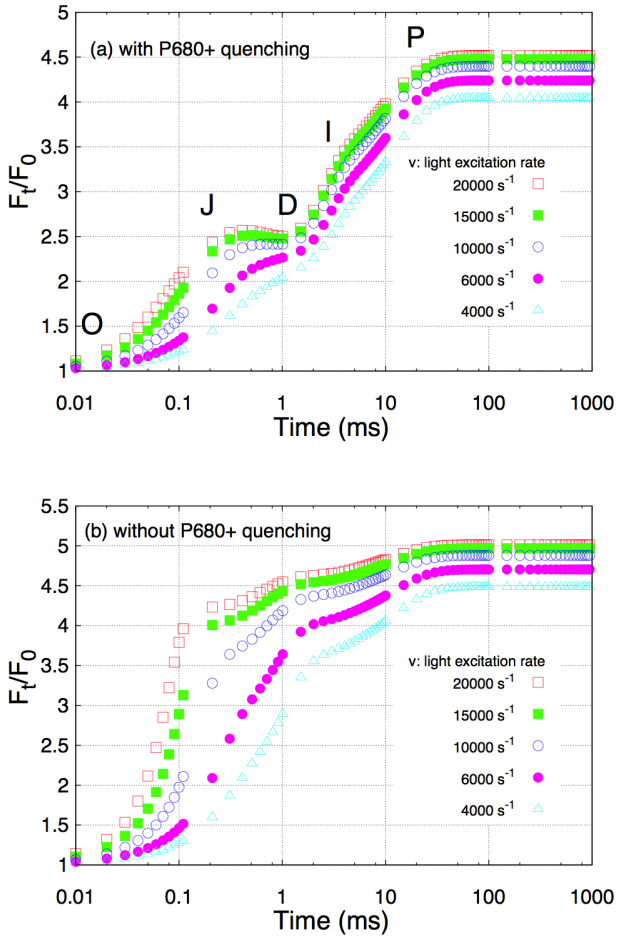

Figure 4.6 Simulated FIs with various light excitation rates, (a) for the case with P^{+}_{680}-quenching and (b) for those without. Light excitation rate for PS II, v, is set as $4,000$, $6,000$, $10,000$, $15,000$ and $20,000\,\mathrm{s}^{-1}$. The fluorescence intensity is normalized by the value at $t = 0$, F_0.

corresponds approximately to the light-flux density of $3\,\mathrm{mmol\,photons\,m^{-2}\,s^{-1}}$ [12]. This estimation is based on the chlorophyll $(a + b)$ concentration in a green leaf (about 15 $\mu\mathrm{mol\,cm^{-2}}$) and the average chlorophyll $(a + b)$ molecular mass ($900\mathrm{g\,mol^{-1}}$). These lead to 0.017 $\mu\mathrm{mol\,cm^{-2}}$ chlorophyll $(a + b)$ concentration. If light irradiance of 3 $\mathrm{mmol\,m^{-2}s^{-1}}$ is used, the ratio $(3\mathrm{m\,mol\,m^{-2}\,s^{-1}})/(0.017\mu\mathrm{mol\,cm^{-2}})$ gives the excitation rate of one chlorophyll as $18\,\mathrm{s^{-1}}$. Then, assuming 250 chlorophylls per PS II, the excitation rate of one PS ll is given as $4500\,\mathrm{s^{-1}}$. If 80-90 % of irradiance is absorbed, the excitation rate is estimated as $3600\,\mathrm{s^{-1}}$ to $4050\,\mathrm{s^{-1}}$.

Simulated FIs for various light intensities are plotted in Fig. 4.6. In previous ex-

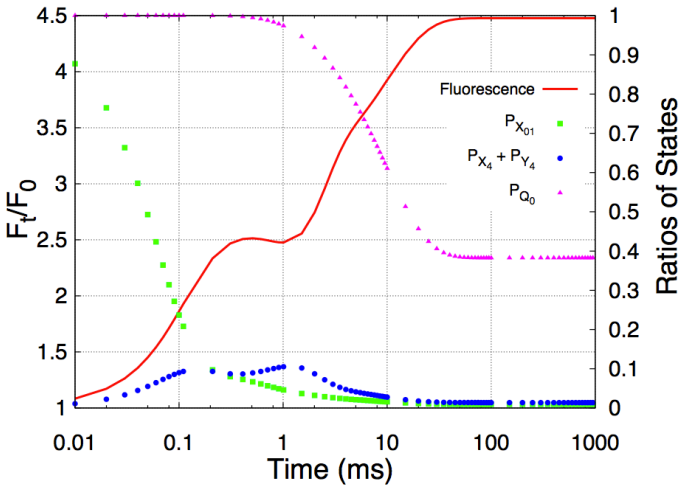

Figure 4.7 Simulated FI (red solid line, left axis) and time courses of the occupancy ratios of quenchers (right axis) at $v = 15,000\,\mathrm{s}^{-1}$. $P_{X_{01}}$(green square), $P_{X_4} + P_{Y_4}$(blue circle) and P_{Q_0}(magenta triangle) indicate the occupancy ratios of each quencher, $\mathrm{P_{680}PheQ_A}$, $\mathrm{P^+_{680}}$ and PQ, respectively. The fluorescence intensity is normalized by the value at $\tau_{\mathrm{IV}} = 0$, F_0.

perimental studies [71, 72], the light-intensity dependent changes of the FI transient pattern from the O-J-I-P to the O-J-D-I-P were observed. In our simulation, the $\mathrm{P^+_{680}}$ quenching is taken into account in the case (a) and neglected (i.e., setting the $\mathrm{P^+_{680}}$-quenching rate $k_{\mathrm{c}} = 0$) in the case (b). In the case (a), the light-intensity dependent changes of the FI pattern from O-J-I-P to O-J-D-I-P are reproduced well. These changes are in accord with the experimental results shown in Fig. 4.5. In the case (b), in contrast, the fluorescence transient pattern of J-D-I does not appear even if the light intensity is high. These results suggest that the appearance of the fluorescence transient pattern J-D-I reflects the presence of $\mathrm{P^+_{680}}$ quenching.

The time courses of the occupancies of $\mathrm{P_{680}PheQ_A}$, $\mathrm{P^+_{680}}$ and PQ, denoted respectively as $P_{X_{01}}$, $P_{X_4} + P_{Y_4}$ and P_{Q_0}, are plotted with FI at $v = 15,000\,\mathrm{s}^{-1}$ in Fig. 4.7. The ratio of the X_{01} state to total RC, $P_{X_{01}}$, which is set as $P_{X_{04}} = 1$ at $t = 0$, rapidly decreases until the J peak appears. At the same time, the ratio of $\mathrm{P^+_{680}}$ in RC, $P_{X_4} + P_{Y_4}$, gradually increases. Then the fluorescence intensity increases, which means that the magnitude of decrease of the rate of photochemical quenching, $\kappa^{\mathrm{o}}_{\mathrm{P}}$, via charge separation from open RC is larger than that of increase of the $\mathrm{P^+_{680}}$-quenching rate, κ_{C}, and thus the quantum efficiency Φ_{F} of fluorescence increases. After the

decreasing rate of $P_{X_{01}}$ slows down, $P_{X_4} + P_{Y_4}$ increases again. Then the peak J appears, indicating that Φ_{F} starts decreasing according to the increase of κ_{C}. Subsequently, $P_{X_4} + P_{Y_4}$ continues to increase and then comes to a peak at about 1 ms. At this time, κ_{C} and Φ_{F} take a local maximum and a local minimum, respectively, and the dip D appears. Thereafter, Φ_{F} increases along with the decrease of $P_{X_4} + P_{Y_4}$. The inflection point I of FI appears when the decreasing rate of $P_{X_4} + P_{Y_4}$ decelerates. Subsequently, the fluorescence intensity continues increasing under the effects not only of photochemical quenching and P^+_{680} quenching but also of PQ quenching. Finally, the peak P appears when the PQ and all other states come to steady states.

To analyze the situations of electron flows of PS II system, the ratios of the rate of outflux to that of influx concerning each state of electron donors/acceptors are plotted with FI at $v = 15,000\,\mathrm{s}^{-1}$ in Fig. 4.8. The P^+_{680} quenching is taken into account in the case (a) and neglected (i.e., $k_{\mathrm{c}} = 0$) in the case (b). The ratios of outflux to influx concerning the transitions of the following states, $\mathrm{Q}^-_{\mathrm{A}}(\mathrm{P}_{680}\mathrm{PheQ}^-_{\mathrm{A}} + \mathrm{P}^+_{680}\mathrm{PheQ}^-_{\mathrm{A}})$, $\mathrm{Q}^{2-}_{\mathrm{B}}$, PQ, $\mathrm{Y}^+_{\mathrm{Z}} + \mathrm{P}^+_{680}$ and $\mathrm{Y}_{\mathrm{Z}} + \mathrm{Y}^+_{\mathrm{Z}}$, are indicated as $V^{Y_{04}}_{\mathrm{out}}/V^{Y_{04}}_{\mathrm{in}}$, $V^{Z_2}_{\mathrm{out}}/V^{Z_2}_{\mathrm{in}}$,$V^{Q_1}_{\mathrm{out}}/V^{Q_1}_{\mathrm{in}}$,$V^{H}_{\mathrm{out}}/V^{H}_{\mathrm{in}}$ and $V^{T_{01}}_{\mathrm{out}}/V^{T_{01}}_{\mathrm{in}}$, respectively. Here, V^{x}_{out} and V^{x}_{in} indicate the sum of the rates of outfluxes from the state x and those of influxes into the state x in ODEs, respectively. Concerning the case (b) where P^+_{680} quenching is neglected, it is clear that the timings at which the characters J', I' and P' of FI appear in the diagram correspond to those at which $V^{Y_{04}}_{\mathrm{out}}/V^{Y_{04}}_{\mathrm{in}}$, $V^{Z_2}_{\mathrm{out}}/V^{Z_2}_{\mathrm{in}}$ and $V^{Q_1}_{\mathrm{out}}/V^{Q_1}_{\mathrm{in}}$ become almost unity. This means that each pattern of FI, i.e., J', I' or P', reflects that the transition of $\mathrm{Q}^-_{\mathrm{A}}$, $\mathrm{Q}^{2-}_{\mathrm{B}}$ or PQ state has come to the quasi-steady state, respectively. This correspondence indicates that the amount of $\mathrm{Q}^-_{\mathrm{A}}$, which governs Φ_{F} via photochemical quenching rate, $\kappa^{\mathrm{o}}_{\mathrm{P}}$, changes with the rate affected by the states of donors/acceptors, Q_{A}, Q_{B} and PQ, on the downstream side of PS II, which become to steady states in turn. On the other hand, in the case (a) where P^+_{680} quenching is taken into account, the FI pattern does not clearly reflect anymore the timings at which Q_{A} and Q_{B} have become quasi-steady states. In this case, the peak J and the dip D appear after the transition of Q_{A} state comes to a quasi-steady state. The timing at which the inflection point I appears corresponds to that at which H and T_{01} have come to quasi-steady states. This means that the Kok cycle, which represents the transition of states of OEC located on the donor side of PS II, has become a quasi-steady state. At this time, the decreasing rate of the P^+_{680} state starts decelerating since P^+_{680} accepts electrons provided by OEC. This causes the decelerations of the decrease of P^+_{680}-quenching rate κ_{C}, and the increase of the

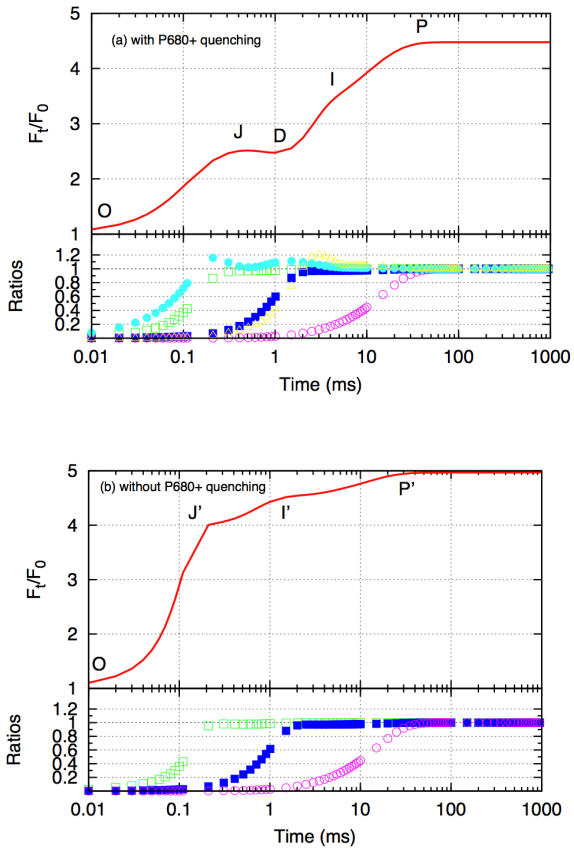

Figure 4.8 Simulated FI (upper graph) and the ratios of fluxes about electron donors/acceptors (lower graph) at $v = 15,000\,\mathrm{s}^{-1}$ for the case (a) where P_{680}^{+}-quenching is taken into account and (b) neglected. The ratios of outflux to influx about each variable state, $\mathrm{Q}_{\mathrm{A}}^{-}(Y_{04})$, $\mathrm{Q}_{\mathrm{B}}^{2-}(Z_2)$, $\mathrm{PQ}(Q_0)$, $\mathrm{P}_{680}^{+} + \mathrm{Y}_{\mathrm{Z}}^{+}(H)$ and $\mathrm{Y}_{\mathrm{Z}} + \mathrm{Y}_{\mathrm{Z}}^{+}(T_{01})$, are defined as $V_{\mathrm{out}}^{Y_{04}}/V_{\mathrm{in}}^{Y_{04}}$ (green open square), $V_{\mathrm{out}}^{Z_2}/V_{\mathrm{in}}^{Z_2}$ (blue closed square), $V_{\mathrm{out}}^{Q_1}/V_{\mathrm{in}}^{Q_1}$ (magenta open circle), $V_{\mathrm{out}}^{H}/V_{\mathrm{in}}^{H}$ (aqua closed circle) and $V_{\mathrm{out}}^{T_{01}}/V_{\mathrm{in}}^{T_{01}}$ (yellow open triangle), respectively. The fluorescence intensity is normalized by the value F_0 at $t = 0$.

quantum efficiency Φ_{F} of fluorescence. The timing at which the peak P appears corresponds to that at which PQ has come to a steady state in the same way as in the case (b).

4.3.2 Results based on the TSTM

The TSTM, expressed by Eqs. (4.9a) and (4.9b), and illustrated in Fig. 4.2.3, is obtained by applying the HCG method to the full PS II model without the process

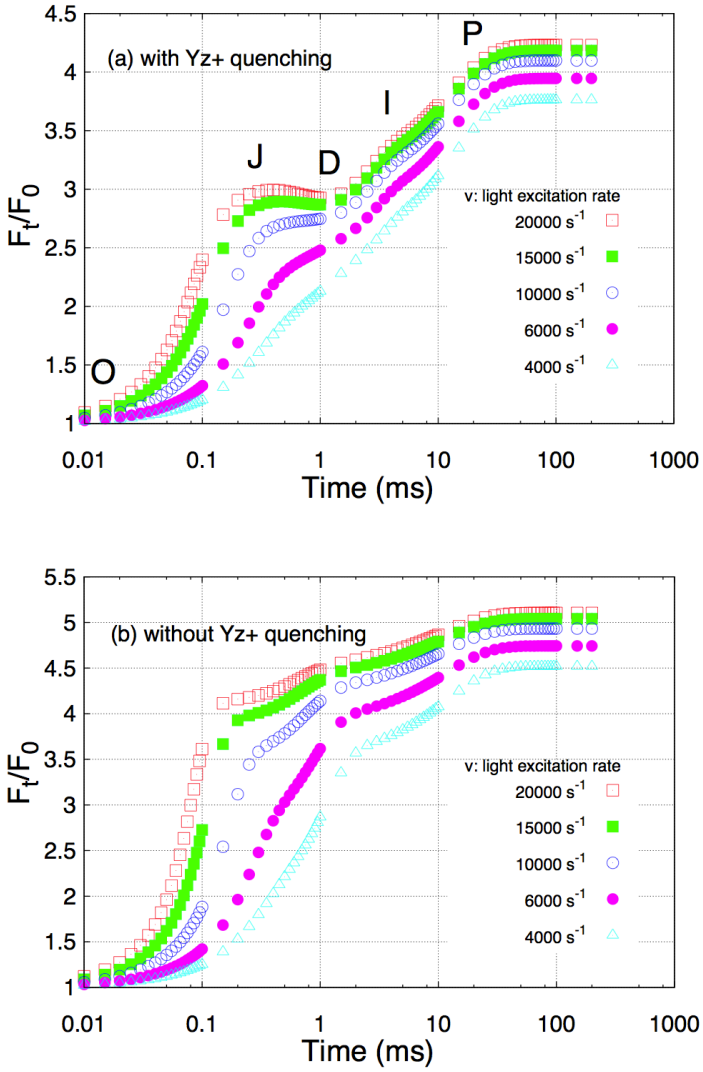

Figure 4.9 Simulated FIs with various photoexcitation rates (a) for the case with Y_Z^+ quenching and (b) for those without. Photoexcitation rate for PS II v is set as $4,000$, $6,000$, $10,000$, $15,000$ and $20,000\,s^{-1}$. The fluorescence intensity is normalized by the value at $\tau_{IV} = 0$, F_0.

of hole transfer from Y_Z^+ to P_{680}. The results based on this model are presented below. The initial values of the variables are set as $P_{X_{01}} = 1, P_{T_0} = 1, P_{Z_0} = 1, P_{Q_0} = 1, P_{S_0} = 0.25, P_{S_1} = 0.75$, and otherwise 0.

Simulated FIs for various incident light intensities are plotted in Fig. 4.9. In the case (a) Y_Z^+, P_{680}^+ and PQ quenchings are taken into account, while in the case (b) only P_{680}^+ and PQ quenchings are taken into account but Y_Z^+ quenching is neglected. The Y_Z^+ quenching is due to a hypothetical quencher which was proposed in Vredenberg's

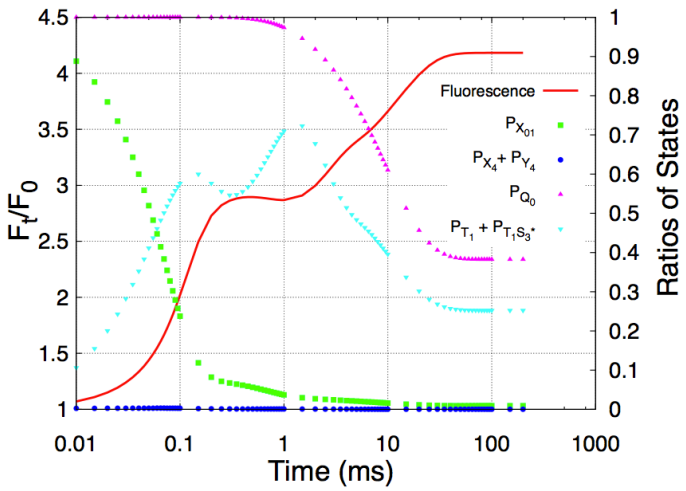

Figure 4.10 Simulated FI and time course of the states of quenchers at $v = 15,000\,\mathrm{s}^{-1}$. The FI (red solid line, left axis) and the ratios of quenchers to each of their maximum values (right axis) are plotted. $P_{X_{01}}$ (green square), $P_{X_4} + P_{Y_4}$ (blue circle), P_{Q_0} (magenta triangle) and $P_{T_1} + P_{TS_3^*}$ (aqua inverted triangle), correspond to the quenchers $\mathrm{P_{680}PheQ_A}$, $\mathrm{P_{680}^+}$, PQ and $\mathrm{Y_Z^+}$, respectively. The fluorescence intensity is normalized by the value at $\tau_{\mathrm{IV}} = 0$, F_0.

FIA [69]. We set this $\mathrm{Y_Z^+}$-quenching rate to $k_{\mathrm{z}} = 10^8\,\mathrm{s}^{-1}$ in the case (a). In this case, the light-intensity dependent changes of FI pattern from O-J-I-P to O-J-D-I-P observed by Schansker et al. [71, 72] are reproduced well. In the case (b), on the other hand, the fluorescence transient pattern of J-D-I does not appear at all. These results suggest that the fluorescence transient pattern J-D-I requires the presence of $\mathrm{Y_Z^+}$ quenching in the case that the hole transfer from $\mathrm{Y_Z^+}$ to RC is neglected.

The time courses of $P_{X_{01}}$, $P_{X_4} + P_{Y_4}$, P_{Q_0} and $P_{T_1} + P_{TS_3^*}$ which are the occupancies of $\mathrm{P_{680}PheQ_A}$, $\mathrm{P_{680}^+}$, PQ and $\mathrm{Y_Z^+ + Y_Z^+S_3^*}$, respectively, are plotted with FI at $v = 15,000\,\mathrm{s}^{-1}$ in Fig. 4.10. For $P_{X_{04}} = 1$ at $t = 0$, $P_{X_{01}}$ rapidly decreases and $P_{T_1} + P_{TS_3^*}$ quickly increases up to a local maximum before the J peak appears. Then the fluorescence intensity increases, which means that the magnitude of decrease of the photochemical quenching rate $\kappa_{\mathrm{P}}^{\mathrm{o}}$ via charge separation from open RC is larger than that of increase of the $\mathrm{Y_Z^+}$-quenching rate κ_{Z}, and thus the quantum efficiency of fluorescence, $\Phi_{\mathrm{F}} \equiv \kappa_{\mathrm{F}}/(\kappa_{\mathrm{P}}^{\mathrm{o}} + \kappa_{\mathrm{P}}^{\mathrm{c}} + \kappa_{\mathrm{F}} + \kappa_{\mathrm{D}} + \kappa_{\mathrm{C}} + \kappa_{\mathrm{Q}} + \kappa_{\mathrm{Z}})$, increases. After the decreasing rate of $P_{X_{01}}$ decelerates, $P_{X_4} + P_{Y_4}$ starts decreasing and then reaches the local minimum. Thus, the peak J appears, which indicates that κ_{Z} and Φ_{F} reach

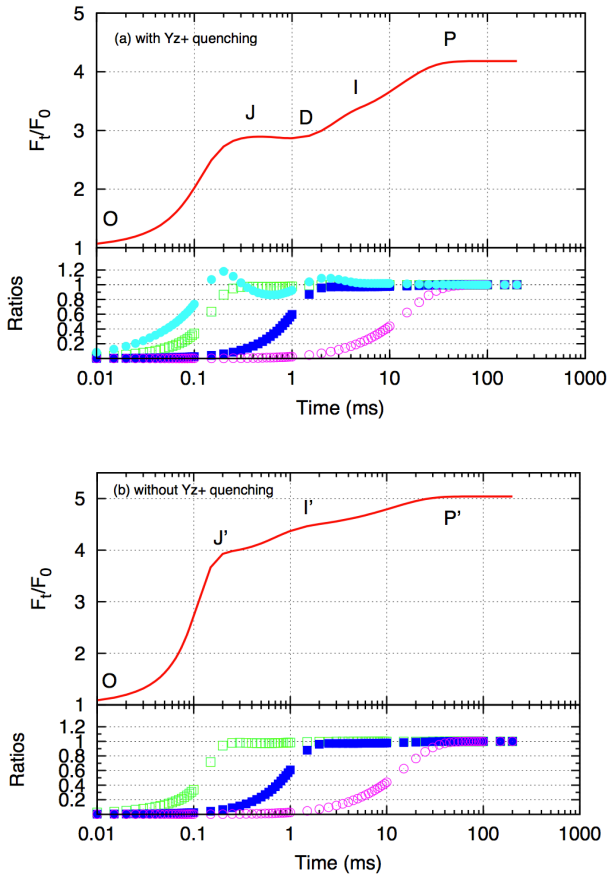

Figure 4.11 Simulated FI (upper graph) and the ratios of fluxes about electron donors/acceptors (lower graph) at $v = 15,000\,\mathrm{s}^{-1}$. The ratio of outflux to influx about each variable state: $\mathrm{Q_A^-}(Y_{04})$, $\mathrm{Q_B^{2-}}(Z_2)$, $\mathrm{PQ}(Q_0)$ and $\mathrm{Y_Z^+} + \mathrm{Y_Z^+S_3^*}(T_1 + TS_3^*)$ is defined as $V_{\mathrm{out}}^{Y_{04}}/V_{\mathrm{in}}^{Y_{04}}$ (green open square), $V_{\mathrm{out}}^{Z_2}/V_{\mathrm{in}}^{Z_2}$ (blue closed square), $V_{\mathrm{out}}^{Q_1}/V_{\mathrm{in}}^{Q_1}$ (magenta open circle) and $(V_{\mathrm{out}}^{T_1} + V_{\mathrm{out}}^{TS_3^*})/(V_{\mathrm{in}}^{T_1} + V_{\mathrm{in}}^{TS_3^*})$ (aqua closed circle), respectively. The fluorescence intensity is normalized by the value F_0 at $t = 0$. The $\mathrm{Y_Z^+}$-quenching is taken into account in the case (a) and is neglected in the case (b).

the local minimum and the local maximum, respectively. Subsequently, $P_{T_1} + P_{TS_3^*}$ continues to increase and then comes to the local maximum. At this time, κ_{Z} and Φ_{F} take the local maximum and local minimum, respectively, and the dip D appears. After that Φ_{F} increases along with the decrease of $P_{T_1} + P_{TS_3^*}$. The inflection point I of FI appears when the decreasing rate of $P_{T_1} + P_{TS_3^*}$ decelerates. Subsequently, the fluorescence intensity continues increasing under the effects of photochemical, $\mathrm{Y_Z^+}$ and PQ quenchings. The peak P appears when the PQ and all other states come to steady states. In this case based on TSTM, the value of $P_{X_4} + P_{Y_4}$ is almost zero and

does not accumulate in comparison to other states, indicating that P_{680}^{+} quenching is not effective.

To analyze the states of electron fluxes of PS II system, each ratio of outflux to influx concerning each state of electron donors/acceptors is plotted with FI at $v = 15,000\,\mathrm{s}^{-1}$ in Fig. 4.11. The Y_Z^{+} quenching is taken into account in the case (a) and neglected (i.e., $k_z = 0$) in the case (b). The ratios of outflux to influx concerning the transitions of following states, $Q_A^{-}(P_{680}PheQ_A^{-})$, Q_B^{2-}, PQ and $Y_Z^{+} + Y_Z^{+}S_3^{*}$, are indicated as $V_{\mathrm{out}}^{Y_{01}}/V_{\mathrm{in}}^{Y_{01}}$, $V_{\mathrm{out}}^{Z_2}/V_{\mathrm{in}}^{Z_2}$,$V_{\mathrm{out}}^{Q_1}/V_{\mathrm{in}}^{Q_1}$ and $(V_{\mathrm{out}}^{T_1}+V_{\mathrm{out}}^{TS_3^{*}})/(V_{\mathrm{in}}^{T_1}+V_{\mathrm{in}}^{TS_3^{*}})$, respectively. On the one hand, in the case (b), where the Y_Z^{+} quenching is neglected, it is clear that the timings at which the patterns J', I' and P' of FI appear correspond to those at which the transitions of Q_A^{-}, Q_B^{2-} and PQ states lead to quasi-steady states similarly as in Fig. 4.11(b). On the other hand, in the case (a), where the Y_Z^{+} quenching is taken into account, the FI pattern does no longer reflect clearly the timings when Q_A and Q_B have come to quasi-steady states. In this case, the peak J appears after the transition of Q_A state leads to the quasi-steady state. At the instant when the peak J appears, $(V_{\mathrm{out}}^{T_1}+V_{\mathrm{out}}^{TS_3^{*}})/(V_{\mathrm{in}}^{T_1}+V_{\mathrm{in}}^{TS_3^{*}})$ takes the value of unity with a negative gradient with respect to time. This means that the amount of $Y_Z^{+} + Y_Z^{+}S_3^{*}$ starts increasing at this time. At the instant when the dip D appears, the same ratio takes the value of unity with a positive gradient with respect to time. This indicates that the amount of $Y_Z^{+} + Y_Z^{+}S_3^{*}$ starts decreasing at this timing. The instant at which the inflection point I appears corresponds to that at which the ratio becomes stationary. This means that the transition of $Y_Z^{+} + Y_Z^{+}S_3^{*}$, i.e., the transition of states on donor side of PS II, has come to a quasi-steady state. The timing at which the peak P appears corresponds to that at which PQ has become to a steady state similarly as in the case (b).

4.4 Discussion

First, with respect to the states of RC in the coarse-grained models at millisecond scale (Eqs. (4.7a) and (4.7b), and Eqs. (4.9a) and (4.9b)) obtained through the application of the HCG method to the full PS II models, it is confirmed that the RC takes two or three variable states depending on whether the hole transfer from Y_Z^{+} to P_{680} is included or not, respectively, in the PS II model. In the former case, the variables of RC are given as quasi-conserved quantities, $[P_{680}Q_A + P_{680}^{+}Q_A]$ and $[P_{680}Q_A^{-} + P_{680}^{+}Q_A^{-}]$, where the transition between P_{680} and P_{680}^{+} is in equilibrium at both open and closed RC. In the latter case, the RC state changes between $P_{680}PheQ_A$, $P_{680}PheQ_A^{-}$ and

$P_{680}Phe^-Q_A^-$. The light-intensity dependent transition of the dominant states of RC between the pairs of ($P_{680}PheQ_A$, $P_{680}PheQ_A^-$) and ($P_{680}PheQ_A^-$, $P_{680}Phe^-Q_A^-$) is revealed on the basis of the difference between the coarse-grained models at millisecond scale for the different regimes of light intensity. This means that the dominant path towards $P_{680}PheQ_A$ state or $P_{680}Phe^-Q_A^-$ state concerning the outflux from $P_{680}PheQ_A^-$ depends on the incident light intensity. To investigate this light-dependent change of the transition pathway of RC states, the ratios of the transition flux $V_{Y_3,Y_{01}}$ from Y_{01} ($P_{680}PheQ_A^-$) to X_{01} ($P_{680}PheQ_A$), to the flux $V_{X_{01},Y_{01}}$ from Y_{01} ($P_{680}PheQ_A^-$) to Y_3 ($P_{680}Phe^-Q_A^-$) in terminal steady states at various photoexcitation rates v's for PS II are plotted in Fig. 4.12. The case (a) where the path of hole transfer from Y_Z^+ to P_{680} is included in the PS II model and the case (b) where that path is neglected in the model are shown in Fig. 4.12. The parameters for the path are set as $k_3 = 10^7\,s^{-1}$, $k_{-3} = 10^6\,s^{-1}$ in the former case and $k_3 = 5\times10^6\,s^{-1}$, $k_{-3} = 0\,s^{-1}$ in the latter case. In the case (a), if v is lower than $\sim 10^5\,s^{-1}$, $V_{Y_3,Y_{01}}/V_{X_{01},Y_{01}}$ is sufficiently small and RC takes X_{04} state or Y_{04} state, whereas if v is close to $10^7\,s^{-1}$, the ratio is close to unity and thus Y_3 state appears. In the case (b), where $V_{Y_3,Y_{01}}/V_{X_{01},Y_{01}}$ is larger than that of case (a), the ratio is close to unity at $v \sim 10^5\,s^{-1}$, whereas the pair of RC states ($P_{680}PheQ_A$, $P_{680}PheQ_A^-$) is dominant when v is smaller than $\sim 10^3\,s^{-1}$. On the other hand, the pair ($P_{680}PheQ_A^-$, $P_{680}Phe^-Q_A^-$) is dominant when v is larger than $\sim 5\times10^4\,s^{-1}$. This is in agreement with the result of coarse-graining of PS II whose coarse-grained models are different according to the photoexcitation rate ranges. At the point where the flux ratio $V_{Y_3,Y_{01}}/V_{X_{01},Y_{01}}$ is unity, the ratio of $P_{Y_{01}}$ to P_{Y_3} becomes unity. The Y_3 state is dominant when v is greater than the value of this point. Up to $v \sim 10^3\,s^{-1}$, there is no difference in the ratios of open and closed RCs at the steady states between (a) and (b). However, when v is greater than that value, there is a clear difference in the ratios of Y_3 state between (a) and (b). These results suggest that the hole transfer from Y_Z^+ to P_{680} reduces $V_{Y_3,Y_{01}}$ and suppresses the production of $P_{680}Phe^-Q_A^-$.

Second, Figs. 4.7 and 4.10 indicate that the concentration of $P_{680}PheQ_A$ gradually decreases until the peak P appears in both the DSTM and the TSTM. Especially in the TSTM, Fig. 4.7 illustrates that the ratio of $P_{680}PheQ_A^-$ state in RC at the J peak is smaller than 0.9, which is in contradiction to Vredenberg's assumption for FIA that almost all the RCs are in $P_{680}PheQ_A^-$ state at the J peak. In contrast, we have found out that the transition of Q_A is in quasi-steady state when the J peak appears (Fig. 4.11).

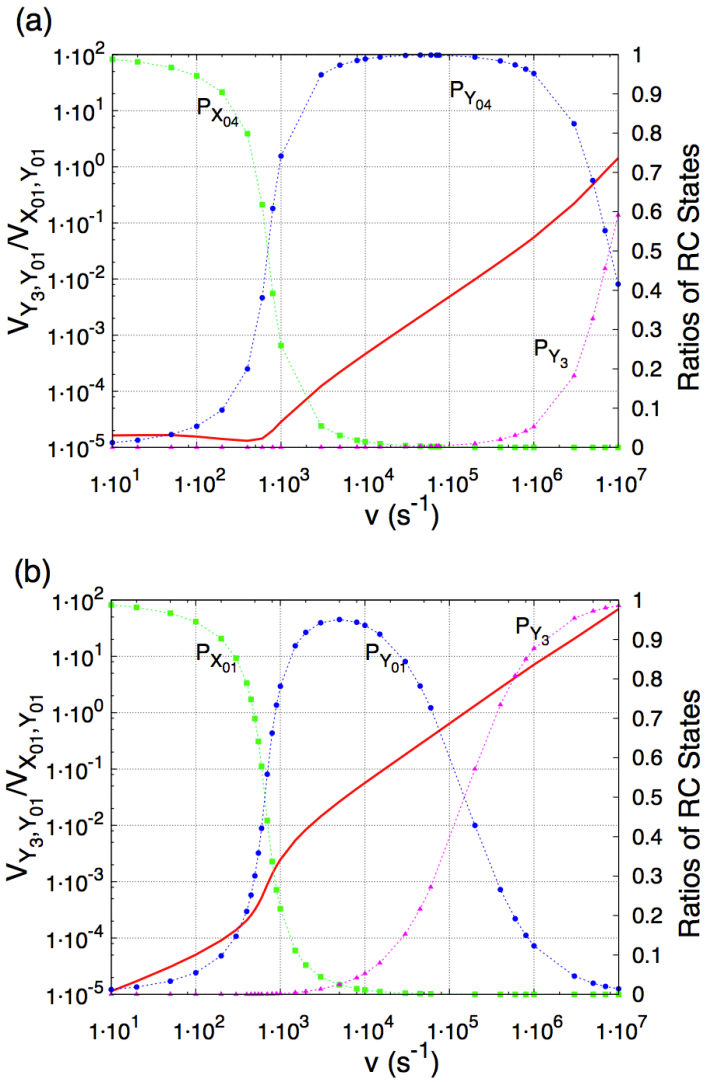

Figure 4.12 The ratio $V_{X_{01},Y_{01}}/V_{Y_3,Y_{01}}$ (red solid line, left axis) of outflux for path 1 to that for path 2 from $P_{680}PheQ_A^-$ (Y_{01} state), and the occupancy of each state in RC (right axis) at different light excitation rate v for PS II. In the case (a), where the hole transfer from Y_Z^+ to P_{680} is taken into account, $P_{X_{04}}$ and $P_{Y_{04}}$ indicate the ratios for $[P_{680}Q_A + P_{680}^+Q_A]$ and $[P_{680}Q_A^- + P_{680}^+Q_A^-]$ in the RC, respectively. In the case (b), where the hole transfer from Y_Z^+ to P_{680} is neglected, $P_{X_{01}}$ and $P_{Y_{01}}$ indicate the ratios for $P_{680}PheQ_A$ and $P_{680}PheQ_A^-$ in the RC, respectively. In both cases, P_{Y_3} indicates the ratio of $P_{680}Phe^-Q_A^-$ in the RC. All data are taken at the terminal steady states of the coarse-grained model at microsecond scale.

Third, the change of FI pattern depending on the light intensity is accounted for based on P_{680}^+ quenching in the DSTM and Y_Z^+ quenching in the TSTM. While in the TSTM the simulated FI shows a characteristic dependence on light intensity similar to that observed in experiments when the Y_Z^+-quenching rate is set as $k_z = 10^8\,s^{-1}$, this quencher is a hypothetical one and lacks the experimental verification. On the other hand, P_{680}^+ quenching mechanism, which explains the J-D-I pattern of FI in the DSTM, has experimental evidences [65].

As a result of transformation from a detailed model of PS II to a coarse-grained model, we have carve out the principal pathways at millisecond scale through the application of HCG. The process of hole transfer from Y_Z to RC is not neglected in the course of this procedure, but rather renormalized into the coarse-graining functions which guide us to the point where the processes at microsecond scale sufficiently proceed. This feature affects the coarse-grained structure of reaction network at millisecond scale and thus plays an important role for the description of the accumulation of P_{680}^+ state. For these reasons, we judge that the DSTM is a more reliable PS II model at millisecond scale than the TSTM. The assumption that the hole transfer from Y_Z to RC is negligible does not seem to be pertinent in the case that the incident light intensity is high and thus the rate of charge separation would be transiently limited by the donor-side processes of PS II. It is noted that the mathematical structure derived through the HCG method is robust for the delicate variances of parameter values. This structure does not change unless the parameters of the original full model change their orders of magnitudes.

4.5 Conclusions

The coarse-grained models of PS II at millisecond scale which correspond to an EDST-like model were systematically elucidated through the HCG method in two different cases. These models appropriately reproduce the light-intensity dependent change of FI pattern from O-J-I-P to O-J-D-I-P. In both models, the J-D-I pattern reflects the states of the donor side of PS II. On the one hand, in the case that the hole transfer from Y_Z^+ to P_{680} is accounted for in the PS II model, the J-D-I pattern is explained on the basis of P_{680}^+ quenching. On the other hand, in the case that the hole transfer process is neglected, the J-D-I pattern is explained on the basis of Y_Z^+ quenching. In the former case, the states of RC are described by two effective states. Each state is defined as the sum of P_{680}^+ and P_{680} which are in equilibrium

at microsecond scale in open RC or closed RC, respectively. The coarse-grained model in the latter case has three variable states for RC, $P_{680}PheQ_A$, $P_{680}PheQ_A^-$ and $P_{680}Phe^-Q_A^-$. These states are equivalent to the states which were assumed to be taken by RC in Vredenberg's TSTM.

These coarse-grained models obtained through the application of HCG contain the information about fast timescale processes in a renormalized way. In both the DSTM and the TSTM, the picosecond-scale processes constitute a quasi-isolated system and thus provide the quasi-conserved quantities. In the DSTM, the nanosecond-scale processes are renormalized to give the quantum efficiencies of core antenna and the rate of the indirect non-radiative recombination path from $P_{680}^+PheQ_A^-$ state. Besides, the microsecond-scale processes form the quasi-conserved quantities in this model. In TSTM, the nanosecond-scale processes are renormalized to give the quantum efficiencies of the core antenna. In particular, in the case that the photoexcitation rate v is in microsecond-scale, it is revealed that the transition path from $P_{680}PheQ_A^-$ to $P_{680}Phe^-Q_A^-$ is no longer negligible. In this case, the quantum efficiency of charge separation from closed RC, that contains the information of nanosecond-scale processes in a renormalized way, is introduced.

The present study has developed a model-based analysis of the light-intensity dependent change of transition pathways. It then suggests that the hole transfer from Y_Z^+ to P_{680} suppresses the production of over-reduced state $P_{680}Phe^-Q_A^-$ in the case that the photoexcitation rate v is about $10^4\,s^{-1}$ or higher.

We have thus found that the coarse-grained EDST-like models derived through the application of the HCG method give comprehensive descriptions with respect to the dynamic properties of PS II at timescales of interest. It is remarkable that the mathematical coarse-graining procedures naturally provide those physicochemical pictures that are consistent with biological observations.

Chapter 5

Coarse-Graining of the Model for Photosynthetic Processes of PS I

5.1 Introduction

Photosystem I (PS I) is one of the most important protein complex of photosynthesis as well as PS II. The redox potential (energy level) of electron transferred from H_2O is elevated by these two photosystems and then the electron obtains the reduction power high enough to reduce $NADP^+$ (nicotinamide adenine dinucleotide phosphate). Meanwhile, other electron transfer steps dissipate the excitation energy, hence the energy diagram of electron transfer steps on thylakoid membrane has a zig-zag feature called "Z-scheme" [23]. The dynamics of electron transfer in PS I is observed by means of I_{820} signal, which reflects the accumulations of P^+_{700} and oxidized Pc [94, 95]. The major peak of the fluorescence emitted from PS I at room temperature is observed at 725nm [96, 97]. Therefore, its contribution to the Chl *a* fluorescence characterized by a band peak at 685nm, which is discussed in Chapter 3, is regarded to be small.

The electron transport system in PS I is supposed to possess regulation mechanisms. The charge recombination process is suggested to work for regulation of electron transfer when electrons are congested in PS I. The congestion of electrons in PS I occurs in the induction time. The dynamics of the electron transport system in PS I is reflected by the characteristic time course profile of the I_{820} signal. However, the analysis of this time course pattern is difficult because the reaction model used for analysis is too complex to comprehensively understand the phenomena on the basis of the model. The reaction network of electron transfer in PS I is not only complicated but also temporally multiscale as in PS II. In this chapter, a kinetic model

of excitation-energy transfer and electron transfer for PS I is treated. If one deals with all the possible combinations of the states of N electron carriers which take oxidized or reduced states, the dimension of the state space of electron carriers is equal to 2^N. This dimensionality can be reduced by extracting the principal reaction network by means of the multiscale property of the original reaction model. In this way, I attempt to understand the induction phenomena of PS I based on the simple and mono-scale model extracted from the complex and multiscale model. The hierarchical coarse-graining in time of the kinetic model of PS I at picosecond, nanosecond, microsecond and millisecond scales are attempted below.

5.2 Models and Methods

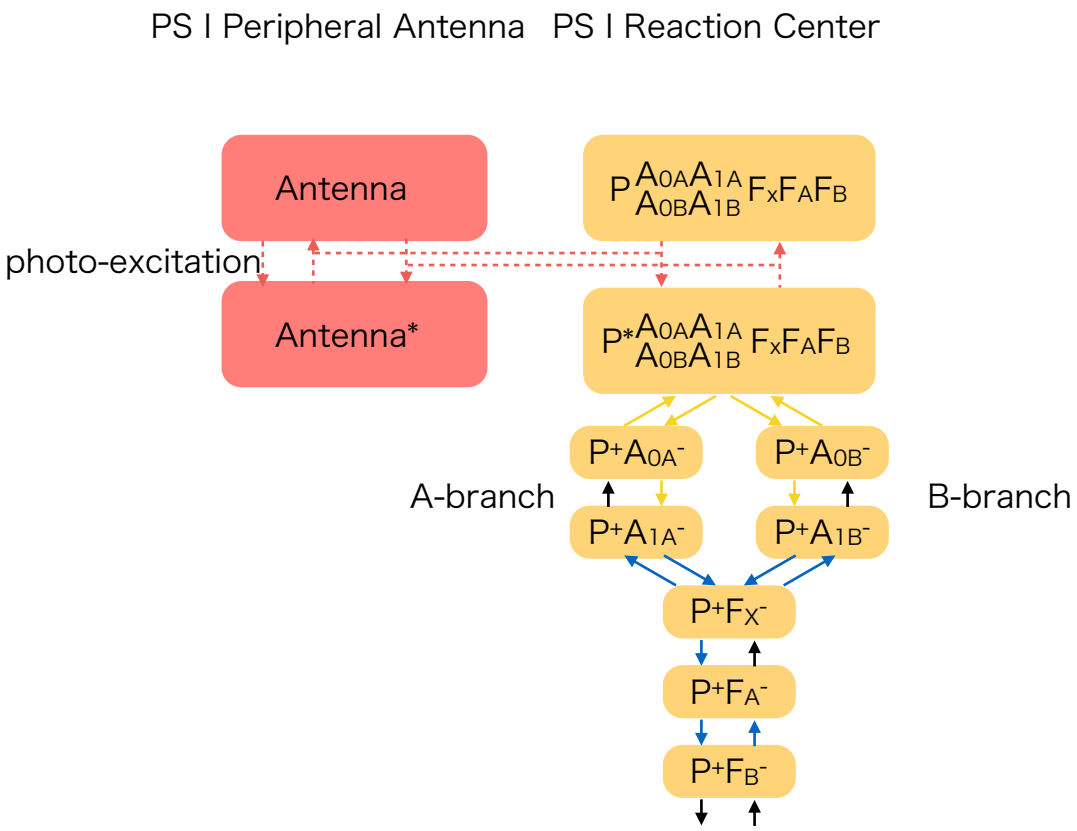

Figure 5.1 Schematic diagram of excitation-energy and electron transfer processes following a single excitation in PS I. Solid and dashed lines indicate the electron transfer and the excitation-energy transfer, respectively. Each color indicates different time-scales as follows. Red: picoseconds, yellow: nanoseconds, blue: microseconds, black: milliseconds. Each RC, except for the ground and the excited states, is characterized by the reduced site.

5.2.1 Kinetic model of PS I

First, the reaction network of electron transfer in PS I following the single excitation is studied as a simple case [98]. The diagram of this reaction including picosecond to microsecond scales is illustrated in Fig. 5.1. PS I has a heterodimeric reaction center

that consists of the two near-symmetrical electron transfer branches, A-branch and B-branch. Though the amino-acid identity of these branches is about 60 % and thus there are some functional differences, the probabilities of the occurrences of charge separation are nearly equal in both branches [99]. The kinetic model of this reaction is expressed with the use of the ODEs (Eq. (5.2) below). The notations are assigned to the variables as follows:

$$\begin{aligned} &WI_1 : [antenna^*]; WI_0 : [antenna]; XI_1 : [\mathrm{P}^*]; \\ &XI_{2A} : [\mathrm{P}^+\mathrm{A}^-_{0\mathrm{A}}]; XI_{2B} : [\mathrm{P}^+\mathrm{A}^-_{0\mathrm{B}}]; \\ &XI_{3A} : [\mathrm{P}^+\mathrm{A}^-_{1\mathrm{A}}]; XI_{3B} : [\mathrm{P}^+\mathrm{A}^-_{1\mathrm{B}}]; \\ &XI_4 : [\mathrm{P}^+\mathrm{F}^-_{\mathrm{X}}]; XI_5 : [\mathrm{P}^+\mathrm{F}^-_{\mathrm{A}}]; XI_6 : [\mathrm{P}^+\mathrm{F}^-_{\mathrm{B}}], \end{aligned} \tag{5.1}$$

where [ ] means the concentration. P is the primary donor, P_{700}. Both $\mathrm{A}_{0\mathrm{A}}$ and $\mathrm{A}_{0\mathrm{B}}$ are Chl *a* molecules that are the first electron acceptors of path A and path B, respectively. $\mathrm{A}_{1\mathrm{A}}$ and $\mathrm{A}_{1\mathrm{B}}$ are phylloquinone molecules that are the next electron acceptors of path A and path B, respectively. The electron transfer reactions proceed over the ion-sulfur clusters, F_{X}, F_{A} and F_{B} in turn. The rate constants are shown in Table 5.1.

$$\begin{cases} \frac{\mathrm{d}WI_1}{\mathrm{d}t} &= V\frac{WI_0}{WI_T} - k_{\mathrm{d}}WI_1 - k_{\mathrm{p}+}\frac{XI_T-XI_0-XI_1}{XI_T}WI_1 - k_0WI_1\frac{XI_0}{XI_T} + k_{-0}\frac{WI_0}{WI_T}XI_1, \\ \frac{\mathrm{d}XI_0}{\mathrm{d}t} &= -k_0WI_1\frac{XI_0}{XI_T} + k_{-0}\frac{WI_0}{WI_T}XI_1 + k_dXI_1, \\ \frac{\mathrm{d}XI_1}{\mathrm{d}t} &= k_0WI_1\frac{XI_0}{XI_T} - k_{-0}\frac{WI_0}{WI_T}XI_1 - k_dXI_1 - k_{\mathrm{p}+}\frac{XI_T-XI_0-XI_1}{XI_T}XI_1 \\ &\quad -(k_1+k_{10})XI_1 + k_{-1}XI_{2A} + k_{-10}XI_{2B}, \\ \frac{\mathrm{d}XI_{2A}}{\mathrm{d}t} &= k_1XI_1 - (k_2+k_{-1})XI_{2A}, \\ \frac{\mathrm{d}XI_{2B}}{\mathrm{d}t} &= k_{10}XI_1 - (k_{20}+k_{-10})XI_{2B}, \\ \frac{\mathrm{d}XI_{3A}}{\mathrm{d}t} &= k_2XI_{2A} - k_3XI_{3A} + k_{-3}XI_4, \\ \frac{\mathrm{d}XI_{3B}}{\mathrm{d}t} &= k_{20}XI_{2B} - k_{30}XI_{3B} + k_{-30}XI_4, \\ \frac{\mathrm{d}XI_4}{\mathrm{d}t} &= k_3XI_{3A} + k_{30}XI_{3B} - (k_{-3}+k_{-30}+k_4)XI_4 + k_{-4}XI_5, \\ \frac{\mathrm{d}XI_5}{\mathrm{d}t} &= k_4XI_4 - k_{-4}XI_5 - k_{AB}XI_5 + k_{-AB}XI_6, \\ \frac{\mathrm{d}XI_6}{\mathrm{d}t} &= k_{AB}XI_5 - k_{-AB}XI_6. \end{cases} \tag{5.2}$$

Thus one should consider only nine states of RC for the reaction up to microsecond scale when the reaction is induced by the single excitation. However, under continuous light irradiation such as sun light, over-reduced states that have more than two electron charges are realized in RC. This means that a number of states should be taken into account under continuous light.

The principal reaction pathway can be extracted with the use of the hierarchical property of the timescale of the reaction network. In this treatment, each variable state is assumed to change by the reactions whose timescales belong to the most and secondly fast classes among the reactions related to each variable state. The reaction network diagram extracted by this assumption is illustrated in Fig. 5.2. A kinetic model of the reaction network of PSI-RC under continuous light can be constructed based on this figure along with Eq. (5.2). The over-reduced states of RC are represented by the combinations of the notations defined in Eq. (5.1). For example, XI_{654} : $[\mathrm{P}^{+}\mathrm{F}_{\mathrm{X}}^{-}\mathrm{F}_{\mathrm{A}}^{-}\mathrm{F}_{\mathrm{B}}^{-}]$; XI_{650} : $[\mathrm{PF}_{\mathrm{A}}^{-}\mathrm{F}_{\mathrm{B}}^{-}]$; XI_{62B} : $[\mathrm{P}^{+}\mathrm{A}_{0\mathrm{B}}^{-}\mathrm{F}_{\mathrm{B}}^{-}]$; XI_{51} : $[\mathrm{P}^{*}\mathrm{F}_{\mathrm{A}}^{-}]$, and so on. Here, the notations 0 and 1 correspond to the ground state and the excited state of the primary donor P_{700}, respectively. Besides, the notations $2A$, $2B$, ..., 5 and 6 represent that the corresponding pigments indicated in Eq. (5.1) are reduced. In addition to Eq. (5.1), XI_7 : $[\mathrm{P}^{+}]$ is introduced for the RC state where the P_{700} is oxidized and other sites are neutral.

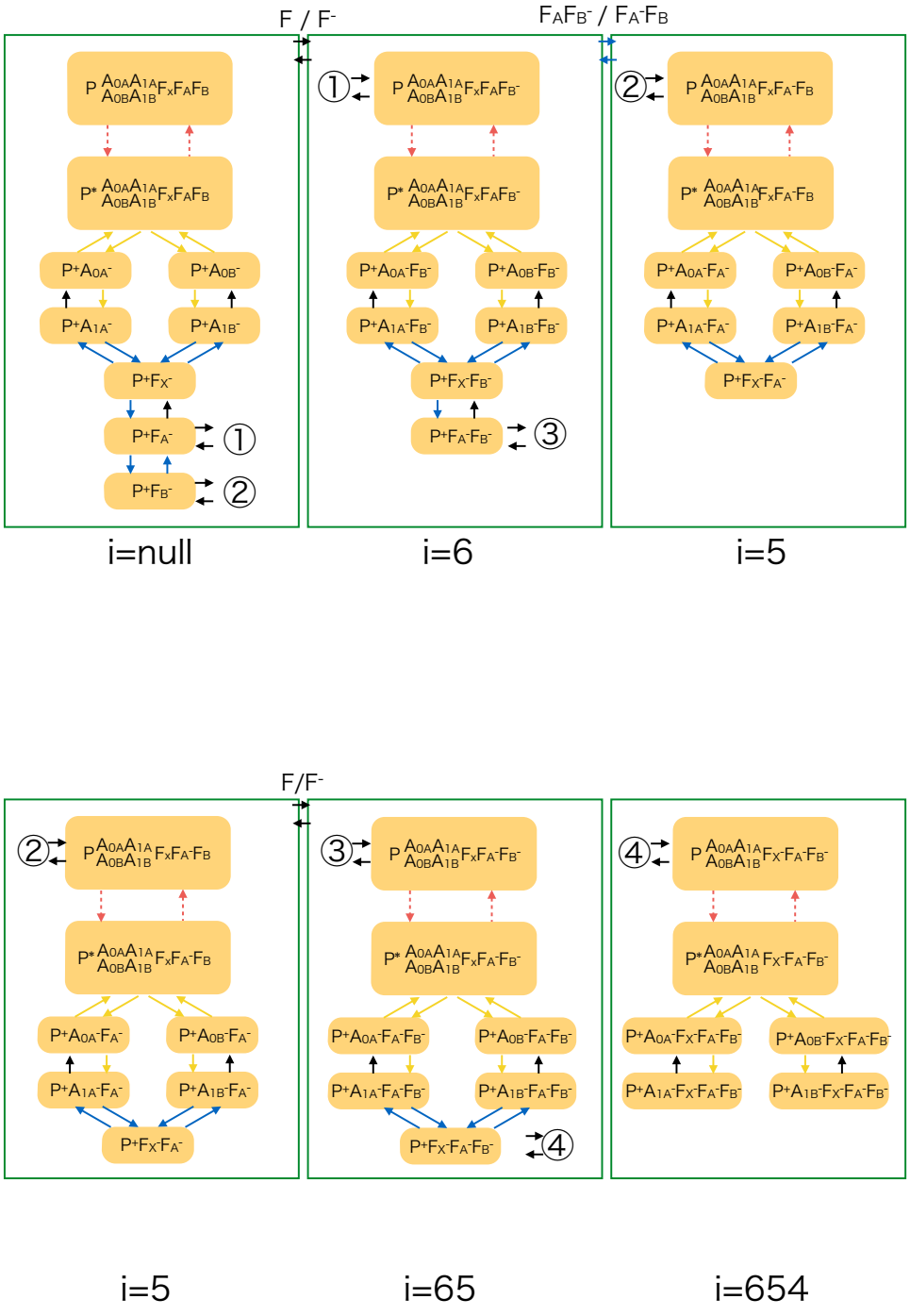

Figure 5.2 Reduced diagrams of PSI-RC reaction network. Each number enclosed within a circle indicates the reaction coupled with redox reaction of Pc. The meanings of types and colors of arrows are the same as Fig. 5.1. The states which share the same reduced sites are classified by the green boxes characterized by the index i. The index i = 5, 6, 65 and 654 correspond to the F_A^-, F_B^-, $F_A^-F_B^-$ and $F_X^-F_A^-F_B^-$ states, respectively.

5.2.2 Coarse-graining treatment

Hereafter, coarse-graining treatment is applied to the kinetic model based on Fig. 5.2. According to the HCG method proposed in Chapter 2, the dimensionless times should be introduced. In this chapter, the dimensionless times are introduced by means of the characteristic rate constants of the kinetic model as below:

$$\begin{aligned} \tau_{\mathrm{I}} &\equiv k_0 t, \\ \tau_{\mathrm{II}} &\equiv k_2 t, \\ \tau_{\mathrm{III}} &\equiv k_4 t, \\ \tau_{\mathrm{IV}} &\equiv k_{bf} t. \end{aligned} \tag{5.3}$$

The timescale ratios are introduced as $\varepsilon_{\mathrm{I,II}} = k_2/k_0$, $\varepsilon_{\mathrm{II,III}} = k_4/k_2$, $\varepsilon_{\mathrm{III,IV}} = k_{bf}/k_4$ and $\varepsilon_{\mathrm{II,IV}} = k_{bf}/k_2$. The rate constants of the model are enumerated in Table 5.1.

The ODEs with the dimensionless time τ_{I} scaled by the picosecond-scale rate constant is expressed as

$$\begin{cases} \frac{\mathrm{d}WI_1}{\mathrm{d}\tau_{\mathrm{I}}} & = \varepsilon_{\mathrm{I,II}}\nu\frac{WI_0}{WI_T} - \varepsilon_{\mathrm{I,II}}\kappa_{\mathrm{d}}WI_1 - \varepsilon_{\mathrm{I,II}}\kappa_{\mathrm{p}+}\frac{XI_T - XI_0 - XI_1}{XI_T}WI_1 \\ & \quad -\kappa_0 WI_1\frac{\sum_i XI_{i0}}{XI_T} + \kappa_{-0}\sum_i \frac{WI_0}{WI_T}XI_{i1}, \\ \frac{\mathrm{d}XI_{i1}}{\mathrm{d}\tau_{\mathrm{I}}} & = \kappa_0 WI_1\frac{XI_{i0}}{XI_T} - \kappa_{-0}\frac{WI_0}{WI_T}XI_{i1} - \varepsilon_{\mathrm{I,II}}\kappa_d XI_{i1} - \varepsilon_{\mathrm{I,II}}\kappa_{\mathrm{p}+}\frac{XI_T - XI_0 - XI_1}{XI_T}XI_{i1} \\ & \quad -\varepsilon_{\mathrm{I,II}}(\kappa_1 + \kappa_{10})XI_{i1} + \varepsilon_{\mathrm{I,II}}\kappa_{-1}XI_{i2A} + \varepsilon_{\mathrm{I,II}}\kappa_{-10}XI_{i2B}, \end{cases} \tag{5.4}$$

where $i = null$, 5, 6, 65 and 654. At picosecond scale, the quasi-conserved quantities that only change with $O(\varepsilon_{\mathrm{I,II}})$ rates exist: $UI_1 = WI_1 + \sum_i XI_{i1}$ and $XI_{i01} = XI_{i0} + XI_{i1}$. The asymptotic behaviors of WI_1 and XI_{i1}'s can be described by the slower variables by means of quasi-equilibrium pseudo-steady-state approximation, $\lim_{\tau_{\mathrm{I}}\to\infty}\mathrm{d}WI_1/\mathrm{d}\tau_{\mathrm{I}} = 0$ and $\lim_{\tau_{\mathrm{I}}\to\infty}\mathrm{d}XI_{i1}/\mathrm{d}\tau_{\mathrm{I}} = 0$:

$$\begin{aligned} \lim_{\tau_{\mathrm{I}}\to\infty} WI_1(\tau_{\mathrm{I}}) &= \frac{\kappa_{-0}XI_T}{\kappa_{-0}XI_T + \kappa_0\sum_i XI_{i0}}UI_1, \\ \lim_{\tau_{\mathrm{I}}\to\infty} XI_{i1}(\tau_{\mathrm{I}}) &= \frac{\kappa_0 XI_{i0}}{\kappa_{-0}XI_T + \kappa_0\sum_i XI_{i0}}UI_1 \\ &\equiv p(XI_{i1} \mid UI_1)UI_1. \end{aligned} \tag{5.5}$$

Here, the occupancy ratios of the exciton at RCs, $XI_{i1}(i = null,\ 5,\ 6,\ 65,\ 654)$, to the total exciton at PS I, UI_1, are introduced as $p(XI_{i1} \mid UI_1) = \kappa_0 XI_{i0}/(\kappa_{-0}XI_T + \kappa_0\sum_i XI_{i0})$.

Table 5.1 Parameter List of PS I Model

Description	Notation	Value (Time-scale class)	Reference
Rate constant of excitation transfer from LHA to special pair	k_0	-(A_{I})	Implicit
Rate constant of excitation transfer from special pair to LHA	k_{-0}	- (A_{I})	Implicit
Rate constant of excitation dissipation from antenna	k_{d}	$5 \times 10^8\,\mathrm{s}^{-1}$ (A_{II})	[98]
Rate constant of charge separation at branch A	k_1	$10^{11}\,\mathrm{s}^{-1}$ (A_{II})	[98]
Rate constant of charge separation at branch A	k_{10}	$10^{11}\,\mathrm{s}^{-1}$ (A_{II})	[98]
Rate constant of charge recombination at branch A	k_{-1}	$8.3 \times 10^9\,\mathrm{s}^{-1}$ (A_{II})	[98]
Rate constant of charge recombination at branch B	k_{-10}	$8.3 \times 10^9\,\mathrm{s}^{-1}$ (A_{II})	[98]
Rate constant of electron transfer from A_{0A} to A_{1A}	k_2	$2.6 \times 10^{10}\,\mathrm{s}^{-1}$ (A_{II})	[98]
Rate constant of electron transfer from A_{0B} to A_{1B}	k_{20}	$4.8 \times 10^{10}\,\mathrm{s}^{-1}$ (A_{II})	[98]
Rate constant of electron transfer from A_{1A} to F_X	k_3	$4.6 \times 10^7\,\mathrm{s}^{-1}$ (A_{III})	[98]
Rate constant of electron transfer from A_{1B} to F_X	k_{30}	$8.2 \times 10^7\,\mathrm{s}^{-1}$ (A_{III})	[98]
Rate constant of electron transfer from F_X to A_{1A}	k_{-3}	$8.4 \times 10^7\,\mathrm{s}^{-1}$ (A_{III})	[98]
Rate constant of electron transfer from F_X to F_A	k_4	$2.1 \times 10^7\,\mathrm{s}^{-1}$ (A_{III})	[98]
Rate constant of electron transfer from F_A ot F_X	k_{-4}	$4.7 \times 10^4\,\mathrm{s}^{-1}$ (A_{IV})	[98]
Rate constant of electron transfer from F_A to F_B	k_{AB}	$3.5 \times 10^6\,\mathrm{s}^{-1}$ (A_{III})	[98]
Rate constant of electron transfer from F_B to F_B	k_{-AB}	$1.1 \times 10^6\,\mathrm{s}^{-1}$ (A_{III})	[98]
Rate constant of $P700^+$ quenching of antenna	$k_{\mathrm{p+}}$	$2 \times 10^9\,\mathrm{s}^{-1}$ (A_{II})	[60]
Rate constant of non-radiative recombination from $P^+A_{1A}^-$ and $P^+A_{1B}^-$	$k_{1\mathrm{P}}$	$10^5\,\mathrm{s}^{-1}$ (A_{IV})	[60]

(To be continued)

(Continued)

Rate constant of electron transfer from F_B to F	k_{BF}	$3.25 \times 10^3\,s^{-1}$ (A_{III})	[60]
Rate constant of electron transfer from F^- F_B	k_{-BF}	$3.25 \times 10^3\,s^{-1}$ (A_{III})	[60]
Rate constant of electron transfer from F to active FNR	k_{FFNR}	$580\,s^{-1}$(A_{II})	[78]
Rate constant of electron transfer from reduced FNR, FNR^- or FNR^{2-}, to F	k_{-FFNR}	$580 s^{-1}$ (A_{IV})	[78]
Rate constant for the activation of inactive FNR (FNRi)	k_{FNRA}	$0.01\,s^{-1}$ (A_{IV})	[78]
Rate constant for the oxidation of FNR^{2-} back to active FNR	k_{FNR}	$220\,s^{-1}$ (A_{IV})	[78]
Rate constant of electron transport from reduced Pc to P_{700}^+	k_{PcP}	$110\,s^{-1}$ (A_{IV})	[78]
Rate constant of electron transport from P_{700} to Pc^+	k_{-PcP}	$110\,s^{-1}$ (A_{IV})	[78]
Rate constant for the reduction of Pc^+ by electrons come from PS II	k_{Pc}	$100\,s^{-1}$ (A_{IV})	[78]
Radiation flux density to PS I	V	(A_{IV})	
Concentration of all PS I reaction center's states (conserved quantity)	XI_T	-	-
Concentration of total states of ferredoxin (conserved quantity)	YI_T	-	-
Concentration of total states of FNR (conserved quantity)	ZI_T	-	-
Concentration of Pc in thylakoid lumen (conserved quantity)	C_T	-	-
Concentration of total pigments in core antenna (conserved quantity)	WI_T	-	-

Next, the coarse-graining of the processes at nanosecond scale is considered. The ODEs with dimensionless time τ_{II} are expressed by means of Eq. (5.5) for $i = null$, 5, 6, 65 and 654:

$$\begin{cases} \frac{dUI_1}{d\tau_{II}} & = \varepsilon_{II,IV}\nu\frac{WI_0}{WI_T} - \kappa_d UI_1 - \kappa_{p+}\frac{XI_T - \sum_i XI_{i01}}{XI_T}UI_1 \\ & +(\kappa_1 + \kappa_{10})\sum_i p(XI_{i1} \mid UI_1)UI_1, \\ \frac{dXI_{i2A}}{d\tau_{II}} & = \kappa_1 p(XI_{i1} \mid UI_1)UI_1 - (\kappa_2 + \kappa_{-1})XI_{i2A}, \\ \frac{dXI_{i2B}}{d\tau_{II}} & = \kappa_{10}\Gamma_{XI_{i1}} - (\kappa_{20} + \kappa_{-10})XI_{i2B}. \end{cases} \tag{5.6}$$

The coarse-graining functions are given through the non-equilibrium pseudo-steady-state approximation, $\lim_{\tau_{II}\to\infty} dUI_1/d\tau_{II} = 0$, $\lim_{\tau_{II}\to\infty} dXI_{i2A}/d\tau_{II} = 0$ and

$\lim_{\tau_{\mathrm{II}}\to\infty} \mathrm{d}XI_{i2B}/\mathrm{d}\tau_{\mathrm{II}} = 0$:

$$\begin{aligned}
\lim_{\tau_{\mathrm{II}}\to\infty} UI_1(\tau_{\mathrm{II}}) &= \frac{\varepsilon_{\mathrm{II,IV}}\nu}{\kappa_d + \kappa_{\mathrm{p}+}\frac{XI_T - \sum_i XI_{i01}}{XI_T} + (\kappa_1\gamma^f_{XI_{i2A}} + \kappa_{10}\gamma^f_{XI_{i2B}})\sum_i p(XI_{i1} \mid UI_1)} \\
&\equiv \varepsilon_{\mathrm{II,IV}}\Gamma_{UI_1}, \\
\lim_{\tau_{\mathrm{II}}\to\infty} XI_{i2A}(\tau_{\mathrm{II}}) &= \varepsilon_{\mathrm{II,IV}}\frac{\kappa_1}{\kappa_2 + \kappa_{-1}}\Gamma_{XI_{i1}} \\
&\equiv \varepsilon_{\mathrm{II,IV}}\Gamma_{XI_{i2A}}, \\
\lim_{\tau_{\mathrm{II}}\to\infty} XI_{i2B}(\tau_{\mathrm{II}}) &= \varepsilon_{\mathrm{II,IV}}\frac{\kappa_{10}}{\kappa_{20} + \kappa_{-10}}\Gamma_{XI_{i1}} \\
&\equiv \varepsilon_{\mathrm{II,IV}}\Gamma_{XI_{i2B}}.
\end{aligned} \tag{5.7}$$

Here, the coarse-graining parameters, $\gamma^f_{XI_{2A}} = \kappa_2/(\kappa_2+\kappa_{-1})$ and $\gamma^f_{XI_{2B}} = \kappa_{20}/(\kappa_{20}+\kappa_{-10})$, meaning the ratios of forward reaction flux rates to the total flux rate from XI_{2A} and XI_{2B}, respectively, are introduced. Besides, the coarse-graining functions of the excited RCs, $\lim_{\tau_{\mathrm{II}}\to\infty} XI_{i1} \equiv p(XI_{i1} \mid UI_1)\Gamma_{UI_1}$ for $i = null$, 5, 6, 65 and 654, are introduced.

The processes at microsecond scale are coarse-grained in the following. The kinetic models at this scale are different among $i = null$, 5, 6, 65 and 654. The ODEs with the dimensionless time τ_{III} are shown as below.

The case of $i = null$:

$$\begin{cases}
\frac{\mathrm{d}XI_{3A}}{\mathrm{d}\tau_{\mathrm{III}}} &= \kappa_2\varepsilon_{\mathrm{III,IV}}\Gamma_{XI_{2A}} - (\kappa_3 + \kappa_{1P})XI_{3A} + \kappa_{-3}XI_4, \\
\frac{\mathrm{d}XI_{3B}}{\mathrm{d}\tau_{\mathrm{III}}} &= \kappa_{20}\varepsilon_{\mathrm{III,IV}}\Gamma_{XI_{2B}} - (\kappa_{30} + \kappa_{1P})XI_{3B} + \kappa_{-30}XI_4, \\
\frac{\mathrm{d}XI_4}{\mathrm{d}\tau_{\mathrm{III}}} &= \kappa_3 XI_{3A} + \kappa_{30}XI_{3B} - (\kappa_4 + \kappa_{-3} + \kappa_{-30})XI_4 + \varepsilon_{\mathrm{III,IV}}\kappa_{-4}XI_5, \\
\frac{\mathrm{d}XI_5}{\mathrm{d}\tau_{\mathrm{III}}} &= \kappa_4 XI_4 - \varepsilon_{\mathrm{III,IV}}\kappa_{-4}XI_5 - \kappa_{AB}XI_5 + \kappa_{-AB}XI_6, \\
\frac{\mathrm{d}XI_6}{\mathrm{d}\tau_{\mathrm{III}}} &= \kappa_{AB}XI_5 - \kappa_{-AB}XI_6 - \varepsilon_{\mathrm{III,IV}}(\kappa_{BF}XI_6YI_0 - \kappa_{-BF}XI_7YI_1).
\end{cases} \tag{5.8}$$

The case of $i = 5$, 6:

$$
\begin{cases}
\frac{\mathrm{d}XI_{60}}{\mathrm{d}\tau_{\mathrm{III}}} & = \kappa_{AB}XI_{50} - \kappa_{-AB}XI_{60}, \\
\frac{\mathrm{d}XI_{63A}}{\mathrm{d}\tau_{\mathrm{III}}} & = \kappa_2\varepsilon_{\mathrm{III,IV}}\Gamma_{XI_{62A}} - (\kappa_3+\kappa_{1P})XI_{63A} + \kappa_{-3}XI_{64} + \kappa_{AB}XI_{53A} - \kappa_{-AB}XI_{63A}, \\
\frac{\mathrm{d}XI_{63B}}{\mathrm{d}\tau_{\mathrm{III}}} & = \kappa_{20}\varepsilon_{\mathrm{III,IV}}\Gamma_{XI_{62B}} - (\kappa_{30}+\kappa_{1P})XI_{63B} + \kappa_{-30}XI_{64} + \kappa_{AB}XI_{53B} - \kappa_{-AB}XI_{63B}, \\
\frac{\mathrm{d}XI_{64}}{\mathrm{d}\tau_{\mathrm{III}}} & = \kappa_3XI_{63A} + \kappa_{30}XI_{63B} - (\kappa_4+\kappa_{-3}+\kappa_{-30})XI_{64} + \varepsilon_{\mathrm{III,IV}}\kappa_{-4}XI_{65} \\
& \quad +\kappa_{AB}XI_{54} - \kappa_{-AB}XI_{64}, \\
\frac{\mathrm{d}XI_{65}}{\mathrm{d}\tau_{\mathrm{III}}} & = \kappa_4XI_{64} - \varepsilon_{\mathrm{III,IV}}\kappa_{-4}XI_{65}, \\
\frac{\mathrm{d}XI_{50}}{\mathrm{d}\tau_{\mathrm{III}}} & = -\kappa_{AB}XI_{50} + \kappa_{-AB}XI_{60}, \\
\frac{\mathrm{d}XI_{53A}}{\mathrm{d}\tau_{\mathrm{III}}} & = \kappa_2\varepsilon_{\mathrm{III,IV}}\Gamma_{XI_{52A}} - (\kappa_3+\kappa_{1P})XI_{53A} + \kappa_{-3}XI_{54} - \kappa_{AB}XI_{53A} + \kappa_{-AB}XI_{63A}, \\
\frac{\mathrm{d}XI_{53B}}{\mathrm{d}\tau_{\mathrm{III}}} & = \kappa_{20}\varepsilon_{\mathrm{III,IV}}\Gamma_{XI_{52B}} - (\kappa_{30}+\kappa_{1P})XI_{53B} + \kappa_{-30}XI_{54} - \kappa_{AB}XI_{53B} + \kappa_{-AB}XI_{63B}, \\
\frac{\mathrm{d}XI_{54}}{\mathrm{d}\tau_{\mathrm{III}}} & = \kappa_3XI_{53A} + \kappa_{30}XI_{53B} - (\kappa_4+\kappa_{-3}+\kappa_{-30})XI_{54} - \kappa_{AB}XI_{54} + \kappa_{-AB}XI_{64}.
\end{cases}
\tag{5.9}
$$

The case of $i = 65$:

$$
\begin{cases}
\frac{\mathrm{d}XI_{653A}}{\mathrm{d}\tau_{\mathrm{III}}} & = \kappa_2\varepsilon_{\mathrm{III,IV}}\Gamma_{XI_{652A}} - (\kappa_3+\kappa_{1P})XI_{653A} + \kappa_{-3}XI_{654}, \\
\frac{\mathrm{d}XI_{653B}}{\mathrm{d}\tau_{\mathrm{III}}} & = \kappa_{20}\varepsilon_{\mathrm{III,IV}}\Gamma_{XI_{652B}} - (\kappa_{30}+\kappa_{1P})XI_{653B} + \kappa_{-30}XI_{654}, \\
\frac{\mathrm{d}XI_{654}}{\mathrm{d}\tau_{\mathrm{III}}} & = \kappa_3XI_{653A} + \kappa_{30}XI_{653B} - (\kappa_{-3}+\kappa_{-30})XI_{654}.
\end{cases}
\tag{5.10}
$$

The case of $i = 654$:

$$
\begin{cases}
\frac{\mathrm{d}XI_{6543A}}{\mathrm{d}\tau_{\mathrm{III}}} & = \kappa_2\varepsilon_{\mathrm{III,IV}}\Gamma_{XI_{6542A}} - (\kappa_3+\kappa_{1P})XI_{6543A}, \\
\frac{\mathrm{d}XI_{6543B}}{\mathrm{d}\tau_{\mathrm{III}}} & = \kappa_{20}\varepsilon_{\mathrm{III,IV}}\Gamma_{XI_{6542B}} - (\kappa_{30}+\kappa_{1P})XI_{6543B}.
\end{cases}
\tag{5.11}
$$

The coarse-graining functions of the XI_{i3A}, XI_{i3B} and XI_{i4} for $i = null$, 5, 6, 65 and 654 are derived through the nonequilibrium pseudo-steady-state approximation, $\lim_{\tau_{\mathrm{II}}\to\infty}\mathrm{d}XI_{i3A}/\mathrm{d}\tau_{\mathrm{II}} = 0$, $\lim_{\tau_{\mathrm{II}}\to\infty}\mathrm{d}XI_{i3B}/\mathrm{d}\tau_{\mathrm{II}} = 0$ and $\lim_{\tau_{\mathrm{II}}\to\infty}\mathrm{d}XI_{i4}/\mathrm{d}\tau_{\mathrm{II}} = 0$. In the case of $i = null$, the coarse-graining functions are expressed as below:

$$
\begin{aligned}
\lim_{\tau_{\mathrm{III}}\to\infty} XI_4(\tau_{\mathrm{III}}) &= \varepsilon_{\mathrm{III,IV}}\frac{\kappa_2\gamma^f_{XI_{3A}}\Gamma_{XI_{2A}} + \gamma^f_{XI_{3B}}\kappa_{20}\Gamma_{XI_{2B}} + \kappa_{-4}XI_5}{\kappa_4 + \kappa_{-3}\gamma^d_{XI_{3A}} + \kappa_{-30}\gamma^d_{XI_{3B}}} \\
&\equiv \varepsilon_{\mathrm{III,IV}}\Gamma_{XI_4}, \\
\lim_{\tau_{\mathrm{III}}\to\infty} XI_{3A}(\tau_{\mathrm{III}}) &= \frac{\varepsilon_{\mathrm{III,IV}}}{\kappa_3+\kappa_{1P}}[\kappa_2\Gamma_{XI_{2A}} + \kappa_{-3}\Gamma_{XI_4}] \equiv \varepsilon_{\mathrm{III,IV}}\Gamma_{XI_{3A}}, \\
\lim_{\tau_{\mathrm{III}}\to\infty} XI_{3B}(\tau_{\mathrm{III}}) &= \frac{\varepsilon_{\mathrm{III,IV}}}{\kappa_{30}+\kappa_{1P}}[\kappa_{20}\Gamma_{XI_{2B}} + \kappa_{-30}\Gamma_{XI_4}] \equiv \varepsilon_{\mathrm{III,IV}}\Gamma_{XI_{3B}},
\end{aligned}
\tag{5.12}
$$

with $\gamma^f_{XI_{3A}} = \kappa_3/(\kappa_3+\kappa_{1P})$, $\gamma^f_{XI_{3B}} = \kappa_{30}/(\kappa_{30}+\kappa_{1P})$, $\gamma^d_{XI_{3A}} = \kappa_{1P}/(\kappa_3+\kappa_{1P})$ and $\gamma^d_{XI_{3B}} = \kappa_{1P}/(\kappa_{30}+\kappa_{1P})$. For the case of $i = 5$, 6, 65 and 654, see Appendix C.1.

By substituting these results to Eqs. (5.8) - (5.11), it is revealed in the case $i = null$ that there is the quasi-conserved quantity, $XI_{5/6} \equiv XI_5 + XI_6$, that changes only with $\mathrm{O}(\varepsilon_{\mathrm{III,IV}})$ rates at this time scale.

The coarse-graining functions Eq. (5.13) are derived by applying the quasi-equilibrium pseudo-steady-state approximation, $\lim_{\tau_{\mathrm{III}}\to\infty} \mathrm{d}XI_5/\mathrm{d}\tau_{\mathrm{III}} = -\kappa_{AB}XI_5 + \kappa_{-AB}XI_6 = 0$ and $\lim_{\tau_{\mathrm{III}}\to\infty} \mathrm{d}XI_6/\mathrm{d}\tau_{\mathrm{III}} = \kappa_{AB}XI_5 - \kappa_{-AB}XI_6 = 0$:

$$\begin{aligned}
\lim_{\tau_{\mathrm{III}}\to\infty} XI_5(\tau_{\mathrm{III}}) &= \frac{\kappa_{-AB}}{\kappa_{AB}+\kappa_{-AB}} XI_{56} \\
&\equiv \Gamma_{XI_5}, \\
\lim_{\tau_{\mathrm{III}}\to\infty} XI_6(\tau_{\mathrm{III}}) &= \frac{\kappa_{AB}}{\kappa_{AB}+\kappa_{-AB}} XI_{56} \\
&\equiv \Gamma_{XI_6}.
\end{aligned} \tag{5.13}$$

In the case of $i = 5, 6$, the quasi-conserved quantity, $XI_{50/60} \equiv XI_{50} + XI_{60}$, is introduced as in the case of $i = null$. The coarse-graining functions of XI_{50} and XI_{60} are also derived in the same way as in the case of $i = null$ (See Appendix C.1).

5.2.3 Coarse-grained model of PS I

According to the above results, the coarse-grained reaction network model of PSI-RC under continuous light is given. The diagram of the coarse-grained model of PS I is illustrated in Fig. 5.3. With respect to this PS I kinetic model, the rates of electron transfer outside PS I are set to be proportional to the product of the concentrations of the reactants. For the reactants outside PS I, the electron acceptors of PS I (ferredoxin (F), ferredoxin-NADP(H)-oxidoreductase (FNR)) and the electron donor for PS I (plastocyanin (Pc)) are introduced. In the following, the notations are adopted as below: Y_0 : [F]; Y_1 : [F^-], Z_{-1} : [$\mathrm{FNR_i}$]; Z_0 : [FNR]; Z_1 : [FNR^-]; Z_2 : [FNR^{2-}]; C_0 : [Pc^+]; C_1 : [Pc]. The activation process of inactive FNR ($\mathrm{FNR_i}$), the oxidation of FNR^{2-} and the reduction of oxidized Pc are assumed to be irreversible and proceed linearly with their concentration.

The ODEs with τ_{IV} of the coarse-grained kinetic model of PS I are expressed as

$$
\begin{cases}
\dfrac{\mathrm{d}XI_0}{\mathrm{d}\tau_{\mathrm{IV}}} & = -\kappa_0\Gamma_{WI_1}\dfrac{XI_0}{XI_T} + \kappa_{-0}\Gamma_{XI_1} + \kappa_{1P}(\Gamma_{XI_{3A}} + \Gamma_{XI_{3B}}) \\
& +\kappa_{PcP}XI_7\dfrac{C_1}{C_{\mathrm{T}}} - \kappa_{-PcP}XI_0\dfrac{C_0}{C_{\mathrm{T}}} + \kappa_{BF}\dfrac{YI_0}{YI_{\mathrm{T}}}\Gamma_{XI_{60}} - \kappa_{-BF}\dfrac{YI_1}{YI_{\mathrm{T}}}XI_0, \\
\dfrac{\mathrm{d}XI_{5/6}}{\mathrm{d}\tau_{\mathrm{IV}}} & = \kappa_4\Gamma_{XI_4} - \kappa_{-4}\Gamma_{XI_5} - \kappa_{BF}(\Gamma_{XI_6} - XI_{65})\dfrac{YI_0}{YI_{\mathrm{T}}} \\
& +\kappa_{-BF}(XI_7 - \Gamma_{XI_5})\dfrac{YI_1}{YI_{\mathrm{T}}} - \kappa_{PcP}XI_{5/6}\dfrac{C_1}{C_{\mathrm{T}}} + \kappa_{-PcP}XI_{60/50}\dfrac{C_0}{C_{\mathrm{T}}}, \\
\dfrac{\mathrm{d}XI_7}{\mathrm{d}\tau_{\mathrm{IV}}} & = \kappa_{BF}\Gamma_{XI_6}\dfrac{YI_0}{YI_{\mathrm{T}}} - \kappa_{-BF}XI_7\dfrac{YI_1}{YI_{\mathrm{T}}} - \kappa_{PcP}XI_7\dfrac{C_1}{C_{\mathrm{T}}} + \kappa_{-PcP}XI_0\dfrac{C_0}{C_{\mathrm{T}}}, \\
\dfrac{\mathrm{d}XI_{50/60}}{\mathrm{d}\tau_{\mathrm{IV}}} & = \kappa_{PcP}XI_{5/6}\dfrac{C_1}{C_{\mathrm{T}}} - \kappa_{-PcP}XI_{50/60}\dfrac{C_0}{C_{\mathrm{T}}} \\
& -\kappa_{BF}\dfrac{YI_0}{YI_{\mathrm{T}}}(\Gamma_{XI_{60}} - XI_{650}) + \kappa_{-BF}\dfrac{YI_1}{YI_{\mathrm{T}}}(XI_0 - \Gamma_{XI_{50}}) \\
& -\kappa_0\Gamma_{WI_1}\dfrac{XI_{50/60}}{XI_T} + \kappa_{-0}\Gamma_{XI_{6151}} + \kappa_{1P}(\Gamma_{XI_{53a}} + \Gamma_{XI_{63a}} + \Gamma_{XI_{53b}} + \Gamma_{XI_{63b}}), \\
\dfrac{\mathrm{d}XI_{65}}{\mathrm{d}\tau_{\mathrm{IV}}} & = \kappa_4\Gamma_{XI_{64}} - \kappa_{-4}XI_{65} - \kappa_{PcP}XI_{65}\dfrac{C_1}{C_{\mathrm{T}}} + \kappa_{-PcP}XI_{650}\dfrac{C_0}{C_{\mathrm{T}}} \\
& -\kappa_{BF}\dfrac{YI_0}{YI_{\mathrm{T}}}XI_{65} + \kappa_{-BF}\dfrac{YI_1}{YI_{\mathrm{T}}}\Gamma_{XI_5}, \\
\dfrac{\mathrm{d}XI_{650}}{\mathrm{d}\tau_{\mathrm{IV}}} & = \kappa_{PcP}XI_{65}\dfrac{C_1}{C_{\mathrm{T}}} - \kappa_{-PcP}XI_{650}\dfrac{C_0}{C_{\mathrm{T}}} - \kappa_{BF}\dfrac{YI_0}{YI_{\mathrm{T}}}XI_{650} + \kappa_{-BF}\dfrac{YI_1}{YI_{\mathrm{T}}}\Gamma_{XI_{50}} \\
& +\kappa_4\Gamma_{XI_{640}} - \kappa_{-4}XI_{650} - \kappa_0\Gamma_{WI_1}\dfrac{XI_{650}}{XI_T} + \kappa_{-0}\Gamma_{XI_{651}} + \kappa_{1P}(\Gamma_{X653a} + \Gamma_{X653b}), \\
\dfrac{\mathrm{d}XI_{6540}}{\mathrm{d}\tau_{\mathrm{IV}}} & = \varepsilon_{\mathrm{III,IV}}\kappa_{PcP}\Gamma_{XI_{654}}\dfrac{C_1}{C_{\mathrm{T}}} - \kappa_{-PcP}XI_{6540}\dfrac{C_0}{C_{\mathrm{T}}} \\
& -\kappa_{BF}\dfrac{YI_0}{YI_T}XI_{6540}.
\end{cases}
\tag{5.14}
$$

The ODEs with τ_{IV} of the kinetic model of electron carriers outside PS I are expresses as follows:

$$
\begin{cases}
\dfrac{\mathrm{d}YI_0}{\mathrm{d}\tau_{\mathrm{IV}}} & = -\kappa_{BF}(\Gamma_{XI_6}+\Gamma_{XI_{60}}+XI_{65}+XI_{650}+XI_{6540}+\varepsilon_{\mathrm{III,IV}}\Gamma_{XI_{654}})\dfrac{YI_0}{YI_{\mathrm{T}}} \\
& \quad +\kappa_{-BF}(XI_0+XI_7+\Gamma_{XI_5}+\Gamma_{XI_{50}})\dfrac{YI_1}{YI_{\mathrm{T}}} \\
& \quad +\kappa_{FFNR}(\dfrac{ZI_0}{ZI_{\mathrm{T}}}+\dfrac{ZI_1}{ZI_{\mathrm{T}}})YI_1-\kappa_{-FFNR}(ZI_1+ZI_2)\dfrac{YI_0}{YI_{\mathrm{T}}}, \\
\dfrac{\mathrm{d}YI_1}{\mathrm{d}\tau_{\mathrm{IV}}} & = \kappa_{BF}(\Gamma_{XI_6}+\Gamma_{XI_{60}}+XI_{65}+XI_{650}+XI_{6540}+\varepsilon_{\mathrm{III,IV}}\Gamma_{XI_{654}})\dfrac{YI_0}{YI_{\mathrm{T}}} \\
& \quad -\kappa_{-BF}(XI_0+XI_7+\Gamma_{XI_5}+\Gamma_{XI_{50}})\dfrac{YI_1}{YI_{\mathrm{T}}} \\
& \quad -\kappa_{FFNR}(\dfrac{ZI_0}{ZI_{\mathrm{T}}}+\dfrac{ZI_1}{ZI_{\mathrm{T}}})YI_1+\kappa_{-FFNR}(ZI_1+ZI_2)\dfrac{YI_0}{YI_{\mathrm{T}}}, \\
\dfrac{\mathrm{d}ZI_{-1}}{\mathrm{d}\tau_{\mathrm{IV}}} & = -\kappa_{FNRA}ZI_{-1}, \\
\dfrac{\mathrm{d}ZI_0}{\mathrm{d}\tau_{\mathrm{IV}}} & = \kappa_{FNRA}ZI_{-1}-\kappa_{FFNR}YI_1\dfrac{ZI_0}{ZI_{\mathrm{T}}}+\kappa_{-FFNR}ZI_1\dfrac{YI_0}{YI_{\mathrm{T}}}+\kappa_{FNR}ZI_2, \\
\dfrac{\mathrm{d}ZI_1}{\mathrm{d}\tau_{\mathrm{IV}}} & = \kappa_{FFNR}YI_1(\dfrac{ZI_0}{ZI_{\mathrm{T}}}-\dfrac{ZI_1}{ZI_{\mathrm{T}}})-\kappa_{-FFNR}(ZI_1-ZI_2)\dfrac{YI_0}{YI_{\mathrm{T}}}, \\
\dfrac{\mathrm{d}ZI_2}{\mathrm{d}\tau_{\mathrm{IV}}} & = \kappa_{FFNR}YI_1\dfrac{ZI_1}{ZI_{\mathrm{T}}}-\kappa_{-FFNR}ZI_2\dfrac{YI_0}{YI_{\mathrm{T}}}-\kappa_{FNR}ZI_2, \\
\dfrac{\mathrm{d}C_0}{\mathrm{d}\tau_{\mathrm{IV}}} & = -\kappa_{Pc}C_0+\kappa_{PcP}(XI_7+XI_{56}+XI_{65}+\varepsilon_{\mathrm{III,IV}}\Gamma_{XI_{65}})\dfrac{C_1}{CI_{\mathrm{T}}} \\
& \quad -\kappa_{-PcP}(XI_0+XI_{6050}+XI_{650}+XI_{6540})\dfrac{C_0}{C_{\mathrm{T}}}, \\
\dfrac{\mathrm{d}C_1}{\mathrm{d}\tau_{\mathrm{IV}}} & = \kappa_{Pc}C_0-\kappa_{PcP}(XI_7+XI_{56}+XI_{65}+\varepsilon_{\mathrm{III,IV}}\Gamma_{XI_{65}})\dfrac{C_1}{CI_{\mathrm{T}}} \\
& \quad +\kappa_{-PcP}(XI_0+XI_{6050}+XI_{650}+XI_{6540})\dfrac{C_0}{C_{\mathrm{T}}}.
\end{cases}
\tag{5.15}
$$

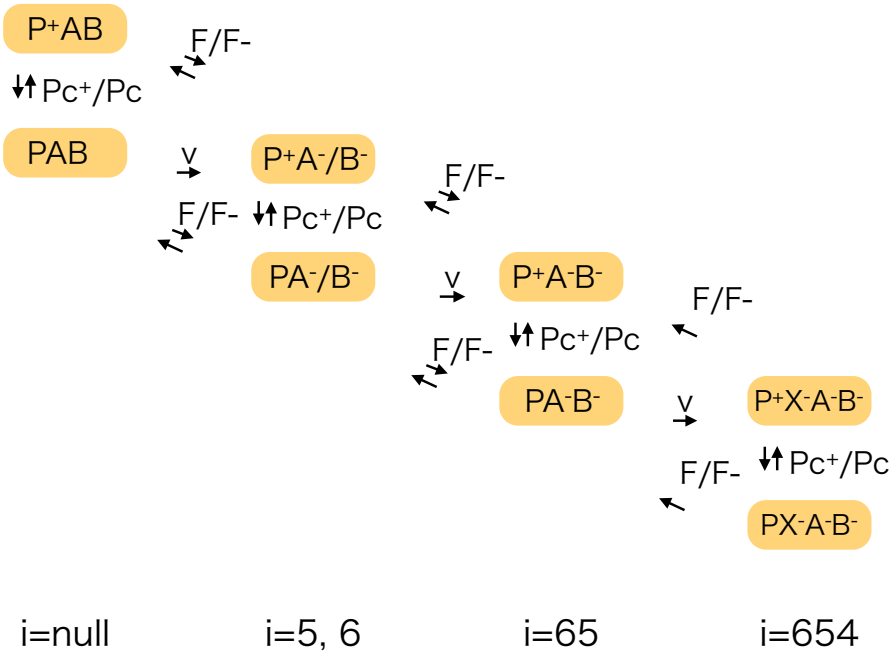

Figure 5.3 Coarse-grained picture of the diagram of PSI-RC reaction network. Here, the P_{700}, F_X, F_A and F_B sites are indicated by P, X, A and B, respectively. The notation PA^-/B^- means that the PS I realizes $P_{700}F_A^-F_B$ or $P_{700}F_AF_B^-$ state. The arrows marked with Pc^+/Pc, F/F^- and v indicate the reaction accompanied by the redox reactions of Pc, that of F and light absorption, respectively. The index i = 5, 6, 65 and 654 correspond to the F_A^-, F_B^-, $F_A^-F_B^-$ and $F_X^-F_A^-F_B^-$ states, respectively.

5.3 Results and Discussion

The results of the simulations for the dynamics of PS I in photosynthetic induction time are shown in this section. During the induction of photosynthesis, i.e, before the dark reactions of photosynthesis such as Calvin-Benson cycle are activated by light, the electron transfer reactions on thylakoid membrane are suitably regulated for light environment. Until the activations of the dark reactions are induced by light, the

amount of oxidized ferredoxin is limited and its reduced form builds up. Unless the plastocyanin pool is fully oxidized, P_{700}^{+} is reduced fast enough and then electrons linger on the acceptors of PS I upon further turnovers. It is necessary to dispose the extra absorbed energy that is not used for photosynthesis at this situation. With respect to such an energy-dissipation process, the charge-recombination processes are considered to play an important role [99]. In regard to the dynamics of PS I, the absorbance changes at 820 nm (relative to the absorbance at 870 nm), I_{820} signal, that reflects the amounts of P_{700}^{+} and Pc^{+} are known to show an characteristic pattern in time [100, 101]. With these in mind, the relations between the charge recombinations of the charge separated states, $P^{+}A_{1A}^{-}$ and $P^{+}A_{1B}^{-}$, and the characteristic pattern of the dynamics of I_{820} signal have been investigated.

First, the simulated I_{820} curve is illustrated in Fig. 5.4 along with the experimental results [60]. Here, the initial states are set as those in dark: $WI_0(0) = WI_{\mathrm{T}}$, $XI_0(0) = XI_{\mathrm{T}}$, $YI_0(0) = YI_{\mathrm{T}}$, $ZI_{-1}(0) = ZI_{\mathrm{T}}$, $C_1(0) = C_{\mathrm{T}}$ and otherwise 0. The ratio of $XI_{\mathrm{T}}/YI_{\mathrm{T}}/ZI_{\mathrm{T}}/C_{\mathrm{T}}/WI_{\mathrm{T}}$ is assumed to be 1/3/3/3/170. The photo-excitation rate used for the simulation is set to be $2000\,\mathrm{s}^{-1}$ which corresponds to the light flux density of 3,000 $\mu\mathrm{mol\,m^{-2}\,s^{-1}}$ used in the experiment [60]. These two curves agree well with respect to the inflection point at about 10^{-3}s, the peak at about 2×10^{-2}s and the relaxation at 10^{-1}s.

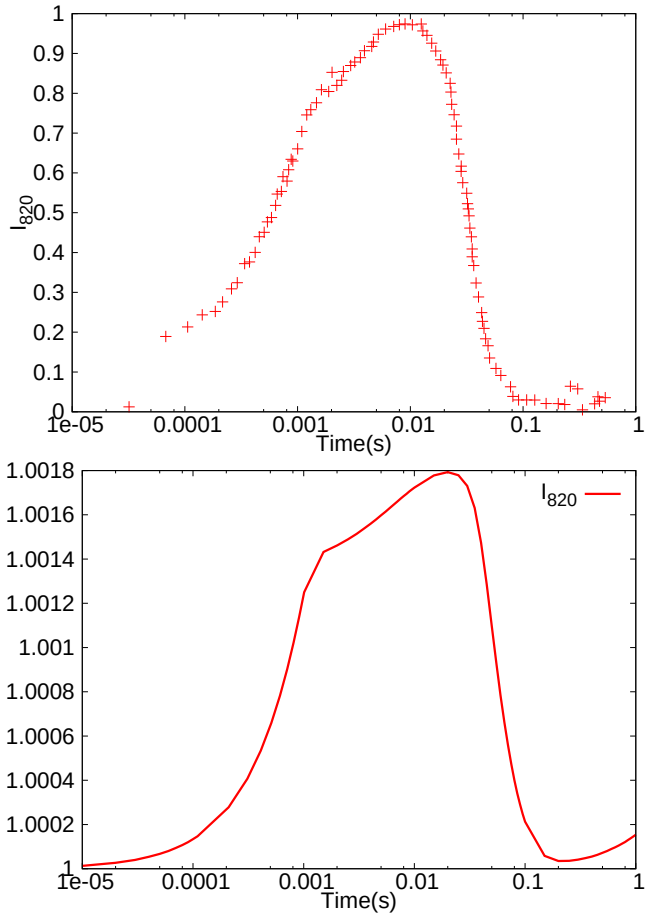

Figure 5.4 Dynamics of I_{820} signal. The upper figure is the experimental result (Modified from Lazar [60]) and the lower one is the result of simulation. The relative values are plotted in the upper figure. In simulation, I_{820} signal is caluculated by the Eq. (C.3) (See Appendix C.2).

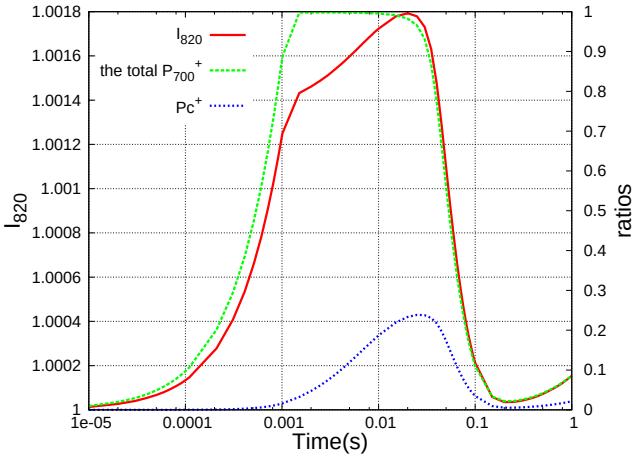

Figure 5.5 The simulated dynamics of I_{820} signal and the occupancies of the oxidized reactants, the total P^+_{700} and Pc^+.

Next, the dynamics of the occupancies of P^+_{700} and Pc^+ to each total amount are shown with I_{820} curve in Fig. 5.5. This figure indicates that the rise of I_{820} curve up to inflection point at 10^{-3}s reflects the accumulation of P^+_{700} and the increase from the inflection point to the peak at 2×10^{-2}s reflects the accumulation of Pc^+. Besides, the relaxation of I_{820} curve after the peak accompanies the decreases of both P^+_{700} and Pc^+.

The dynamics of the occupancies of PSI-RC states and those of the states of other electron carriers are shown in Fig. 5.6. With respect to the PSI-RC, the $P^+_{700}F^-_A/F^-_B$ state firstly increases among all the P^+_{700} states and then the $P^+_{700}F_AF_B$ state increases. The simultaneous increase of F^-, the reduced state of the electron acceptor of PS I, indicates that above change of PSI-RC accompanies the electron transfer from $P^+_{700}F_AF^-_B$ to F. In regard to the oxidized state of the electron donor, Pc^+, it increases with $P^+_{700}F^-_A/F^-_B$ and $P^+_{700}F^-_AF^-_B$ states at the same time. This means that the charge separations of $P_{700}F_AF_B$ and $P_{700}F^-_A/F^-_B$ states occur immediately after the Pc has been oxidized by $P^+_{700}F_AF_B$ and $P^+_{700}F^-_A/F^-_B$ states, respectively. The reduced states of the electron carriers accumulate substantially, and then the almost all ferredoxins become the reduced state, F^-. At this time, almost all PSI-RCs become $P_{700}F^-_AF^-_B$ state. Therefore the plastocyanin is no more oxidized by PSI. This indicates that the charge recombination process from $P^+_{700}A^-_{1A}F^-_AF^-_B$ or $P^+_{700}A^-_{1B}F^-_AF^-_B$ state to $P_{700}F^-_AF^-_B$ state is in active as shown in Fig. 5.7.

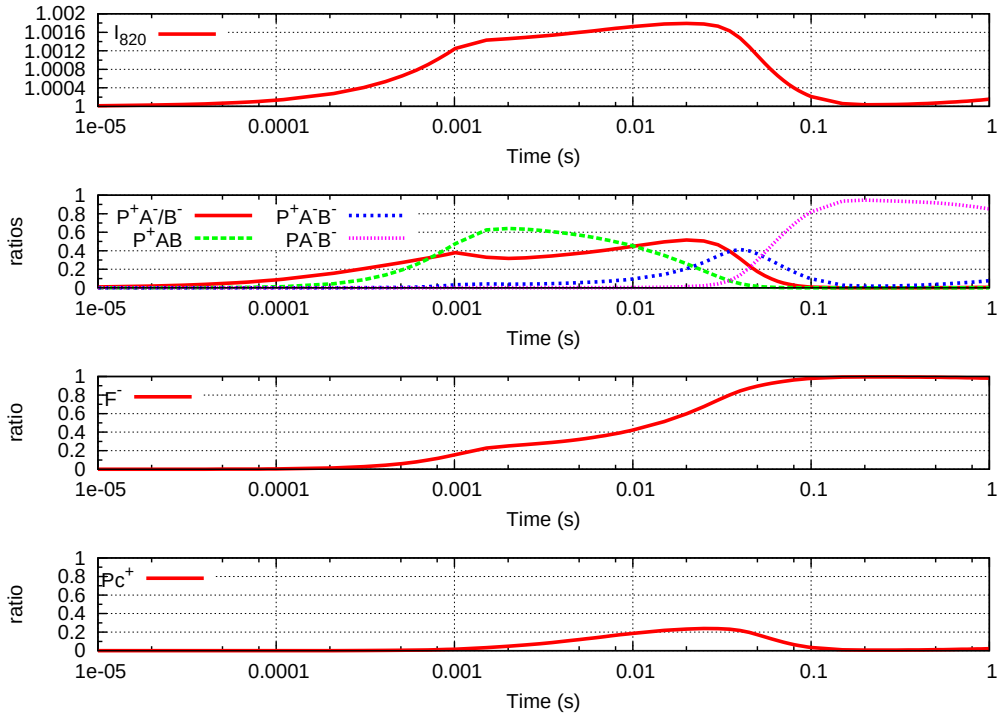

Figure 5.6 The simulated dynamics of I_{820} signal and each state of the electron carriers. Here, the notations P, A and B mean P_{700}, F_A and F_B, respectively.

The dynamics of the ratios of the rate of charge separation and that of charge recombination at each PSI-RC to the total rate of charge separation at PSI are plotted with I_{820} curve in Fig. 5.7. Figure 5.7 (b) shows the time courses of the ratios of the rates of charge separations at $P_{700}F_AF_B$, $P_{700}F_A^-/F_B^-$ and $P_{700}F_A^-F_B^-$ to the total rate of charge separation at PS I. Each ratio is represented by Φ_{AB}^{CS}, Φ_{A^-/B^-}^{CS} and $\Phi_{A^-B^-}^{CS}$, respectively. Interestingly, the active process following the charge separation from $P_{700}F_AF_B$ state is not the charge separation from $P_{700}F_A^-/F_B^-$ state but that from $P_{700}F_A^-F_B^-$ state. This means that the majority of the $P_{700}^+F_A^-F_B$ state produced via charge separation from $P_{700}F_AF_B$ state is reduced by F^- at acceptor side of PS I and then change into $P_{700}F_A^-F_B^-$ state not through $P_{700}F_A^-/F_B^-$ state.

The ratio of charge recombination rate at each PSI-RC to the total charge separation rate at PS I is plotted in Fig. 5.7 (c). Here, Φ_{AB}^{CR}, Φ_{A^-/B^-}^{CR} and $\Phi_{A^-B^-}^{CR}$ represent the ratios of the charge recombination rates of $P_{700}^+A_{1A}^-$ and $P_{700}^+A_{1B}^-$ at the PS I, where the states of ion sulfurs are in F_AF_B, F_A^-/F_B^- and $F_A^-F_B^-$ states, to the total charge separation rate at PS I, respectively. Through the comparison between Figs. 5.7 (b) and (c), it is revealed that the charge recombination rate is much smaller than the charge separation rate at the $P_{700}F_AF_B$ state on the one hand. But, on the other

hand, the time course of charge recombination rate is mostly the same as the charge separation rate at the $P_{700}F_A^-F_B^-$ state. This suggests that the charge recombination paths from $P_{700}^+A_{1A}^-F_A^-F_B^-$ and $P_{700}^+A_{1B}^-F_A^-F_B^-$ states to $P_{700}F_A^-F_B^-$ state play an important role for the dissipation of the extra absorbed energy. Thus it is revealed that the regulation mechanism for dissipation of extra absorbed energy exists in electron transfer chain of PS I. It is noted that this mechanism becomes active when the electrons are accumulated at acceptor side of PS I, and then PSI-RC is in the doubly reduced state, $P_{700}F_A^-F_B^-$.

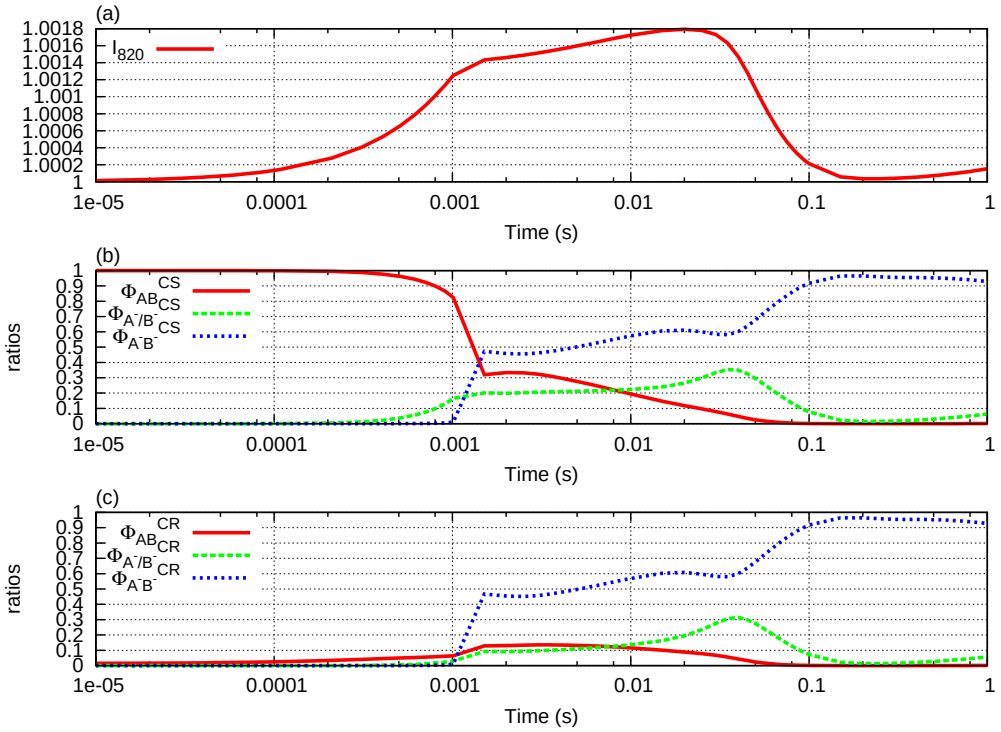

Figure 5.7 (a) The simulated dynamics of I_{820} signal, (b) the ratios of charge separation rates of each PSI-RC to the total charge separation rate, and (c) the ratios of charge recombination rates of each PSI-RC to the total charge separation rate.

5.4 Conclusions

In this chapter, the coarse-grained model of PS I is derived and applied for the simulation of the photosynthetic induction up to 1 s. With the use of the HCG method, the dimensionality of the state space of PSI-RC is reduced from 2^8 to 7 (the number of variables of Eq. (5.14)). With respect to the curve of I_{820} signal,

it is revealed that the increase towards the inflection point at about 10^{-3}s reflects the accumulation of P_{700}^{+} and the increase from that inflection point to the peak at 2×10^{-2}s reflects the accumulation of Pc^{+}. Besides, the decrease after the peak accompanies the increase of the doubly reduced PS I, $P_{700}F_{A}^{-}F_{B}^{-}$. The important role of the charge recombination from $P_{700}^{+}A_{1A}^{-}F_{A}^{-}F_{B}^{-}$ or $P_{700}^{+}A_{1B}^{-}F_{A}^{-}F_{B}^{-}$ state to $P_{700}F_{A}^{-}F_{B}^{-}$ state for the dissipation of extra energy has also been revealed. It is noted that other mechanisms of the regulation of electron transfer processes around PS I have been proposed at more slower time scales such as cyclic electron flow [102] and water-water-cycle [103], which are called alternative electron pathways in distinction from the ordinary linear electron pathway [104]. It seems that the model proposed here has a potential to describe the slower dynamics of photosynthesis in combination with the models that describe the further slower reactions of photosynthesis.

Chapter 6

General Conclusion and Perspective

The multi-hierarchy and complexity are the typical characteristics of the reactions in living body. To understand such a living system by intuition, it is necessary to construct a model that is composed of the essential elements [105]. In this study, I have tried to extract such a essential model of photosynthesis that is consistent with the full detailed model.

In Chapter 3, I have presented a hierarchical coarse-graining (HCG) method in time which can reduce the complexity and the multi-timescale property of photosynthesis reaction models. This method is proposed based on the three variable model and then applied to the simplified model of PS II. As a result, the multi-timescale model of PS II is transformed into the mono-timescale one with sufficient accuracy.

Through this new method, the phenomenological structures of photosystem II and photosystem I at millisecond scale can be systematically derived. It is important that derived models have been revealed to have an ability to clearly explain the fluorescence induction phenomena and the I_{820} signal curve.

In Chapter 4, the full model of PS II combined with OEC and LHA is coarse grained through the HCG method. Two different coarse-grained models are derived in response to the difference in the rate constants of the electron transfer at donor side of PS II. The analysis of reaction network reveals that the coarse-grained model that is consistent with the results of experiments is that derived in the case where the electron transfer at donor side of PS II can be assumed in quasi-equilibrium. With respect to FI, it is revealed that the light-intensity dependent changes of the transient patterns from O-J-I-P to O-J-D-I-P reflect the changes of the states of the donor side of PS II. The factor that affects the FI pattern is P^+_{680} quenching or Y^+_Z quenching corresponding to the different coarse-grained model.

In Chapter 5, the coarse-grained model of PS I is obtained through the HCG method base on the model that has the 2^8 dimensionality in the state space of RC. The obtained model describes RC by seven state variables. The simulation of the photosynthetic induction reveals what the I_{820} curve reflects. The increase up to the inflection point at 10^{-3} s, the increase from that point to the peak at 2×10^{-2} s, and the decay after that peak reflect the accumulations of P_{700}^{+}, Pc^{+} and $P_{700}F_{A}^{-}F_{B}^{-}$, respectively. Besides, it is revealed that once the PSI-RC realized the $P_{700}F_{A}^{-}F_{B}^{-}$ state the charge recombination processes from $P_{700}^{+}A_{1A}^{-}$ and $P_{700}^{+}A_{1A}^{-}$ states play the important role for the dissipation of the extra absorbed energy.

The remaining problem is concerned with the explanation of the slow-change pattern of fluorescence induction phenomena. This phenomena is regarded to be affected by NPQ processes as explained in Chapter 2. Though various mechanisms concerning the environmental response at this timescale range from seconds to minutes are proposed, the relationships between them are still being debated [106]. To cope with this problem, it seems useful to derive the phenomenological structure of the reaction on thylakoid membrane by combining the models of the NPQ with the models of PS II and PS I obtained in this study, and then to analyze the phenomena systematically. Furthermore, in combination with the model of dark reactions such as Calvin-Benson cycle, the phenomenological model of photosynthesis in chloroplast that is consistent with the full detailed model would be obtained.

Acknowledgements

First of all, I would like to express my sincere gratitude to my supervisor, Prof. Shigenori Tanaka, for his kind guidance and helpful advice during my graduate course at Kobe University. I am deeply grateful to Prof. Kuniyoshi Ebina, who is my supervisor of my master's course, for his in-depth guidance and suggestive comments throughout my graduate course. I especially would like to thank Dr. Kazuhiro Fujimoto for his helpful advice and great encouragement to this work. I would like to express my gratitude to Prof. Kensuke Ikeda who is my supervisor during my undergraduate course at Ritsumeikan University. His enthusiasm always encourages me. I would like to thank Mr. Yosuke Suzuki for numerous insightful discussions with him. I am grateful to Mr. Kazuo Teraoka for his kind support and encouragement. I greatly appreciate the feedback offered by Mr. Kazuhiro Jogo about this work. I would like to thank Mr. Tomoyuki Sugamoto for the instructive discussions with him about theoretical physics. I would like to thank the members of Tanaka and Ebina groups. I am particularly grateful for the cordial assistance given by Noriko Ito. My heartfelt appreciation goes to Eriko Okada for her thoughtful support and encouragement. I would like to show my greatest appreciation to my grand mother, Mrs. Kazuko Matsuoka for her grateful support during my time of graduate course at Kobe. Finally, I would like to express my deepest appreciation to my parents, Mr. Kyoji Matsuoka and Mrs. Atsuko Matsuoka for their supports throughout my time of graduate course at Kobe University.

Appendix A

A.1 Linear stability analysis

A.1.1 The case of a

With respect to the ODEs constructed by neglecting the $\mathcal{O}(\varepsilon_{\mathrm{I,II}})$ terms in Eq. (3.3), each ODE is denoted in terms of F_n as

$$\begin{cases} \frac{dx_0}{d\tau_{\mathrm{I}}} &= \kappa_b x_2 - \kappa_f x_1 x_0 = F_0, \\ \frac{dx_1}{d\tau_{\mathrm{I}}} &= \kappa_b x_2 - \kappa_f x_1 x_0 = F_1, \\ \frac{dx_2}{d\tau_{\mathrm{I}}} &= -\kappa_b x_2 + \kappa_f x_1 x_0 = F_2. \end{cases} \tag{A.1}$$

The steady state of these ODEs is considered. The solution $\bar{\boldsymbol{x}} = (\bar{x}_0, \bar{x}_1, \bar{x}_2)^{\mathrm{T}}$ to these ODEs at the steady state is called an equilibrium point. Then, the linear stability analysis for $\bar{\boldsymbol{x}} + \Delta\boldsymbol{x}$, which is displaced by $\Delta\boldsymbol{x} = (\Delta x_0, \Delta x_1, \Delta x_2)^{\mathrm{T}}$ from the equilibrium point, is attempted. By substituting $\bar{\boldsymbol{x}} + \Delta\boldsymbol{x}$ into Eq. (A.1), the ODEs of $\Delta\boldsymbol{x}$ are obtained as

$$\begin{aligned} \frac{d\Delta\boldsymbol{x}}{d\tau_{\mathrm{I}}} &= \boldsymbol{\Lambda}\Delta\boldsymbol{x}, \\ \boldsymbol{\Lambda} &= \begin{pmatrix} \frac{\partial F_0}{\partial x_0} & \frac{\partial F_0}{\partial x_1} & \frac{\partial F_0}{\partial x_2} \\ \frac{\partial F_1}{\partial x_0} & \frac{\partial F_1}{\partial x_1} & \frac{\partial F_1}{\partial x_2} \\ \frac{\partial F_2}{\partial x_0} & \frac{\partial F_2}{\partial x_1} & \frac{\partial F_2}{\partial x_2} \end{pmatrix}, \\ &= \begin{pmatrix} -\kappa_f \bar{x}_1 & -\kappa_f \bar{x}_0 & \kappa_b \\ -\kappa_f \bar{x}_1 & -\kappa_f \bar{x}_0 & \kappa_b \\ \kappa_f \bar{x}_1 & \kappa_f \bar{x}_0 & -\kappa_b \end{pmatrix}. \end{aligned} \tag{A.2}$$

$\boldsymbol{\Lambda}$ is called the Jacobian matrix. By solving the eigenvalue equation $|\mathbf{I}\lambda - \boldsymbol{\Lambda}| = \mathbf{0}$ for λ, the eigenvalues of the Jacobian matrix are obtained as

$$\lambda_0 = \lambda_1 = 0, \lambda_2 = -(\kappa_f \bar{x}_1 + \kappa_f \bar{x}_0 + \kappa_b). \tag{A.3}$$

The eigenvectors $\mathbf{p_0}$, $\mathbf{p_1}$, $\mathbf{p_2}$ of each λ_0, λ_1, λ_2 are obtained by solving the following equation:

$$(\mathbf{I}\lambda_\mathbf{n} - \mathbf{\Lambda})\mathbf{p_n} = \mathbf{0}. \tag{A.4}$$

A matrix $\mathbf{P}$, which is formed by the eigenvectors $\mathbf{p_0}, \mathbf{p_1}, \mathbf{p_2}$ is then introduced as

$$\begin{aligned} \mathbf{P} &= \begin{pmatrix} \mathbf{p_0} & \mathbf{p_1} & \mathbf{p_2} \end{pmatrix}, \\ &= \begin{pmatrix} \bar{x}_0 & \kappa_b & 1 \\ -\bar{x}_1 & \kappa_b & 1 \\ 0 & \kappa_f(\bar{x}_0 + \bar{x}_1) & -1 \end{pmatrix}. \end{aligned} \tag{A.5}$$

By substituting $\Delta\boldsymbol{x} = \mathbf{P}\boldsymbol{y}$, Eq. (A.2) is transformed to a linear differential equation of $\boldsymbol{y} = (y_0, y_1, y_2)^{\mathrm{T}}$ as

$$\begin{aligned} \frac{d}{d\tau_\mathrm{I}}\boldsymbol{y} &= \mathbf{P^{-1}}\mathbf{\Lambda}\mathbf{P}\boldsymbol{y}, \\ &= \begin{pmatrix} 0 & 0 & 0 \\ 0 & 0 & 0 \\ 0 & 0 & \lambda_2 \end{pmatrix} \boldsymbol{y}. \end{aligned} \tag{A.6}$$

The relaxation time of the perturbation $\Delta\boldsymbol{x}$ for the steady state of Eq. (A.2) is estimated as $\mathcal{O}(-\frac{1}{\lambda_2})$ from this result.

A.1.2 The case of b

With respect to the ODEs constructed by neglecting the $\mathcal{O}(\varepsilon_{\mathrm{I,II}})$ terms in Eq. (3.7),

$$\begin{cases} \frac{dx_0}{d\tau_\mathrm{I}} &= \kappa_b x_2 - \kappa_f x_1 x_0, \\ \frac{dx_1}{d\tau_\mathrm{I}} &= -\kappa_1 x_1 + \kappa_b x_2 - \kappa_f x_1 x_0, \\ \frac{dx_2}{d\tau_\mathrm{I}} &= -\kappa_b x_2 + \kappa_f x_1 x_0, \end{cases} \tag{A.7}$$

the linear stability analysis for the point displaced by $\Delta\boldsymbol{x} = (\Delta x_0, \Delta x_1, \Delta x_2)^{\mathrm{T}}$ from the equilibrium point is attempted. This analysis can be performed by introducing the ODEs for $\Delta\boldsymbol{x}$ as well as in the case of a:

$$\begin{aligned} \frac{d\Delta\boldsymbol{x}}{d\tau_\mathrm{I}} &= \Lambda\Delta\boldsymbol{x}, \\ \Lambda &= \begin{pmatrix} -\kappa_f\bar{x}_1 & -\kappa_f\bar{x}_0 & \kappa_b \\ -\kappa_f\bar{x}_1 & -\kappa_1 - \kappa_f\bar{x}_0 & \kappa_b \\ \kappa_f\bar{x}_1 & \kappa_f\bar{x}_0 & -\kappa_b \end{pmatrix}. \end{aligned} \tag{A.8}$$

The eigenvalues of the Jacobian matrix are obtained as

$$\lambda_0 = 0, \lambda_\pm = \frac{-(\kappa_1 + \kappa_b + \kappa_f(\bar{x}_0 + \bar{x}_1)) \pm \sqrt{(\kappa_1 + \kappa_b + \kappa_f(\bar{x}_0 + \bar{x}_1))^2 - 4\kappa_1(\kappa_b + \kappa_f \bar{x}_1)}}{2}. \tag{A.9}$$

A matrix $\mathbf{P} = (\mathbf{p_0}\ \mathbf{p}_+\ \mathbf{p}_-)$, which is formed by each eigenvector, is introduced. By substituting $\Delta\boldsymbol{x} = \mathbf{P}\boldsymbol{y}$, Eq. (A.8) is transformed to a linear differential equation of $\boldsymbol{y} = (y_0, y_1, y_2)^{\mathrm{T}}$:

$$\frac{d}{d\tau_{\mathrm{I}}}\boldsymbol{y} = \begin{pmatrix} 0 & 0 & 0 \\ 0 & \lambda_+ & 0 \\ 0 & 0 & \lambda_- \end{pmatrix} \boldsymbol{y}. \tag{A.10}$$

The relaxation time of the perturbation $\Delta\boldsymbol{x}$ for the steady state of Eq. (A.8) is estimated as $\mathcal{O}(-\frac{1}{\lambda_+})$ from this result.

A.1.3 The case of c

Concerning the ODEs constructed by neglecting the $\mathcal{O}(\varepsilon_{\mathrm{I,II}})$ terms in Eq. (3.14),

$$\begin{cases} \frac{dx_0}{d\tau_{\mathrm{I}}} &= \kappa_b x_2 - \kappa_f x_1 x_0, \\ \frac{dx_1}{d\tau_{\mathrm{I}}} &= -\kappa_1 x_1 + \kappa_b x_2 - \kappa_f x_1 x_0, \\ \frac{dx_2}{d\tau_{\mathrm{I}}} &= -\kappa_2 x_2 - \kappa_b x_2 + \kappa_f x_1 x_0, \end{cases} \tag{A.11}$$

the linear stability analysis for the point displaced by $\Delta\boldsymbol{x} = (\Delta x_0, \Delta x_1, \Delta x_2)^{\mathrm{T}}$ from the equilibrium point is attempted. This analysis can be performed by introducing the ODEs for $\Delta\boldsymbol{x}$ as well as in the case of a:

$$\begin{aligned} \frac{d\Delta\boldsymbol{x}}{d\tau_{\mathrm{I}}} &= \Lambda\Delta\boldsymbol{x}, \\ \Lambda &= \begin{pmatrix} -\kappa_f\bar{x}_1 & -\kappa_f\bar{x}_0 & \kappa_b \\ -\kappa_f\bar{x}_1 & -\kappa_1 - \kappa_f\bar{x}_0 & \kappa_b \\ \kappa_f\bar{x}_1 & \kappa_f\bar{x}_0 & -\kappa_b - \kappa_3 \end{pmatrix}. \end{aligned} \tag{A.12}$$

The eigenvalues of the Jacobian matrix are obtained as

$$
\begin{aligned}
\lambda_0 &= \omega_0 \sqrt[3]{-q+\sqrt{q^2+p^3}} + \omega_0 \sqrt[3]{-q-\sqrt{q^2+p^3}} - \frac{1}{3}a, \\
\lambda_1 &= \omega_1 \sqrt[3]{-q+\sqrt{q^2+p^3}} + \omega_2 \sqrt[3]{-q-\sqrt{q^2+p^3}} - \frac{1}{3}a, \\
\lambda_2 &= \omega_2 \sqrt[3]{-q+\sqrt{q^2+p^3}} + \omega_1 \sqrt[3]{-q-\sqrt{q^2+p^3}} - \frac{1}{3}a,
\end{aligned}
\tag{A.13}
$$

where $\omega_0 = 1, \omega_1 = \frac{-1+i\sqrt{3}}{2}, \omega_2 = \frac{-1-i\sqrt{3}}{2}, q = \frac{1}{2}c - \frac{1}{6}ab + \frac{1}{27}a^3$, and $p = \frac{1}{3}b - \frac{1}{9}a^2$. a, b, and c are given by

$$
\begin{aligned}
a &= \kappa_1 + \kappa_f(\bar{x}_1 + \bar{x}_2), \\
b &= [\kappa_1 + \kappa_f(\bar{x}_1 + \bar{x}_2)]\kappa_3 + \kappa_1\kappa_b + \kappa_1\kappa_f\bar{x}_1, \\
c &= \kappa_1\kappa_3.
\end{aligned}
\tag{A.14}
$$

A matrix $\mathbf{P} = (\mathbf{p_0}\ \mathbf{p_1}\ \mathbf{p_2})$, formed by each eigenvector is introduced. By putting $\Delta\boldsymbol{x} = \mathbf{P}\boldsymbol{y}$, Eq. (A.12) is transformed to a linear differential equation of $\boldsymbol{y} = (y_0, y_1, y_2)^{\mathrm{T}}$ as

$$
\frac{d}{d\tau_{\mathrm{I}}}\boldsymbol{y} = \begin{pmatrix} \lambda_0 & 0 & 0 \\ 0 & \lambda_1 & 0 \\ 0 & 0 & \lambda_2 \end{pmatrix} \boldsymbol{y}. \tag{A.15}
$$

The relaxation time of the perturbation $\Delta\boldsymbol{x}$ for the steady state of Eq. (A.12) is estimated as $\mathcal{O}(-\frac{1}{\lambda_0})$ from this result.

A.2 The ODEs with τ_{IV}

The ODEs with τ_{IV} (Eq. (3.29)) neglecting $\mathcal{O}(\varepsilon^2_{\mathrm{III,IV}})$ terms are expressed as

$$
\begin{cases}
\dfrac{dX_{01}}{d\tau_{\mathrm{IV}}} &= -\{1 + \varepsilon_{\mathrm{III,IV}}[\dfrac{\kappa_3\kappa_4}{\mathrm{Z_T}}(\mathrm{Z_T} - Z_1) - \kappa_{-0}]\}\nu_I\gamma^f_{U_1} - \varepsilon_{\mathrm{III,IV}}\kappa_{-2}\gamma^b_{X_2}\nu_I(\gamma^f_{U_1})^2 \\
&\quad + \dfrac{\kappa_4}{\mathrm{Z_T}}(\mathrm{Z_T} - Z_1)(\mathrm{R_T} - X_{01}) - \dfrac{\kappa_{-4}}{\mathrm{R_T}}X_{01}Z_1, \\
\dfrac{dZ_1}{d\tau_{\mathrm{IV}}} &= -\kappa_5 Z_1 + \dfrac{\kappa_4}{\mathrm{Z_T}}(\mathrm{Z_T} - Z_1)(\mathrm{R_T} - X_{01} + \varepsilon_{\mathrm{III,IV}}\nu_I\gamma^f_{U_1}) - \dfrac{\kappa_{-4}}{\mathrm{R_T}}X_{01}Z_1.
\end{cases}
\tag{A.16}
$$

Appendix B

B.1 The case that hole transfer from $\mathbf{Y}_{\mathbf{Z}}^{+}$ to RC is taken into account

B.1.1 ODEs with dimensionless time

The equations which have $\mathcal{O}(1)$ terms in ODEs with τ_{I} are

$$\begin{cases} \frac{dW_1}{d\tau_{\mathrm{I}}} &= -\bar{\kappa_{\mathrm{t}}}\frac{X_0+Y_0}{R_{\mathrm{T}}}W_1 + \bar{\kappa}_{-\mathrm{t}}\frac{W_0}{W_{\mathrm{T}}}(X_1+Y_1) + \mathcal{O}(\varepsilon_{\mathrm{I,II}}), \\ \frac{dX_0}{d\tau_{\mathrm{I}}} &= -\bar{\kappa_{\mathrm{t}}}\frac{X_0}{R_{\mathrm{T}}}W_1 + \bar{\kappa}_{-\mathrm{t}}\frac{W_0}{W_{\mathrm{T}}}X_1 + \mathcal{O}(\varepsilon_{\mathrm{I,II}}), \\ \frac{dX_1}{d\tau_{\mathrm{I}}} &= \bar{\kappa_{\mathrm{t}}}\frac{X_0}{R_{\mathrm{T}}}W_1 - \bar{\kappa}_{-\mathrm{t}}\frac{W_0}{W_{\mathrm{T}}}X_1 + \mathcal{O}(\varepsilon_{\mathrm{I,II}}), \\ \frac{dY_0}{d\tau_{\mathrm{I}}} &= -\bar{\kappa_{\mathrm{t}}}\frac{Y_0}{R_{\mathrm{T}}}W_1 + \bar{\kappa}_{-\mathrm{t}}\frac{W_0}{W_{\mathrm{T}}}Y_1 + \mathcal{O}(\varepsilon_{\mathrm{I,II}}), \\ \frac{dY_1}{d\tau_{\mathrm{I}}} &= \bar{\kappa_{\mathrm{t}}}\frac{Y_0}{R_{\mathrm{T}}}W_1 - \bar{\kappa}_{-\mathrm{t}}\frac{W_0}{W_{\mathrm{T}}}Y_1 + \mathcal{O}(\varepsilon_{\mathrm{I,II}}), \\ W_0 &= W_{\mathrm{T}} - W_1. \end{cases} \tag{B.1}$$

The equations which have $\mathcal{O}(1)$ terms in ODEs with τ_{II} are

$$
\begin{cases}
\frac{dV_1}{d\tau_{\mathrm{II}}} & = \kappa_{\mathrm{U}} U_1 p(W_1 \mid U_1) \frac{V_{\mathrm{T}} - V_1}{V_{\mathrm{T}}} - \kappa_{\mathrm{U}} \frac{W_{\mathrm{T}} - \Gamma_{\mathrm{W}_1}}{W_{\mathrm{T}}} V_1 \\
& \quad -(\kappa_{\mathrm{F}} + \kappa_{\mathrm{d}} + \kappa_{\mathrm{c}} \frac{X_2 + X_4 + Y_2 + Y_4}{\mathrm{R}_{\mathrm{T}}} + \kappa_{\mathrm{q}} \frac{Q_0}{Q_{\mathrm{T}}}) V_1, \\
\frac{dU_1}{d\tau_{\mathrm{II}}} & = -\kappa_{\mathrm{U}} U_1 p(W_1 \mid U_1) \frac{V_{\mathrm{T}} - V_1}{V_{\mathrm{T}}} + \kappa_{\mathrm{U}} \frac{W_{\mathrm{T}} - \Gamma_{\mathrm{W}_1}}{W_{\mathrm{T}}} V_1 \\
& \quad -(\kappa_{\mathrm{F}} + \kappa_{\mathrm{d}} + \kappa_{\mathrm{c}} \frac{X_2 + X_4 + Y_2 + Y_4}{R_{\mathrm{T}}} + \kappa_{\mathrm{q}} \frac{Q_0}{Q_{\mathrm{T}}}) U_1 \\
& \quad -\kappa_1^{\mathrm{o}} U_1 p(X_1 \mid U_1) - \kappa_1^{\mathrm{c}} U_1 p(Y_1 \mid U_1) + \kappa_{-1}^{\mathrm{o}} X_2 + \kappa_{-1}^{\mathrm{c}} Y_2 + \mathcal{O}(\varepsilon_{\mathrm{II,IV}}), \\
\frac{dX_{01}}{d\tau_{\mathrm{II}}} & = (\kappa_{-1}^{\mathrm{o}} + \kappa_{\mathrm{nr}}^{\mathrm{ind}}) X_2 - \kappa_1^{\mathrm{o}} U_1 p(X_1 \mid U_1) + \kappa_0^{\mathrm{ntr}} X_0^{\mathrm{tr}} + \mathcal{O}(\varepsilon_{\mathrm{II,III}}), \\
\frac{dX_2}{d\tau_{\mathrm{II}}} & = -(\kappa_2 + \kappa_{-1}^{\mathrm{o}} + \kappa_{\mathrm{tr}} + \kappa_{\mathrm{nr}}^{\mathrm{ind}}) X_2 + \kappa_1^{\mathrm{o}} U_1 p(X_1 \mid U_1) + \mathcal{O}(\varepsilon_{\mathrm{II,III}}), \\
\frac{dY_4}{d\tau_{\mathrm{II}}} & = \kappa_2 X_2 + \mathcal{O}(\varepsilon_{\mathrm{II,III}}), \\
\frac{dY_{01}}{d\tau_{\mathrm{II}}} & = \kappa_{-1}^{\mathrm{c}} Y_2 + \kappa_2 X_3 - \kappa_1^{\mathrm{c}} U_1 p(Y_1 \mid U_1) + \mathcal{O}(\varepsilon_{\mathrm{II,III}}), \\
\frac{dY_2}{d\tau_{\mathrm{II}}} & = -(\kappa_{-1}^{\mathrm{c}} + \kappa_{\mathrm{tr}} + \kappa_{\mathrm{nr}}^{\mathrm{ind}}) Y_2 + \kappa_1^{\mathrm{c}} U_1 p(Y_1 \mid U_1) + \mathcal{O}(\varepsilon_{\mathrm{II,III}}), \\
\frac{dX_3}{d\tau_{\mathrm{II}}} & = -\kappa_2 X_3 + \mathcal{O}(\varepsilon_{\mathrm{II,III}}), \\
\frac{dX_2^{\mathrm{tr}}}{d\tau_{\mathrm{II}}} & = \kappa_{\mathrm{tr}} X_2 - \kappa_{02}^{\mathrm{tr}} X_2^{\mathrm{tr}}, \\
\frac{dX_0^{\mathrm{tr}}}{d\tau_{\mathrm{II}}} & = \kappa_{02}^{\mathrm{tr}} X_2^{\mathrm{tr}} - \kappa_0^{\mathrm{ntr}} X_0^{\mathrm{tr}}, \\
\frac{dY_2^{\mathrm{tr}}}{d\tau_{\mathrm{II}}} & = \kappa_{\mathrm{tr}} Y_2 - \kappa_{02}^{\mathrm{tr}} Y_2^{\mathrm{tr}}, \\
\frac{dY_0^{\mathrm{tr}}}{d\tau_{\mathrm{II}}} & = \kappa_{02}^{\mathrm{tr}} Y_2^{\mathrm{tr}} - \kappa_0^{\mathrm{ntr}} Y_0^{\mathrm{tr}}.
\end{cases}
\tag{B.2}
$$

The equations which have $\mathcal{O}(1)$ terms in ODEs with τ_{III} are

$$
\begin{cases}
\frac{dX_{01}}{d\tau_{\mathrm{III}}} & = \kappa_3 \frac{T_0}{T_{\mathrm{T}}} X_4 - \kappa_{-3} \frac{T_1}{T_{\mathrm{T}}} X_{01} + \mathcal{O}(\varepsilon_{\mathrm{III,IV}}), \\
\frac{dY_4}{d\tau_{\mathrm{III}}} & = -\kappa_3 \frac{T_0}{T_{\mathrm{T}}} Y_4 + \kappa_{-3} \frac{T_1}{T_{\mathrm{T}}} Y_{01} + \mathcal{O}(\varepsilon_{\mathrm{III,IV}}), \\
\frac{dX_4}{d\tau_{\mathrm{III}}} & = -\kappa_3 \frac{T_0}{T_{\mathrm{T}}} X_4 + \kappa_{-3} \frac{T_1}{T_{\mathrm{T}}} X_{01} + \mathcal{O}(\varepsilon_{\mathrm{III,IV}}), \\
\frac{dY_{01}}{d\tau_{\mathrm{III}}} & = \kappa_3 \frac{T_0}{T_{\mathrm{T}}} Y_4 - \kappa_{-3} \frac{T_1}{T_{\mathrm{T}}} Y_{01} + \mathcal{O}(\varepsilon_{\mathrm{III,IV}}), \\
\frac{dT_1}{d\tau_{\mathrm{III}}} & = \kappa_3 \frac{T_0}{T_{\mathrm{T}}} (Y_4 + X_4) - \kappa_{-3} \frac{T_1}{T_{\mathrm{T}}} (X_0 + Y_0 + Y_3) + \mathcal{O}(\varepsilon_{\mathrm{III,IV}}), \\
\frac{dT_0}{d\tau_{\mathrm{III}}} & = -\kappa_3 \frac{T_0}{T_{\mathrm{T}}} (Y_4 + X_4) + \kappa_{-3} \frac{T_1}{T_{\mathrm{T}}} (X_0 + Y_0 + Y_3) + \mathcal{O}(\varepsilon_{\mathrm{III,IV}}), \\
\frac{dY_3}{d\tau_{\mathrm{III}}} & = -\kappa_{-3} \frac{T_1}{T_{\mathrm{T}}} Y_3 + \mathcal{O}(\varepsilon_{\mathrm{II,III}}) + \mathcal{O}(\varepsilon_{\mathrm{III,IV}}).
\end{cases}
\tag{B.3}
$$

The ODEs with τ_{IV} neglecting $\mathcal{O}(\varepsilon_{\mathrm{III,IV}})$ and $\mathcal{O}(\varepsilon_{\mathrm{II,III}})$ terms are expressed by the coarse-graining functions as

$$
\begin{cases}
\frac{dE}{d\tau_{\mathrm{IV}}} & = -\kappa_1^{\mathrm{o}}\gamma_{X_2}^{\mathrm{f}}\Gamma_{X_1} + (1-\gamma_{X_2}^{\mathrm{f}}+\kappa_{\mathrm{nr}}^{\mathrm{d}})\Gamma_{Y_4} + \sum_{i=0}^{3}\kappa_{i*,i}\frac{S_i}{S_{\mathrm{T}}}\Gamma_{T_1} + \kappa_{0,4}TS_4, \\
\frac{dX_{04}}{d\tau_{\mathrm{IV}}} & = -\kappa_1^{\mathrm{o}}\gamma_{X_2}^{\mathrm{f}}\Gamma_{X_1} + (1-\gamma_{X_2}^{\mathrm{f}}+\kappa_{\mathrm{nr}}^{\mathrm{d}})\Gamma_{Y_4} + \frac{\kappa_{41}Z_0+\kappa_{42}Z_1}{Z_{\mathrm{T}}}Y_{04} - (\kappa_{-41}Z_1+\kappa_{-42}Z_2)\frac{X_{04}}{R_{\mathrm{T}}}, \\
\frac{dZ_1}{d\tau_{\mathrm{IV}}} & = \kappa_{41}\frac{Z_0}{Z_{\mathrm{T}}}Y_{04} - \kappa_{-41}\frac{X_{04}}{R_{\mathrm{T}}}Z_1 - \kappa_{42}\frac{Z_1}{Z_{\mathrm{T}}}Y_{04} + \kappa_{-42}\frac{X_{04}}{R_{\mathrm{T}}}Z_2, \\
\frac{dZ_2}{d\tau_{\mathrm{IV}}} & = \kappa_{42}\frac{Z_1}{Z_{\mathrm{T}}}Y_{04} - \kappa_{-42}\frac{X_{04}}{R_{\mathrm{T}}}Z_2 - \kappa_5 Z_2\frac{Q_0}{Q_{\mathrm{T}}} + \kappa_{-5}Z_0\frac{Q_1}{Q_{\mathrm{T}}}, \\
\frac{dQ_1}{d\tau_{\mathrm{IV}}} & = \kappa_5 Z_2\frac{Q_0}{Q_{\mathrm{T}}} - \kappa_{-5}Z_0\frac{Q_1}{Q_{\mathrm{T}}} - \kappa_6 Q_1, \\
\frac{dS_i}{d\tau_{\mathrm{IV}}} & = \kappa_{i-1*,i-1}\frac{S_{i-1}}{S_{\mathrm{T}}}\Gamma_{T_1} - \kappa_{i*,i}\frac{S_i}{S_{\mathrm{T}}}\Gamma_{T_1}, \\
\frac{dTS_3^*}{d\tau_{\mathrm{IV}}} & = \kappa_{3*,3}\frac{S_3}{S_{\mathrm{T}}}\Gamma_{T_1} - \kappa_{4,3*}TS_3^* + \kappa_{3*,4}TS_4, \\
\frac{dTS_4}{d\tau_{\mathrm{IV}}} & = \kappa_{4,3*}TS_3^* - (\kappa_{3*,4}+\kappa_{0,4})TS_4, \\
Y_{04} & = R_{\mathrm{T}} - X_{04}, \\
Z_0 & = Z_{\mathrm{T}} - Z_1 - Z_2, \\
Q_0 & = Q_{\mathrm{T}} - Q_1, \\
T_{01} & = T_{\mathrm{T}} - TS_3^* - TS_4, \\
S_0 & = S_{\mathrm{T}} - \sum_{i=1}^{3} S_i - TS_3^* - TS_4.
\end{cases}
\tag{B.4}
$$

B.1.2 Coarse-graining functions

The coarse-graining functions which hold for $\tau_{\mathrm{II}} \to \infty$ are

$$
\begin{aligned}
\Gamma_{V_1}(X_{01}, Y_{01}, Y_4, T_0) &= \frac{\nu_{V_1} + \kappa_{\mathrm{U}}\Gamma_{W_1}}{\kappa_{\mathrm{U}} + \kappa_{\mathrm{F}} + \kappa_{\mathrm{d}} + \kappa_{\mathrm{C}} + \kappa_{\mathrm{Q}}}, \\
\Gamma_{U_1}(X_{01}, Y_{01}, Y_4, T_0) &= \frac{\nu_{U_1} + \gamma_{V_1}^{\mathrm{f}}\nu_{V_1} + \kappa_{-2}\gamma_{X_2}^{\mathrm{b}}(1-\varepsilon_{\mathrm{II},\mathrm{III}}\gamma_{X_2}^{\mathrm{f}}(T_0/T_{\mathrm{T}}))Y_4}{\kappa_{\mathrm{F}} + \kappa_{\mathrm{D}} + \kappa_{\mathrm{P}}^{\mathrm{o}} + \kappa_{\mathrm{P}}^{\mathrm{c}} + \kappa_{\mathrm{C}} + \kappa_{\mathrm{Q}}},
\end{aligned}
\tag{B.5}
$$

$$
\begin{aligned}
\Gamma_{X_2}(X_{01}, Y_{01}, Y_3, Y_4, T_0, T_1, Z_0, Z_1) &= \big[\kappa_1^{\mathrm{o}}\Gamma_{X_1} + Y_4 \\
&\quad + \varepsilon_{\mathrm{II},\mathrm{III}}\kappa_{-3}\frac{T_1}{T_{\mathrm{T}}}(\kappa_{-2}Y_0 + (\kappa_{41}Z_0 + \kappa_{42}Z_1)\frac{Y_3}{Z_{\mathrm{T}}})\big] \\
&\quad \times \gamma_{X_2}^{\mathrm{f}}\big[1 - \varepsilon_{\mathrm{II},\mathrm{III}}\gamma_{X_2}^{\mathrm{f}}(T_0/T_{\mathrm{T}})\big], \\
\Gamma_{Y_2}(X_{01}, Y_{01}, Y_3, Y_4, T_0, T_1) &= \Big(\varepsilon_{\mathrm{III},\mathrm{IV}}^{-1}\frac{\kappa_{-3}}{\kappa_{-1}^{\mathrm{c}} + \kappa_{\mathrm{tr}} + \kappa_{\mathrm{nr}}^{\mathrm{ind}}}\frac{T_1}{T}{}_{\mathrm{T}}Y_3 \\
&\quad + \frac{\kappa_1^{\mathrm{c}}}{\kappa_{-1}^{\mathrm{c}} + \kappa_{\mathrm{tr}} + \kappa_{\mathrm{nr}}^{\mathrm{ind}}}\Gamma_{Y_1}\Big) \\
&\quad \times \big(1 - \varepsilon_{\mathrm{II},\mathrm{III}}\gamma_{Y_2}^{\mathrm{f}}\big), \\
\Gamma_{X_3}(X_{01}, Y_{01}, Y_3, Y_4, T_0, T_1, Z_0, Z_1) &= \Big[Y_{0,1} + \varepsilon_{\mathrm{II},\mathrm{III}}(T_0/T_{\mathrm{T}})\Gamma_{X_2} + (\kappa_{41}Z_0 + \kappa_{42}Z_1)\frac{Y_3}{Z_{\mathrm{T}}}\Big] \\
&\quad \times (1 - \varepsilon_{\mathrm{II},\mathrm{III}}\kappa_{-3}T_1/T_{\mathrm{T}}), \\
\Gamma_{X_2^{\mathrm{tr}}} &= \frac{\kappa_{\mathrm{tr}}}{\kappa_{02}^{\mathrm{tr}}}\Gamma_{X_2}, \\
\Gamma_{X_0^{\mathrm{tr}}} &= \frac{\kappa_{\mathrm{tr}}}{\kappa_0^{\mathrm{ntr}}}\Gamma_{X_2}, \\
\Gamma_{Y_2^{\mathrm{tr}}} &= \frac{\kappa_{\mathrm{tr}}}{\kappa_{02}^{\mathrm{tr}}}\Gamma_{Y_2}, \\
\Gamma_{Y_0^{\mathrm{tr}}} &= \frac{\kappa_{\mathrm{tr}}}{\kappa_0^{\mathrm{ntr}}}\Gamma_{Y_2}, \\
\Gamma_{TS_i^*} &= \frac{\kappa_{i*,i}}{\kappa_{i+1,i*}}\frac{S_i}{S_{\mathrm{T}}}T_1.
\end{aligned}
\tag{B.6}
$$

Here, light excitation rate at core antenna, $\nu_{U_1} = \nu(W_{\mathrm{T}} + R_{\mathrm{T}})/(V_{\mathrm{T}} + W_{\mathrm{T}} + R_{\mathrm{T}}) = \nu(N_{\mathrm{C}} + 1)/(N_{\mathrm{P}} + N_{\mathrm{C}} + 1)$, light excitation rate at peripheral antenna, $\nu_{V_1} = \nu(V_{\mathrm{T}})/(V_{\mathrm{T}} + W_{\mathrm{T}} + R_{\mathrm{T}}) = \nu N_{\mathrm{P}}/(N_{\mathrm{P}} + N_{\mathrm{C}} + 1)$, effective rate of photochemical quenching via charge separation at open RC in core antenna, $\kappa_{\mathrm{P}}^{\mathrm{o}} = \kappa_1^{\mathrm{o}}\gamma_{X_2}^{\mathrm{f}}p(X_1 \mid U_1)$, effective rate of photochemical quenching via charge separation at closed RC in core antenna, $\kappa_{\mathrm{P}}^{\mathrm{c}} = \kappa_1^{\mathrm{c}}\gamma_{Y_2}^{\mathrm{f}}p(Y_1 \mid U_1)$, effective rate of non-photochemical quenching via non-radiative pathway in core antenna, $\kappa_{\mathrm{D}} = \kappa_{\mathrm{d}} + \kappa_1^{\mathrm{o}}\gamma_{X_2}^{\mathrm{d}}p(X_1 \mid U_1) + \kappa_1^{\mathrm{c}}\gamma_{Y_2}^{\mathrm{d}}p(Y_1 \mid U_1) + \kappa_{\mathrm{U}}\gamma_{V_1}^{\mathrm{d}}p(W_1 \mid U_1)$, rate of P_{680}^{+}-quenching, $\kappa_{\mathrm{C}} = \kappa_{\mathrm{c}}(X_4 + Y_4)/R_{\mathrm{T}}$, and rate of PQ-quenching, $\kappa_{\mathrm{Q}} = \kappa_{\mathrm{q}}Q_0/Q_{\mathrm{T}}$, are introduced. Besides, $\gamma_{X_2}^{\mathrm{f}} = \kappa_2/(\kappa_2 + \kappa_{-1}^{\mathrm{o}} + \kappa_{\mathrm{tr}} + \kappa_{\mathrm{nr}}^{\mathrm{ind}})$, $\gamma_{X_2}^{\mathrm{b}} = \kappa_{-1}^{\mathrm{o}}/(\kappa_2 + \kappa_{-1}^{\mathrm{o}} + \kappa_{\mathrm{tr}} + \kappa_{\mathrm{nr}}^{\mathrm{ind}})$, $\gamma_{X_2}^{\mathrm{d}} = (\kappa_{\mathrm{tr}} + \kappa_{\mathrm{nr}}^{\mathrm{ind}})/(\kappa_2 + \kappa_{-1}^{\mathrm{o}} + \kappa_{\mathrm{tr}} + \kappa_{\mathrm{nr}}^{\mathrm{ind}})$, $\gamma_{Y_2}^{\mathrm{f}} = \varepsilon_{\mathrm{II},\mathrm{III}}\kappa_3(T_0/T_{\mathrm{T}})/(\kappa_{-1}^{\mathrm{c}} + \kappa_{\mathrm{tr}} + \kappa_{\mathrm{nr}}^{\mathrm{ind}})$, $\gamma_{Y_2}^{\mathrm{d}} = (\kappa_{\mathrm{tr}} + \kappa_{\mathrm{nr}}^{\mathrm{ind}})/(\kappa_{-1}^{\mathrm{c}} + \kappa_{\mathrm{tr}} + \kappa_{\mathrm{nr}}^{\mathrm{ind}})$, $\gamma_{V_1}^{\mathrm{f}} = \kappa_{\mathrm{U}}/(\kappa_{\mathrm{U}} + \kappa_{\mathrm{F}} + \kappa_{\mathrm{d}} + \kappa_{\mathrm{C}} + \kappa_{\mathrm{Q}})$ and $\gamma_{V_1}^{\mathrm{d}} = (\kappa_{\mathrm{F}} + \kappa_{\mathrm{d}} + \kappa_{\mathrm{C}} + \kappa_{\mathrm{Q}})/(\kappa_{\mathrm{U}} + \kappa_{\mathrm{F}} + \kappa_{\mathrm{d}} + \kappa_{\mathrm{C}} + \kappa_{\mathrm{Q}})$ are introduced, where γ_x^{f}, γ_x^{b} and γ_x^{d} indicate the ratios of forward, backward and dissipation outflows to total

outflow from x state, respectively. The coarse-graining functions of Γ_{W_1}, Γ_{X_1} and Γ_{Y_1} are defined by factoring out $\varepsilon_{\mathrm{II,IV}}$ as

$$\begin{aligned}
\lim_{\tau_{\mathrm{II}}\to\infty} X_1(\tau_{\mathrm{II}}) &\equiv \varepsilon_{\mathrm{II,IV}}\Gamma_{X_1}(X_{01},Y_{01},Y_4,T_0) = \varepsilon_{\mathrm{II,IV}}\Gamma_{U_1}p(X_1\mid U_1),\\
\lim_{\tau_{\mathrm{II}}\to\infty} Y_1(\tau_{\mathrm{II}}) &\equiv \varepsilon_{\mathrm{II,IV}}\Gamma_{Y_1}(X_{01},Y_{01},Y_4,T_0) = \varepsilon_{\mathrm{II,IV}}\Gamma_{U_1}p(Y_1\mid U_1),\\
\lim_{\tau_{\mathrm{II}}\to\infty} W_1(\tau_{\mathrm{II}}) &\equiv \varepsilon_{\mathrm{II,IV}}\Gamma_{W_1}(X_{01},Y_{01},Y_4,T_0) = \varepsilon_{\mathrm{II,IV}}\Gamma_{U_1}p(W_1\mid U_1).
\end{aligned} \tag{B.7}$$

The coarse-graining functions which hold for $\tau_{\mathrm{III}}\to\infty$ are

$$\begin{aligned}
\Gamma_{Y_3}(E,X_{04},Y_{04},T_{01},Z_0,Z_1) =& \frac{\kappa_3\frac{\Gamma_{T_0}}{T_{\mathrm{T}}}}{\frac{\Gamma_{T_1}}{T_{\mathrm{T}}}[\kappa_{-3}-\varepsilon_{\mathrm{II,III}}\frac{\kappa_3}{\kappa_{-1}^{\mathrm{c}}+\kappa_{\mathrm{tr}}+\kappa_{\mathrm{nr}}^{\mathrm{ind}}}\frac{\Gamma_{T_0}}{T_{\mathrm{T}}}]+\varepsilon_{\mathrm{II,IV}}\frac{\kappa_{41}Z_0+\kappa_{42}Z_1}{Z_{\mathrm{T}}}}\Gamma_{Y_1},\\
\Gamma_{Y_4}(E,X_{04},Y_{04},T_{01}) =& p(Y_4\mid Y_{04})Y_{04},\\
\Gamma_{X_4}(E,X_{04},Y_{04},T_{01}) =& p(X_4\mid X_{04})X_{04},\\
\Gamma_{T_1}(E,X_{04},Y_{04},T_{01}) =& \frac{\kappa_3 H+\kappa_{-3}E+(\kappa_3-\kappa_{-3})T_{01}}{2(\kappa_3-\kappa_{-3})}\\
&\times\left\{1\pm\sqrt{1-\frac{4(\kappa_3-\kappa_{-3})\kappa_3 T_{01}H}{[\kappa_3 H+\kappa_{-3}E+(\kappa_3-\kappa_{-3})T_{01}]^2}}\right\}.
\end{aligned} \tag{B.8}$$

Here, the ratio of oxidized special pair is expressed as $p(Y_4\mid Y_{04})=p(X_4\mid X_{04})=\kappa_{-3}\Gamma_{T_1}/[\kappa_3(T_{01}-\Gamma_{T_1})+\kappa_{-3}\Gamma_{T_1}]$. With respect to Γ_{T_1}, the form which vanishes with the initial value, $H=0$, i.e., the case of $-$ out of $\pm$, is employed. Incidentally, if $H\ll 1$, the relation $\Gamma_{T_1}=\kappa_3 T_{01}H/[\kappa_3 H+\kappa_{-3}E+(\kappa_3-\kappa_{-3})T_{01}]$ holds and thus $\Gamma_{T_1}=0$ if $H=0$.

B.2 The case that hole transfer from $\mathbf{Y}_{\mathbf{Z}}^{+}$ to RC is neglected

B.2.1 ODEs with dimensionless time

The equations which have $\mathcal{O}(1)$ terms in ODEs with τ_{III} are

$$\begin{cases}
\frac{dX_{01}}{d\tau_{\mathrm{III}}} &= -\kappa_1^{\mathrm{o}}\gamma_{X_2}^{\mathrm{f}}\Gamma_{X_1}+\kappa_3\frac{T_0}{T_{\mathrm{T}}}X_4+\mathcal{O}(\varepsilon_{\mathrm{III,IV}})+\mathcal{O}(\varepsilon_{\mathrm{II,III}}),\\
\frac{dY_4}{d\tau_{\mathrm{III}}} &= \kappa_1^{\mathrm{o}}\gamma_{X_2}^{\mathrm{f}}\Gamma_{X_1}-\kappa_3\frac{T_0}{T_{\mathrm{T}}}Y_4+\mathcal{O}(\varepsilon_{\mathrm{III,IV}})+\mathcal{O}(\varepsilon_{\mathrm{II,III}}),\\
\frac{dX_4}{d\tau_{\mathrm{III}}} &= -\kappa_3\frac{T_0}{T_{\mathrm{T}}}X_4+\mathcal{O}(\varepsilon_{\mathrm{III,IV}})+\mathcal{O}(\varepsilon_{\mathrm{II,III}}),\\
\frac{dY_{01}}{d\tau_{\mathrm{III}}} &= \kappa_3\frac{T_0}{T_{\mathrm{T}}}Y_4+\mathcal{O}(\varepsilon_{\mathrm{III,IV}})+\mathcal{O}(\varepsilon_{\mathrm{II,III}}).
\end{cases} \tag{B.9}$$

B.2.2 Coarse-graining functions in the case of $\boldsymbol{v}\in\boldsymbol{A}_{\mathbf{IV}}$

The coarse-graining functions which hold for $\tau_{\mathrm{III}}\to\infty$ are

$$
\begin{aligned}
\Gamma_{X_3}(X_{01},Y_{01},Z_1,Z_2) =& \kappa_1^{\mathrm{o}}\gamma_{X_2}^{\mathrm{f}}\frac{\Gamma_{X_1}}{T_0/T_{\mathrm{T}}} \\
&\times\Big\{1-\varepsilon_{\mathrm{II},\mathrm{III}}\gamma_{X_2}^{\mathrm{f}}\frac{T_0}{T_{\mathrm{T}}} \\
&-\varepsilon_{\mathrm{III},\mathrm{IV}}\left[\frac{\kappa_{41}Z_0+\kappa_{42}Z_1}{Z_{\mathrm{T}}}+\kappa_{\mathrm{nr}}+\kappa_{-2}(1-\gamma_{X_2}^{\mathrm{f}})\right]\Big\}, \\
\Gamma_{X_4}(X_{01},Y_{01},Z_1,Z_2) =& \kappa_1^{\mathrm{o}}\gamma_{X_2}^{\mathrm{f}}\Gamma_{X_1}\frac{\kappa_{41}Z_0+\kappa_{42}Z_1}{Z_{\mathrm{T}}(T_0/T_{\mathrm{T}})^2}.
\end{aligned}
\tag{B.10}
$$

B.2.3 Coarse-graining functions in the case of $\boldsymbol{v}\in\boldsymbol{A}_{\mathrm{III}}$

The coarse-graining functions which hold for $\tau_{\mathrm{II}}\to\infty$ are

$$
\begin{aligned}
\Gamma_{U_1}(X_{01},Y_{01},Y_4) &= \frac{\nu_{U_1}+\nu_{V_1}\gamma_{V_1}^{\mathrm{f}}+\kappa_{-1}^{\mathrm{o}}\gamma_{X_2}^{\mathrm{f}}Y_4}{\kappa_{\mathrm{F}}+\kappa_{\mathrm{D}}+\kappa_{\mathrm{P}}^{\mathrm{o}}+\kappa_{\mathrm{P}}^{\mathrm{c}}+\kappa_{\mathrm{C}}+\kappa_{\mathrm{Q}}+\kappa_{\mathrm{Z}}}, \\
\Gamma_{X_1}(X_{01},Y_{01},Y_4) &= \Gamma_{U_1}p(X_1\mid U_1), \\
\Gamma_{Y_1}(X_{01},Y_{01},Y_4) &= \Gamma_{U_1}p(Y_1\mid U_1), \\
\Gamma_{X_2}(X_{01},Y_{01},Y_4) &= (1-\varepsilon_{\mathrm{II},\mathrm{III}}\gamma_{X_2}^{\mathrm{f}})\kappa_{-1}^{\mathrm{o}}\gamma_{X_2}^{\mathrm{f}}\Gamma_{X_1}+\varepsilon_{\mathrm{III},\mathrm{IV}}\gamma_{X_2}^{\mathrm{f}}Y_4, \\
\Gamma_{Y_2}(X_{01},Y_{01},Y_4) &= \frac{\kappa_1^{\mathrm{c}}}{\kappa_{-1}^{\mathrm{c}}+\kappa_{\mathrm{nr}}+\kappa_{\mathrm{tr}}}\Gamma_{Y_1}, \\
\Gamma_{X_3}(X_{01},Y_{01},Y_4,Y_3,Z_1,Z_2), &= \Big[Y_{01}+\frac{\varepsilon_{\mathrm{II},\mathrm{III}}}{\varepsilon_{\mathrm{III},\mathrm{IV}}}\frac{T_0}{T_{\mathrm{T}}}\Gamma_{X_2}+\Big(\kappa_{41}Z_0+\kappa_{42}Z_1\Big)\frac{Y_3}{Z_{\mathrm{T}}}\Big],
\end{aligned}
\tag{B.11}
$$

where $\kappa_{\mathrm{D}},\kappa_{\mathrm{P}}^{\mathrm{c}},\kappa_{\mathrm{P}}^{\mathrm{o}},\kappa_{\mathrm{C}}$ and κ_{Q} are the same as those in Appendix B.1.2. κ_{Z} is $\kappa_z(T_1+TS_3^*)/T_{\mathrm{T}}$.

The coarse-graining functions which hold for $\tau_{\mathrm{III}}\to\infty$ are

$$
\begin{aligned}
\Gamma_{X_{01}}(Y_{01},T_0,Z_0,Z_1) &= \frac{[\kappa_{\mathrm{d}}+\kappa_1^{\mathrm{c}}(\gamma_{Y_2}^{\mathrm{f}}+\gamma_{Y_2}^{\mathrm{d}})]Y_{01}+(\kappa_{\mathrm{d}}+\kappa_{\mathrm{U}}\gamma_{V1}^{\mathrm{d}})\bar{\kappa}_{-\mathrm{t}}R_{\mathrm{T}}}{\kappa_1^{\mathrm{o}}\gamma_{X_2}^{\mathrm{f}}(\nu_{U_1}+\nu_{V_1}\gamma_{V_1}^{\mathrm{f}})} \\
&\quad\times\frac{\kappa_{41}Z_0+\kappa_{42}Z_1}{Z_{\mathrm{T}}}Y_{01}, \\
\Gamma_{Y_4}(Y_{01},T_0,Z_0,Z_1) &= \frac{\kappa_{41}Z_0+\kappa_{42}Z_1}{Z_{\mathrm{T}}T_0/T_{\mathrm{T}}}Y_{01}, \\
\Gamma_{X_4}(Y_{01},T_0,Z_0,Z_1) &= \Big(\frac{\kappa_{41}Z_0+\kappa_{42}Z_1}{Z_{\mathrm{T}}T_0/T_{\mathrm{T}}}\Big)^2Y_{01}.
\end{aligned}
\tag{B.12}
$$

B.2.4 The initial value at $\boldsymbol{\tau_{\mathrm{IV}}=0}$ in TSTM in the case of $\boldsymbol{v}\in\boldsymbol{A}_{\mathrm{III}}$

Equation B.9 suggests that $X_{01}+Y_4+X_4+Y_{01}$ is a quasi-conserved quantity at τ_{III} scale. Consequently, a relation, $(\varepsilon_{\mathrm{III},\mathrm{IV}}\Gamma_{01}+\varepsilon_{\mathrm{III},\mathrm{IV}}\Gamma_{Y_4}+\varepsilon_{\mathrm{III},\mathrm{IV}}^2\Gamma_{X_4}+Y_{01})_{\tau_{\mathrm{IV}}=0}=$

$(X_{01} + Y_4 + X_4 + Y_{01})_{t=0}$
$\equiv C$, holds at $\tau_{\mathrm{IV}} = 0$, where C is a constant. Arranging this equation by considering up to $\mathcal{O}(\varepsilon_{\mathrm{III,IV}})$ terms, the initial value of Y_{01} at $\tau_{\mathrm{IV}} = 0$ in eq 4.12a is given as

$$\begin{aligned} Y_{01}(\tau_{\mathrm{IV}} = 0) &= \frac{C}{1 + \varepsilon_{\mathrm{III,IV}} \frac{\kappa_{41} Z_0 + \kappa_{42} Z_1}{Z_{\mathrm{T}}} \Big[\frac{(\kappa_{\mathrm{d}} + \kappa_{\mathrm{U}} \gamma_{X_2}^{\mathrm{f}}) \kappa_{-\mathrm{t}}^{-} R_{\mathrm{T}}}{\kappa_1^{\mathrm{o}} \gamma_{X_2}^{\mathrm{f}} \nu'} + \frac{T_{\mathrm{T}}}{T_0} \Big]} \\ &\simeq C \Big\{ 1 - \varepsilon_{\mathrm{III,IV}} \frac{\kappa_{41} Z_0 + \kappa_{42} Z_1}{Z_{\mathrm{T}}} \Big[\frac{(\kappa_{\mathrm{d}} + \kappa_{\mathrm{U}} \gamma_{X_2}^{\mathrm{f}}) \bar{\kappa}_{-\mathrm{t}} R_{\mathrm{T}}}{\kappa_1^{\mathrm{o}} \gamma_{X_2}^{\mathrm{f}} \nu'} + \frac{T_{\mathrm{T}}}{T_0} \Big] \Big\}. \end{aligned} \tag{B.13}$$

Appendix C

C.1 Coarse-graining functions of PS I

The coarse-graining functions Γ's of the states of PS I are expressed as below:

$$
\begin{aligned}
\lim_{\tau_{\mathrm{III}}\to\infty} XI_{64}(\tau_{\mathrm{III}}) &\equiv \varepsilon_{\mathrm{III,IV}}\Gamma_{XI_{64}},\\
\Gamma_{XI_{64}} &= \Big\{\kappa_2\gamma^f_{XI_{3A}}(\Gamma_{XI_{62A}}+\gamma^f_{XI_{54}}\Gamma_{XI_{52A}})+\kappa_{20}\gamma^f_{XI_{3B}}(\Gamma_{XI_{62B}}+\gamma^f_{XI_{54}}\Gamma_{XI_{52B}})\\
&\quad+\kappa_{-4}XI_{65}+\varepsilon_{\mathrm{III,IV}}\gamma^f_{XI_{54}}\kappa_{BF}YI_0/YI_{\mathrm{T}}\Gamma_{654}\Big\}\\
&\quad/\big(\kappa_4+\kappa_{-3}\gamma^d_{XI_{3A}}+\kappa_{-30}\gamma^d_{XI_{3B}}+\gamma^f_{XI_{54}}\kappa_{-AB}\big),\\
\lim_{\tau_{\mathrm{III}}\to\infty} XI_{54}(\tau_{\mathrm{III}}) &\equiv \varepsilon_{\mathrm{III,IV}}\Gamma_{XI_{54}},\\
\Gamma_{XI_{54}} &= \frac{\kappa_2\gamma^f_{XI_{3A}}\Gamma_{XI_{52A}}+\kappa_{20}\gamma^f_{XI_{3B}}\Gamma_{XI_{52B}}+\kappa_{-AB}\Gamma_{XI_{64}}+\varepsilon_{\mathrm{III,IV}}\kappa_{BF}YI_0/YI_{\mathrm{T}}\Gamma_{XI_{654}}}{\kappa_{AB}+\kappa_{-3}\gamma^d_{XI_{3A}}+\kappa_{-30}\gamma^d_{XI_{3B}}},\\
\lim_{\tau_{\mathrm{III}}\to\infty} XI_{654}(\tau_{\mathrm{III}}) &\equiv \varepsilon_{\mathrm{III,IV}}\Gamma_{XI_{654}},\\
\Gamma_{XI_{654}} &= \frac{\kappa_2\gamma^f_{XI_{3A}}\Gamma_{XI_{652A}}+\kappa_{20}\gamma^f_{XI_{3B}}\Gamma_{XI_{652B}}}{\kappa_3\gamma^d_{XI_{3A}}+\kappa_{30}\gamma^d_{XI_{3B}}},
\end{aligned}
\tag{C.1}
$$

where $\gamma^f_{XI_{54}} \equiv \kappa_{AB}/(\kappa_{-3}\gamma^d_{XI_{3A}}+\kappa_{-30}\gamma^d_{XI_{3B}}+\kappa_{AB})$ is introduced.

$$
\begin{aligned}
\lim_{\tau_{\text{III}}\to\infty} XI_{50}(\tau_{\text{III}}) &= \frac{\kappa_{-AB}}{\kappa_{AB}+\kappa_{-AB}} XI_{50/60} \\
&\equiv \Gamma_{XI_{50}}, \\
\lim_{\tau_{\text{III}}\to\infty} XI_{60}(\tau_{\text{III}}) &= \frac{\kappa_{AB}}{\kappa_{AB}+\kappa_{-AB}} XI_{50/60} \\
&\equiv \Gamma_{XI_{60}}, \\
\lim_{\tau_{\text{III}}\to\infty} XI_{53a}(\tau_{\text{III}}) &\equiv \varepsilon_{\text{III,IV}}\Gamma_{XI_{53a}}, \\
\Gamma_{XI_{53a}} &= \frac{\kappa_2\Gamma_{XI_{52A}}+\kappa_{-3}\Gamma_{XI_{54}}}{\kappa_3+\kappa_{1P}}, \\
\lim_{\tau_{\text{III}}\to\infty} XI_{63a}(\tau_{\text{III}}) &\equiv \varepsilon_{\text{III,IV}}\Gamma_{XI_{63a}}, \\
\Gamma_{XI_{63a}} &= \frac{\kappa_2\Gamma_{XI_{62A}}+\kappa_{-3}\Gamma_{XI_{64}}}{\kappa_3+\kappa_{1P}}, \\
\lim_{\tau_{\text{III}}\to\infty} XI_{53b}(\tau_{\text{III}}) &\equiv \varepsilon_{\text{III,IV}}\Gamma_{XI_{53b}}, \\
\Gamma_{XI_{53b}} &= \frac{\kappa_{20}\Gamma_{XI_{52B}}+\kappa_{-30}\Gamma_{XI_{54}}}{\kappa_{30}+\kappa_{1P}}, \\
\lim_{\tau_{\text{III}}\to\infty} XI_{63b}(\tau_{\text{III}}) &\equiv \varepsilon_{\text{III,IV}}\Gamma_{XI_{63b}}, \\
\Gamma_{XI_{63b}} &= \frac{\kappa_{20}\Gamma_{XI_{62B}}+\Gamma_{XI_{64}}+\kappa_{-30}\Gamma_{XI_{64}}}{\kappa_{30}+\kappa_{1P}}, \\
\lim_{\tau_{\text{III}}\to\infty} XI_{653a}(\tau_{\text{III}}) &\equiv \varepsilon_{\text{III,IV}}\Gamma_{XI_{653a}}, \\
\Gamma_{X653a} &= \frac{\kappa_2\Gamma_{XI_{652A}}+\kappa_{-3}\Gamma_{XI_{654}}}{\kappa_3+\kappa_{AB}}, \\
\lim_{\tau_{\text{III}}\to\infty} XI_{653b}(\tau_{\text{III}}) &\equiv \varepsilon_{\text{III,IV}}\Gamma_{XI_{653b}}, \\
\Gamma_{X653b} &= \frac{\kappa_{20}\Gamma_{XI_{652B}}+\kappa_{-30}\Gamma_{XI_{654}}}{\kappa_{30}+\kappa_{AB}}, \\
\lim_{\tau_{\text{III}}\to\infty} XI_{540}(\tau_{\text{III}}) &\equiv \varepsilon_{\text{III,IV}}\Gamma_{XI_{540}}, \\
\Gamma_{XI_{540}} &= \frac{\kappa_{BF}XI_{6540}YI_0/YI_T}{\kappa_{AB}\kappa_4/(\kappa_4+\kappa_{-AB})}, \\
\lim_{\tau_{\text{III}}\to\infty} XI_{640}(\tau_{\text{III}}) &\equiv \varepsilon_{\text{III,IV}}\Gamma_{XI_{640}}, \\
\Gamma_{XI_{640}} &= \frac{\kappa_{AB}}{\kappa_4+\kappa_{-AB}}\Gamma_{XI_{540}}.
\end{aligned}
\tag{C.2}
$$

C.2 The definition of I_{820} signal

The I_{820} signal is calculated by the following equation [58]:

$$
I_{820}(t) = 10^{(A_{P_{c^+}}(t)+A_{P^+_{700}}(t))}, \tag{C.3}
$$

where

$$\begin{aligned} A_{Pc^+}(t) &= d \times c \times \varepsilon_{Pc^+} \times \frac{C_0}{C_T}, \\ A_{P_{700}^+}(t) &= d \times c \times \varepsilon_{P_{700}^+} \times \frac{XI_{5/6} + XI_7 + XI_{65} + XI_{654}}{XI_T}. \end{aligned} \tag{C.4}$$

Here, d, c, ε_{Pc^+} and $\varepsilon_{P_{700}^+}$ are the path length (0.01 cm), the molar concentration of PS I (5.79×10^{-6} M), the paticular molar extinction coefficients for Pc^+ (1590 $M^{-1}\,cm^{-1}$) and P_{700}^+ (10,300 $M^{-1}\,cm^{-1}$) [107], respectively.

Bibliography

[1] Scholes, G. D.; Fleming, G. R.; Castro, A. O.; Grondelle, R. v. Lessons from nature about solar light harvesting. Nat. Chem. 2011, 3, 763-774.

[2] Papageorgiou, G. C.; Govindjee. Photosystem II fluorescence: slow changes-scaling from the past. J. Photochem. Photobiol. B. 2011, 104, 258-270.

[3] Papageorgiou, G. C.; Tsimilli-Michael, M.; Stamatakis, K. The fast and slow kinetics of chlorophyll *a* fluorescence induction in plants, algae and cyanobacteria: a viewpoint. Photosynth. Res. 2007, 94, 275-290.

[4] Fassioli, F.; Castro, A. O.; Scheuring, A.; Sturgis, J. N.; Johnson, N. F. Energy transfer in light-adapted photosynthetic membranes: from active to saturated photosynthesis. Biophys. J. 2009, 97, 2464-2473.

[5] Miloslavina, Y.; Szczepaniak, M.; Müller, M. G.; Sander, J.; Nowaczyk, M.; Rögner, M.; Holzwarth. A. R. Charge separation kinetics in intact photosystem II core particles is trap-limited. A picosecond fluorescence study. Biochemistry. 2006, 45, 2436-2442.

[6] Valkunas, L.; Chmeliov, J.; Trinkunas, G.; Duffy, C. D. P.; van Grondelle, R.; Ruban, A. V. Excitation migration, quenching, and regulation of photosynthetic light harvesting in photosystem II. J. Phys. Chem. B. 2011, 115, 9252-9260.

[7] Valkunas, L.; Trinkunas, G.; Chmeliov, J.; Ruban, A.V. Modeling of exciton quenching in photosystem II. Phys. Chem. Chem. Phys. 2009, 11, 7576-7584.

[8] Baake, E.; Schloder, J. Modelling the fast fluorescence rise of photosynthesis. Bull. Math. Biol. 1992, 54, 999-1021.

[9] Belyaeva, N. E.; Schmitt, F.-J.; Steffen, R.; Paschenko, V. Z.; Riznichenko, G. Yu.; Chemeris, Yu. K.; Renger, G.; Rubin, A. B. PS II model-based simulations of single turnover flash-induced transients of fluorescence yield monitored within the time domain of 100 ns-10 s on dark-adapted Chlorella pyrenoidosa cells. Photosynth Res. 2008, 98, 105-119.

[10] Guo, Y.; Tan, J. Modeling and simulation of the initial phases of chlorophyll fluorescence from Photosystem II. Biosystems. 2011, 103, 152-157.

[11] Lavergne, J.; Trissl, H. W. Theory of fluorescence induction in photosystem II: derivation of analytical expressions in a model including exciton-radical-pair equilibrium and restricted energy transfer between photosynthetic units. Biophys. J. 1995, 68, 2474-2792.

[12] Lazár, D. Modelling of light-induced chlorophyll *a* fluorescence rise (O-J-I-P transient) and changes in 820 nm-transmittance signal of photosynthesis. Photosynthetica. 2009, 47, 483-498.

[13] Lazár, D., Jablonský, J. On the approaches applied in formulation of a kinetic model of photosystem II: Different approaches lead to different simulations of the chlorophyll *a* fluorescence transients. J. Theor. Biol. 2008, 257, 260-269.

[14] Schatz, G. H.; Brock, H.; Holzwarth, R. Kinetic and energetic model for the primary processes in photosystem II. Biophys. J. 1988, 54, 397-405.

[15] Stirbet, A.; Govindjee; Strasser, B. J.; Strasser, R. J. Chlorophyll *a* fluorescence induction in higher plants: Modeling and numerical simulation. J. Theor. Biol. 1998, 193, 131-151.

[16] Vershubskii, A. V.; Kuvykin, I. V.; Priklonskii, V. I.; Tikhonov, A. N. Functional and topological aspects of pH-dependent regulation of electron and proton transport in chloroplasts in silico. Biosystems. 2011, 103, 164-179.

[17] Vredenberg, W. Kinetic analyses and mathematical modeling of primary photochemical and photoelectrochemical processes in plant photosystems. Biosystems. 2011, 103, 138-151.

[18] Zaks, J.; Amarnath, K.; Kramer, D. A.; Niyogi, K. K.; Fleming, G. R. A kinetic model of rapidly reversible nonphotochemical quenching. Proc. Natl. Acad. Sci. U.S.A. 2012, 109, 15757-15762.

[19] Zhu, X. -G.; Govindjee; Baker, N. R.; deSturler, E.; Ort, D. R.; Long, S. P. Chlorophyll *a* fluorescence induction kinetics in leaves predicted from a model describing each discrete step of excitation energy and electron transfer associated with Photosystem II. Planta. 2005, 223, 114-133.

[20] Stirbet, A.; Govindjee. Chlorophyll *a* fluorescence induction: a personal perspective of the thermal phase, the O-J-I-P rise. Photosynth. Res. 2012, 113, 15-61.

[21] Albertsson, P. A quantitative model of the domain structure of the photosynthetic membrane. Trends plant Sci. 2001, 6, 349-358.

[22] Allen, J. Photosynthesis of ATP-electrons, proton pumps, rotors, and poise. Cell,

2002, 110(3), 273-276.

[23] Govindjee. Chlorophyll *a* fluorescence: a bit of basics and history. In Chlorophyll *a* fluorescence: a signature of photosynthesis; Papageorgiou, G. C., Govindjee, Eds.; Advances in photosynthesis and Respiration, Vol. 19; Springer, Dordrecht, 2004; pp 1-41.

[24] Kouřil, R.; Dekker, J. P.; Boekema, E.J. Supramolecular organization of photosystem II in green plants. Biochim. Biophys. 2012, Acta 1817, 2-12.

[25] Tanaka, S.; Marcus, R. A. Electron transfer model for the electric field effect on quantum yield of charge separation in bacterial photosynthetic reaction centers. J. Phys. Chem. B. 1997, 101, 5031-5045.

[26] Clegg, R. M.; Sener, M.; Govindjee. From Förster resonance energy transfer to coherent resonance energy transfer and back. Proc. 2010, SPIE 7561, Optical Biopsy VII, 75610C.

[27] Eberhard, S.; Finazzi, G.; Wollman, F.-A. The dynamics of photosynthesis. Annu. Rev. Genet. 2008, 42, 463-515.

[28] Govindjee. Sixty-three years since Kautsky: chlorophyll *a* fluorescence. Aust. J. Plant. Physiol. 1995, 22, 131-160

[29] Baker, N. R. Chlorophyll fluorescence: a probe of photosynthesis in vivo. Annu. Rev. Plant Biol. 2008, 59, 89-113.

[30] Kramer, D. M.; Johnson, G.; Kiirats, O.; Edwards, G.E. New fluorescence parameters for the determination of Q_A redox state and excitation energy fluxes. Photosynthesis Res. 2004, 79, 209-218.

[31] Stirbet, A.; Riznichenko, G.Y.; Rubin, A. B.; Govindjee. Modeling chlorophyll *a* fluorescence transient: relation to photosynthesis. Biochemistry (Moscow). 2014, 79, 291-323.

[32] Butler W. L. On the primary nature of fluorescence yield changes associated with photosynthesis. Proc Natl Acad Sci USA. 1972, 69, 3420-3422.

[33] Renger, T.; Schlodder, E. Primary photochemical processes in photosystem II: bridging the gap between crystal structure and optical spectra. Chem Phys Chem. 2010, 11, 1141-1153.

[34] Zankel, K. L. Rapid fluorescence changes observed in chloroplasts: their relationship to the O2 evolving system. Biochim Biophys Acta. 1973, 325, 138-148.

[35] Vernotte, C.; Etienne, A. L.; Briantais, J-M. Quenching of the system II chlorophyll fluorescence by the plastoquinone pool. Biochim Biophys Acta. 1979, 545, 519-527.

[36] Horton, P.; Hague, A.; Studies on the induction of chlorophyll fluorescence in isolated barley protoplasts: IV. Resolution of nonphotochemical quenching. Biochim. Biophys. Acta. 1988, 932, 107-115.

[37] Krause, G. H.; Jahns, P. Non-photochemical energy dissipation determined by chlorophyll fluorescence quenching: characterization and function. In Chlorophyll *a* Fluorescence: A Signature of Photosynthesis; Papageorgiou G. C., Govindjee, Eds.; The Netherlands: Springer, Dordrecht, 2004; pp. 463-495.

[38] Minagawa, J. State transitions - The molecular remodeling of photosynthetic supercomplexes that controls energy flow in the chloroplast. Biochim. Biophys. Acta. 2010, 1807, 897-905.

[39] Amerongen, H. V.; Valkunas, L.; Grondelle, R. V. Photosynthetic Excitons.; World Scientific Pub Co Inc; Singapore; 2000.

[40] Hemenger, R. P.; Pearlstein, R. M.; Lindenber, K. L. Incoherent Exciton Quenching on Lattices. J. Math. Phys. 1972, 13, 1056-1063.

[41] Montroll, E. W.; Weiss, G. H. Random walks on lattices. II. J. Math. Phys. 1965, 6, 167-181.

[42] Montroll, E. W. Random walks on lattices. III. Calculation of first-passage times with application to exciton trapping on photosynthetic Units. J. Math. Phys. 1969, 10, 753-765.

[43] Perlstein, R. M. Exciton migration and trapping in photosynthesis. Photochem. Photobiol. 1982, 35, 835-844.

[44] Somsen, O. J.; Valkunas, L.; van Grondelle, R. A perturbed two-level model for exciton trapping in small photosynthetic systems. Biophys. J. 1996, 70, 669-683.

[45] Prigogine, I., Kondepudi, D., 1998. Modern Thermodynamics: From Heat Engines to Dissipative Structures, John Wiley and Sons.

[46] Baldazzi, V.; Bertin, N.; de Jong, H.; Génard, M. Towards multiscale plant models: integrating cellular networks. Trends Plant Sci. 2012, 17, 728-736.

[47] Goltsev, V.; Zaharieva, I.; Chernev, P.; Strasser, R. J. Delayed fluorescence in photosynthesis. Photosynth. Res. 2009, 101, 217-232.

[48] Lazár, D. Chlorophyll *a* fluorescence induction. Biochim. Biophys. Acta. Bioenergetics. 1999, 1412, 1-28.

[49] von Bertalanffy, L. General System Theory: Foundations, Development, Applications; George Braziller; New York, 1969.

[50] Alon, U. An Introduction to Systems Biology: Designe Principles of Biological Circuits; Chapman and Hall/CRC; Boca Raton, 2007.

[51] Duysens, L. M. N.; Sweers, H. T. Mechanism of the two photochemical reactions in algae as studied by means of fluorescence. In Studies on microalgae and photosynthetic bacteria; Japanese Society of Plant Physiologists, Eds.; University of Tokyo Press, Tokyo, 1963; pp 353-372.

[52] Laisk, A.; Eichelmann, H.; Oja, V. C3 photosynthesis in silico. Photosynth Res. 2006, 90, 45-66.

[53] Frolov, A. E.; Tikhonov, A. N. Influence of light-induced changes in stromal and lumenal pH on electron transport kinetics in chloroplasts: Mathematical modeling. Biophysics. 2007, 52, 398-405.

[54] Guo, Y.; Tan, J. A kinetic model structure for delayed fluorescence from plants. Biosystems. 2009, 95, 98-103.

[55] Kuvykin, I. V.; Vershubskii. A. V.; Priklonskii, V. I., Tikhonov, A. N. Computer simulation study of pH-dependent regulation of electron transport in chloroplasts. Biophysics. 2009, 54, 455-464.

[56] Lazár, D.; Pospisil, P. Mathematical simulation of chlorophyll *a* fluorescence rise measured with 3-(3', 4'-dichlorophenyl)-1,1- dimethylure barley leaves at room and high temperatures. Eur. Biophys. J. 1999, 28, 468-477.

[57] Lazár, D. Chlorophyll *a* Fluorescence Rise Induced by High Light Illumination of Dark-adapted Plant Tissue Studied by Means of a Model of Photosystem II and Considering Photosystem II Heterogeneity. J. Theor. Biol. 2003, 220, 469-503.

[58] Lazár, D. Modelling of light-induced chlorophyll *a* fluorescence rise (O-J-I-P transient) and changes in 820 nm-transmittance signal of photosynthesis. PHOTOSYNTHETICA. 2009, 47, 483-498.

[59] Lazár, D.; Jablonský, J. On the approaches applied in formulation of a kinetic model of photosystem II: Different approaches lead to different simulations of the chlorophyll *a* fluorescence transients. J. Theor. Biol. 2009, 257, 260-269.

[60] Lazár, D. Simulations show that a small part of variable chlorophyll *a* fluorescence originates in photosystem I and contributes to overall fluorescence rise. J. Theor. Biol. 2013, 335, 249-264.

[61] Xin, C. -P.; Yang, J.; Zhu, X. -G. A model of chlorophyll *a* fluorescence induction kinetics with explicit description of structural constraints of individual photosystem II units. Photosynth Res. 2013, 117, 339-354.

[62] Guo, Y.; Tan, J. Kinetic Monte Carlo simulation of the initial phases of chlorophyll fluorescence from photosystem II. Biosystems. 2014, 115, 1-4.

[63] Kok, B.; Forbush, B.; McGloin, M. P. Cooperation of charges in photosynthetic

O_2 evolution I A linear four step mechanism. Photochem. Photobiol. 1970, 11, 457-475.

[64] Schatz, G. H.; Brock, H.; Holzwarth, A. R. A kinetic and energetic model for the primary processes in photosystem II. Biophys. J. 1988, 54, 397-405.

[65] Trissl, H. W.; Lavergne, J. Fluorescence induction from photosystem II - analytical equations for the yields of photochemistry and fluorescence derived from analysis of a model including exciton-radical pair equilibrium and restricted energytransfer between photosynthetic units. Aust. J. Plant. Physiol. 1995, 22, 183-193.

[66] Velthuys, B. R.; Amesz, J. Charges accumulation at the reducing side of system 2 of photosynthesis. Biochim. Biophys. Acta. 1974, 333, 85-94.

[67] Vredenberg, W. J. A three-state model for energy trapping and chlorophyll fluorescence in photosystem II incorporating radical pair recombination. Biophys. J. 2000, 79, 26-38.

[68] Vredenberg, W. J.; Prášil, O. Modeling of chlorophyll *a* fluorescence kinetics in plant cells: derivation of a descriptive algorithm. In Photosynthesis in silico: understanding complexity from molecules to ecosystems; Laisk, A., Nedbal, L., Govindjee, Eds.; Advances in Photosynthesis and Respiration, Vol. 29; Springer: Dordrecht, 2009; pp 125-149.

[69] Vredenberg, W. J. Kinetic analysis and mathematical modeling of primary photochemical and photoelectrochemical processes in plant photosystems. BioSystems. 2011, 103, 139-150.

[70] Matsuoka, T.; Tanaka, S.; Ebina, K. Hierarchical coarse-graining model for photosystem II including electron and excitation-energy transfer processes. Biosystems. 2014, 117, 15-29.

[71] Schansker, G.; Tóth S. Z.; Strasser, R. J. Dark recovery of the Chl *a* fluorescence transient (OJIP) after light adaptation: the qT-component of non-photochemical quenching is related to an activated photosystem I acceptor side. Biochim. Biophys. Acta. 2006, 1757, 787-797.

[72] Schansker, G.; Tóth, S. Z.; Kovács, L.; Holzwarth, A. R.; Garab, G. Evidence for a fluorescence yield change driven by a light-induced conformational change within photosystem II during the fast chlorophyll *a* fluorescence rise. Biochim. Biophys. Acta. 2011, 1807, 1032-1043.

[73] Kramer, D. M.; DiMarco, G.; Loreto, F. Contribution of plastoquinone, quenching to saturation pulse-induced rise of chlorophyll fluorescence in leaves. In Pho-

tosynthesis: from light to biosphere, vol I; Mathis, P., Ed.; Kluwer Academic Publ, Dordrecht, 1995; pp 147-150.

[74] Okayama, S.; Butler, W. L.; The influence of cytochrome b 559 on the fluorescence yield of chloroplasts at low temperature. Biochim. Biophys. Acta. 1972, 267, 523-527.

[75] Müh, F. Glöckner, C.; Hellmich. J.; Zouni, A. Light-induced quinone reduction in photosystem II. Biochim. Biophys. Acta. 2012, 1817, 44-65.

[76] Rappaport, F.; Diner, B. Primary photochemistry and energetics leading to the oxidation of the (Mn)4Ca cluster and to the evolution of molecular oxygen in Photosystem II. Coord. Chem. Rev. 2008, 252, 259-272.

[77] Renger, G. Light induced oxidative water splitting in photosynthesis: energetics, kinetics and mechanism. J. Photochem. Photobiol. B. 2011, 104, 35-43.

[78] Renger, G. Mechanism of light induced water splitting in Photosystem II of oxygen evolving photosynthetic organisms. Biochim. Biophys. Acta. 2012, 1817, 1164-1176.

[79] Haehnel, W.; The reduction kinetics of chlorophyll *a*1 as indicator for proton uptake between light reactions in chloroplasts. Biochim. Biophys. Acta. 1976, 440, 506-521.

[80] Diner, B. A. Dependence of deactivation reactions of photosystem II on the redox state of the plastoquinone pool A, varied under anaerobic conditions. Equilibria on the acceptor side of photosystem II. Biochim. Biophys. Acta. 1977, 460, 247-258.

[81] Golbeck, J. H.; Kok, B. Redox titration of electron acceptor Q and the plastoquinone pool in photosystem II. Biochim. Biophys. Acta. 1979, 547, 347-360.

[82] Bowes, J.; Crofts, A. R.; Arntzen, C. J. Redox reactions on the reducing side of photosystem II in chloroplasts with altered herbicide binding-properties. Arch. Biochem. Biophys. 1980, 200, 303-308.

[83] Bowes, J.; Crofts, A. R. Binary oscillations in the rate of reoxidation of the primary acceptor of photosystem II. Biochim. Biophys. Acta. 1980, 590, 373-384.

[84] Robinson, H. H.; Crofts, A. R. Kinetics of the oxidation-reduction reactions of the photosystem II quinone acceptor complex, and the pathway for deactivation. FEBS Lett. 1983, 153, 221-226

[85] Brettel, K.; Schlodder, E.; Witt, H. T. Nanosecond reduction kinetics of photooxidized chlorophyll aII (P-680) in single flashes as a probe for the electron pathway, H^+-release and charge eccumulation in the O_2-evolving complex. Biochim. Bio-

phys. Acta. 1984, 766, 403-415.

[86] Peter, G. F.; Thornber, J. P. Biochemical composition and organization of higher plant photosystem II light harvesting pigment proteins. J. Biol. Chem. 1991, 266, 16745-16754.

[87] Joliot, P.; Lavergne, J.; Beal, D. Plastoquinone compartmentation in chloroplasts. 1 Evidence for domains with different rates of photo-reduction. Biochim. Biophys. Acta. 1992, 1101, 1-12.

[88] Roelofs, T. A.; Lee, C. H.; Holzwarth, A. R. Global target analysis of picosecond chlorophyll fluorescence kinetics from pea chloroplasts- a new approach to the characterization of the primary processes in photosystem II α units and β units. Biophys. J. 1992, 61, 1147-1163.

[89] Crofts, A. R.; Baroli, I.; Kramer, D.; Taoka, S. Kinetics of electron- transfer between QA and QB in wild-type and herbicideresistant mutants of *Chlamydomonas reinhardtii*. Z. Naturforschung C-a J. Biosci. 1993, 48, 259-266.

[90] Laible, P.; Zipfel, W.; Owens, T. Excited state dynamics in chlorophyll based antennae: the rate of transfer equlibrium. Biophys. J. 1994, 66, 844-860.

[91] Van Kampen, N. Elimination of fast variables. Phys. Rep. 1985, 124, 69-160.

[92] Nafe, J.; Maas, U. Modeling of NO formation based on ILDM reduced chemistry. Proc. Combust. Inst. 2002, 29, 1379-1385.

[93] Jamshidi, N.; Palsson, B. Ø. Top-down analysis of temporal hierarchy in biochemical reaction networks. PLoS Comput. Biol. 2008, 4, e1000177.

[94] Harbinson, J.; Hadely, C. L. The kinetics of $P-700^+$ reduction in leaves: a novel in situ probe of thylakoid functioning. Plant Cell Environ. 1989, 12, 357-369.

[95] Klughammer, C.; Schreiber, U. Analysis of light-induced absorbance changes in the near-infrared spectral region; I. Characterization of various components in isolated chloroplasts. Z. Naturforsch., C: Biosci. 1991, 46, 233-244.

[96] Croce, R.; Zucchelli, G.; Garlaschi, F. M.; Bassi, R.; Jennings, R. C. Excited state equilibration in the photosystem I-light-harvesting I complex: P700 is almost isoenergetic with its antenna. Biochem. 1996, 35, 8572-8579.

[97] Croce, R.; Dorra, D.; Holzwarth, A. R.; Jennings, R. C. Fluorescence decay and spectral evolution in intact photosystem I of higher plants. Biochem. 2000, 39, 6341-6348.

[98] Santabarbara, S.; Heathcote, P.; Evans, M. C. W. Modelling of the electron transfer reactions in Photosystem I by electron tunnelling theory: the phylloquinones bound to the PsaA and the PsaB reaction centre subunits of PS I are almost

isoenergetic to the iron-sulfur cluster F(X). Biochim. Biophys. Acta. 2005, 1708, 283-310 .

[99] Rutherford, a W.; Osyczka, A.; Rappaport, F. Back-reactions, short-circuits, leaks and other energy wasteful reactions in biological electron transfer: redox tuning to survive life in O_2. FEBS Lett. 2012, 586, 603-616.

[100] Schansker, G.; Srivastava, A.; Govindjee; Strasser. Characterization of the 820-nm transmission signal paralleling the chlorophyll *a* fluorescence rise (OJIP) in pea leaves. Funct. Plant Biol. 2003, 30, 785-796.

[101] Schansker, G.; Tóth, S. Z.; Strasser, R. J. Methyl viologen and dibromothymoquinone treatments of pea leaves reveal the role of photosystem I in the Chl *a* fluorescence rise OJIP. Biochim. Biophys. Acta, Bioenerg. 2005, 1706, 250-261.

[102] Munekage, Y.; Hashimoto, M.; Miyake, C.; Tomizawa, K.; Endo, T.; Tasaka, M.; Shikanai, T. Cyclic electron flow around photosystem I is essential for photosynthesis. Nature. 2004, 429, 579-582.

[103] Asada, K. The water-water cycle in chloroplasts: scavenging of active oxygens and dissipation of excess photons. Annu. Rev. Plant Physiol. Plant Mol. Biol. 1999, 50, 601-639.

[104] Miyake, C. Alternative Electron flows (Water-Water Cycle and Cyclic Electron Flow around PSI) in Photosynthesis: Molecular Mechanisms and Physiological Functions. Plant Cell Physiol. 2010, 51, 1951-1963.

[105] Oono, Y. The Nonlinear World: Conceptual Analysis and Phenomenology; Springer Series in Synergetics; Springer, Dordrecht, 2013.

[106] Takahashi, H.; Clowez, S.; Wollman, F. -A.; Vallon, O.; Rappaport, F. Cyclic electron flow is redox-controlled but independent of state transition. Nat Commun. 2012, 4, 1954-1961.

[107] Kirchhoff, H.; Schöttler, M. A.; Maurer, J.; Weis, E. Plastocyanin redox kinetics in spinach chloroplasts: evidence for disequilibrium in the high potential chain. Biochim. Biophys. Acta, Bioenerg. 2004, 1659, 63-72.

Doctor Thesis, Kobe University
"Systems approach to the multi-timescale dynamics of photosynthesis", 134 pages
Submitted on January 23rd, 2015
The date of publication is printed in cover of repository version published in Kobe University Repository Kernel.

Following papers were submitted with the doctoral dissertation for doctoral dissertation defense.

T. Matsuoka, S. Tanaka, K. Ebina, "Hierarchical coarse-graining model for photosystem II including electron and excitation-energy transfer processes"
Biosystems, 117, 15-29 (2014).

T. Matsuoka, S. Tanaka, K. Ebina, "Systems Approach to Excitation-Energy and Electron Transfer Reaction Networks in Photosystem II Complex: Model Studies for Chlorophyll *a* Fluorescence Induction Kinetics"

Submitted to Journal of Theoretical Biology.